1 FLUORESCENCE DETECTOR

1.1 Fluorescence Detector System

1.1.1 Physics Objectives

The Auger fluorescence detector (FD) is expected to operate always in conjunction with the surface detector (SD). Its primary purpose is to measure the longitudinal profile of showers recorded by the SD whenever it is dark and clear enough to make reliable measurements of atmospheric fluorescence from air showers. The integral of the longitudinal profile is used to determine the shower energy, and the speed of shower development is indicative of the primary particle's mass. The hybrid detector will also have better angular resolution than the surface array alone, and this may be of value in studying tightly clustered arrival directions.

The longitudinal shower profile measured by the fluorescence detector provides a model-independent measure of the electromagnetic shower energy. The primary energy can be estimated as 10% greater than the electromagnetic shower energy, and simulations show that this estimate is systematically in error at most by 5%, regardless of the type of primary particles.

The FD requirements are driven by the required resolution in measurements of the atmospheric depth where the shower reaches its maximum size, X_{max}. Reasonable resolution is needed to evaluate the composition of the cosmic ray primaries. The resolution should be small compared to the (approximately 100 g/cm^2) difference expected between the depth of maximum for a proton shower and for an iron shower of the same energy. Moreover, the experimental resolution should not significantly increase the spread of values for any one component of the composition by itself. The width of the expected X_{max} distribution for any nuclear type decreases with mass *A*, and the distribution of iron depth of maximum values has an rms spread of approximately 30 g/cm^2. We will therefore require that the experimental X_{max} resolution be no greater than 20 g/cm^2.

An accurate longitudinal profile (achieving 20 g/cm^2 depth of maximum resolution) requires good geometric reconstruction of the shower axis. At large zenith angles, a small error in zenith angle causes a significant error in atmospheric slant depth. Averaging over the range of hybrid shower zenith angles (0-60^O) leads to a rule of thumb that an error of one degree in zenith angle leads to an error of 20 g/cm^2 in X_{max}. The angular resolution of the hybrid showers must therefore be significantly better than 1^O, since other uncertainties also contribute to the depth of maximum uncertainty.

The longitudinal profile of each shower will be well measured if the X_{max} is determined to an accuracy of 20 g/cm^2. In particular, the profile will then be well enough measured that the profile integral (proportional to the total shower electromagnetic energy) will contribute less than a 10% fitting uncertainty to the uncertainty in shower energy. Good energy resolution is therefore implicit in the X_{max} resolution requirement.

1.1.2 Detector performance

1.1.2.1 Aperture

Simulations have been performed to calculate the triggering aperture of the FD baseline design, with the arrangement of eyes shown later in this chapter (Figure 1.21). The simulations require a hybrid

trigger *i.e.* triggers in at least one FD eye and at least two surface detectors. The design requirement is that the efficiency be near 100% at 10^{19} eV. This is achieved (Figure 1.1). In this figure it is clear that the FD will have a large stereo aperture at energies well above the threshold. Because we have access to SD timing information, stereo views are not vital for geometric reconstruction of the shower axis, but stereo views will assist in cross checks of our atmospheric transmission measurements. Also stereo triggers will yield some well measured showers (at large zenith angles or with cores outside the array) that are not recorded by the surface array.

There will be a large set of hybrid showers with energies below 10^{19} eV. The number of such showers will exceed the number recorded with energies above 10^{19} eV, even though the aperture is not that of the entire surface array. Such showers are measured by the FD only if they land within some radius of one of the eyes, where the radius is energy dependent.

The arrangement of four eyes at the Argentinian site reduces our dependence on a precise knowledge of light transmission through the atmosphere. The mean impact parameter from the closest triggering eye is 13 km at 10^{19} eV, compared with the effective Rayleigh scattering attenuation length (averaged over all light paths) of 19.5 km at 350nm.

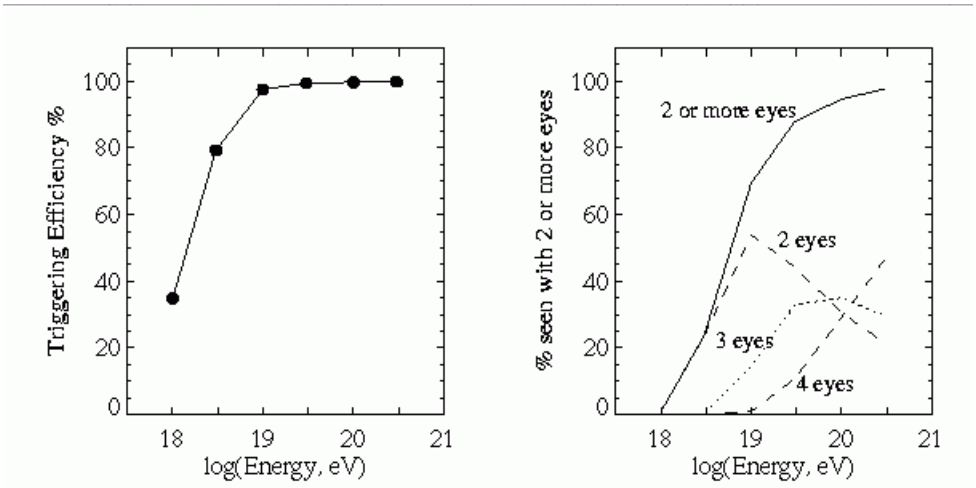

Figure 1.1 Left panel: The hybrid triggering efficiency as a function of energy for showers (with zenith angles less than 60^{O}) falling at random positions within the surface array boundary. At lease one fluorescence eye and two surface detectors are required to trigger. Note the acceptable aperture at energies lower than the nominal turn-on energy at 10^{19}eV. The triggering aperture can be obtained by multiplying the efficiency by 7375 km^{2}sr. Right panel: The fraction of events triggering more than one fluorescence station.

1.1.2.2 Reconstruction precision

As discussed above, the angular resolution of the detector must be small compared with 1^{O}, and the reference design will achieve an angular resolution of 0.5^{O}. There are two aspects of the angular resolution: the shower-detector plane determination and the angle of the shower axis within that plane. The shower-detector plane is determined by the set of pixels that see the shower axis. The need to resolve the shower-detector plane to better than 0.5^{O} has led to the constraint that the pixel size cannot

be larger than 1.5° in effective diameter. Determining the shower axis within the track-detector plane is done exclusively with timing information. The angular velocity of the shower front image moving through the FD field of view does not uniquely determine the shower axis. It does reduce the 2-parameter family of lines in the shower-detector plane to a 1-parameter family of possible axes. Each hypothetical axis makes a specific prediction for the arrival time of the shower front at each surface detector. The measured arrival times at one or more surface detectors thereby determines the correct shower axis. The need for good timing information is a primary reason for using sampling ADC electronics rather than simply recording a charge integral for triggering pixels. The ADC trace in each pixel allows an accurate determination of the time at which the shower front passed the center of the pixel. Analytic arguments and simulations show that time slices of 100 ns will yield the necessary timing accuracy to achieve the required angular resolution.

Simulation results on the expected performance of the hybrid detector are given in Table 1.1.

	Δdir (°)		ΔR_p (m)		$\Delta E/E$ (%)		ΔX_{max} (g/cm^2)	
Confidence limits	50%	90%	50%	90%	50%	90%	50%	90%
E=10^{18}eV	0.50	1.55	20	97	9.5	20.5	21	74
E=10^{19}eV	0.35	1.10	16	76	4.5	12.5	14	62
E=10^{20}eV	0.35	0.90	13	64	2.5	16.5	12	69

Table 1.1 Summary of hybrid reconstruction resolution for a single Auger eye, for events with zenith angles < 60° landing inside the surface array boundary. If more than one eye triggers on an event we use information from the eye with the longest angular track length. The detector is optimized for energies above 10^{19}eV but acceptable reconstruction is expected at energies down to 10^{18}eV. The values of the parameter bracketing 50% and 90% of the error distribution is given. The table lists errors in the arrival direction, impact parameter, energy and depth of maximum. Only statistical errors are considered here.

1.1.3 Overview of the reference design

A prominent innovation in the Auger FD design is the adoption of Schmidt optics. The proposal to use a Schmidt diaphragm (aperture stop) came from Alberto Cordero at Puebla. The problem had been posed at a FD workshop at Utah in March, 1996: How can we achieve a uniform spot (optical point spread function) over a large field of view? It had been recognized that coma aberration is a significant analysis problem even for a 15x15-degree field of view, and we had a desire to reduce the number of telescopes by increasing the field of view of each mirror. The problem with coma aberration is not only the analysis inconvenience of treating pixels differently depending on their angle from the telescope axis. It is also a signal-to-noise issue. Coma spreads the signal to neighboring pixels. To recover all of the signal, one must include the neighboring pixels, and that increases the noise. The Puebla proposal was to use the Schmidt diaphragm to eliminate coma aberration. The telescope optics becomes almost completely spherically symmetric, so pixels far from the telescope's axis are equivalent to pixels on the axis.

There are numerous advantages of the Schmidt optics design:

(a) Clean and simple analysis, since all pixels are the same.

(b) Wide field of view (30^o x 30^o) requiring fewer telescope units.

(c) Small aperture, so simpler and more reliable shutters.

(d) Fewer telescopes of compact design allows housing in one building.

(e) The diaphragm window can be covered by the optical filter, so we gain

- clean mirrors and camera (much less desert dust)
- temperature stability by interior heating and cooling
- the possibility of humidity control
- less fire risk since only UV light reaches the mirror
- the option of an interference filter, since there is a smaller range of incident angles at the filter

It should be noted that the motivation for Schmidt optics is primarily to make a superior detector that is free of coma aberration. There is not a great cost advantage. Although the number of telescopes is reduced by ¼, each has roughly 4 times greater mirror area. (The light collecting area is defined by the diaphragm which is small compared to the mirror when the field of view is large.) The Schmidt optics requires a curved focal surface (spherical symmetry). This is more difficult (and expensive) than a flat focal surface. We end up with one-fourth as many telescopes, but each is much larger and less simple. Having said this, it should also be noted that the reduced number of telescope units does save on certain costs which scale with the number of units. These can include calibration equipment, high voltage supplies, electronics crates and processors, conduits and wiring, etc. The overall cost of the detector is not greatly changed by the Schmidt optics. The number of pixels is the same, and it is the invariant pixel costs (PMT and pixel electronics) that are the major expense in either case.

The Schmidt optics is only the front end of an exciting and innovative fluorescence telescope design. We have designed a camera with excellent light collection efficiency, achieved by using *mercedes star* reflectors between photomultipliers. A new electronics system has been developed with a large dynamic range and 10MHz ADC sampling, to provide good quality pulse timing and amplitude information, and futhermore a flexible and very efficient hardware trigger scheme. We are also pioneering new techniques in detector calibration and atmospheric monitoring, two difficult tasks that are crucial for accurate shower profile measurements.

1.1.4 Detector System

1.1.4.1 Design Specifications

1.1.4.1.1 General Considerations

One observatory eye with a field of view of 180^o in azimuth and 30^o in elevation is built from 6 telescopes each covering 30^o x 30^o. To achieve this large field of view with a reasonable effort and good optical quality the layout of a Schmidt telescope is adapted. The elements of a telescope are the light collecting system (diaphragm and mirror) and the light detecting camera (a PMT array).

The detailed design of the optics contains a large spherical mirror with radius of curvature R=3.4m, having a field of view of 30^o x 30^o with a diaphragm at the center of curvature whose outer radius is 0.85m. These parameters are the result of signal/noise calculations for extensive air shower events at the experimental threshold, taking into account the amount of night sky background at the southern site of the Auger project and the obscuration by the PMT camera and its support structures.

The diaphragm will eliminate coma aberration while guaranteeing an almost uniform spot size (circle of least confusion) over a large field of view. With the above configuration the spot diameter (containing 90% of the mirror-reflected light) is kept under 0.5^o [1, 2].

The sensitivity of the telescope can be improved by enlarging the diaphragm to an outer radius of 1.1m. This choice determines the light collection efficiency (which is nearly doubled) and the size of the mirror surface, about 3.8 x 3.8 m (square with rounded corners). The corresponding increase in spherical aberration can be fully compensated by a corrector lens annulus covering the additional area between 0.85m < r < 1.1m.

This lens is connected to the wall of the building by an adjustable mechanical structure (aperture box) which keeps out the weather and stray light. This box also holds an optical filter transmitting in the nitrogen fluorescence wavelength range (300 to 400 nm) and blocking most of the night sky background. In addition, it acts as a protective window on the outside of the diaphragm.

Based on the considerations given above, we have set Rc =3.4 m. The (curved) focal surface is at approximately half that distance from the center of curvature, so the camera edge has a length of 1.70 x 30 (π/180) metres. The camera size and shape is therefore about 0.9m x 0.9m square.

Each pixel in the light detector should have a field of view small enough to measure accurately the light trajectory on the detector surface but large compared to the spot size. A diameter of about 1.5^o (26.2 mrad) is a good compromise. It corresponds to a linear size on the detector surface of about 0.0262 x 170 cm = 4.5 cm, which can be easily matched to commercially available PMTs. The image on the camera surface has finite dimensions due to two effects: spherical aberration and blurring due to mirror imperfections or alignment inaccuracy. Blurring and additional light from the outer diaphragm area with the corrector annulus should not substantially increase the spot size as determined primarily by spherical aberration.

1.1.4.1.2 Aperture System

1.1.4.1.2.1 Optical Filter

The idea of an optical filter is to transmit most of the fluorescence signal in the near-UV while blocking other night sky background to which the PMTs are sensitive. A good reference for detailed considerations of filter optimization is the article by J.W. Elbert [3]. There you can find a tabulation of the nitrogen fluorescence spectrum, a plot of the PMT spectral response, the night sky spectrum at Dugway and Akeno, HiRes filter transmittance as a function of wavelength, etc. The night sky spectrum should be measured at Pampa Amarilla for a rigorous analysis applicable to this project.

The signal spectrum of interest for filter design is not the emitted nitrogen fluorescence spectrum. That is the signal spectrum for nearby showers whose light is not affected by atmospheric attenuation. Nearby showers are sufficiently bright, however, and will be no problem for FD measurements regardless of the filter optimization. The filter should be designed to maximize S/N for distant showers. Because Rayleigh scattering is strongly wavelength dependent (inversely proportional to the 4th power of wavelength), and aerosol attenuation is also stronger at smaller wavelengths, the nitrogen fluorescence spectrum is significantly "reddened" by atmospheric transmission from a distant shower. A good filter should transmit most of this reddened spectrum while attenuating as much as possible the sky background light.

We can adopt here a procedure for comparing the relative merits of competing filters along with some specifications for the required performance. The test procedure will use the XP3062 PMT that has been proposed for use in the Auger telescopes. Any filter transmittance measurement is here taken to be simply

(PMT response with filter)/(PMT response without filter)

The circumstances of our experiment must be taken into account. To verify that a filter has good transmittance to the nitrogen fluorescence spectrum, we should use a nitrogen flashlamp. To verify that it has good transmittance for a reddened nitrogen spectrum, we should use a narrow band filter to check that the strong 391nm fluorescence line has high transmittance. The other experimental test is then to check that the filter has a relatively low transmittance for the night sky (preferably tested at Pampa Amarilla).

Our proposal for the filter specification is the following:

Transmittance > 0.80 at 391nm

Transmittance > 0.72 for the full nitrogen spectrum

R > 1.65, where R=(nitrogen transmittance)/sqrt(sky transmittance)

These specifications to apply to all relevant incidence angles ($0\text{-}21^{O}$)

Elbert found that the optimal filter for the HiRes aperture would be one that cuts off abruptly at 400nm (preserving most of the reddened nitrogen spectrum while significantly reducing the background). About 10% of the nitrogen spectrum photons are above 400nm, so the second condition above might mean 80% transmittance below 400nm and zero transmittance above 400nm, for example.

The ratio of transmittances R (in the third condition above) is a figure of merit that measures the increase in signal-to-noise effected by the filter. The numerator scales the signal and the denominator gives the scaling of the noise. (For distant showers, the signal is small and the noise is primarily the square root of the sky background.) The HiRes filter gives R slightly greater than 1.65, so the third condition is achievable. Comparing competing filters is done by comparing their figures-of-merit R, assuming the filters already satisfy the first two transmittance requirements. Relatively small improvement in R can be valuable. For example, increasing S/N by 10% would be the equivalent of increasing the collecting area by 21%, which is an expensive alternative. It is therefore worthwhile exploring methods for increasing R.

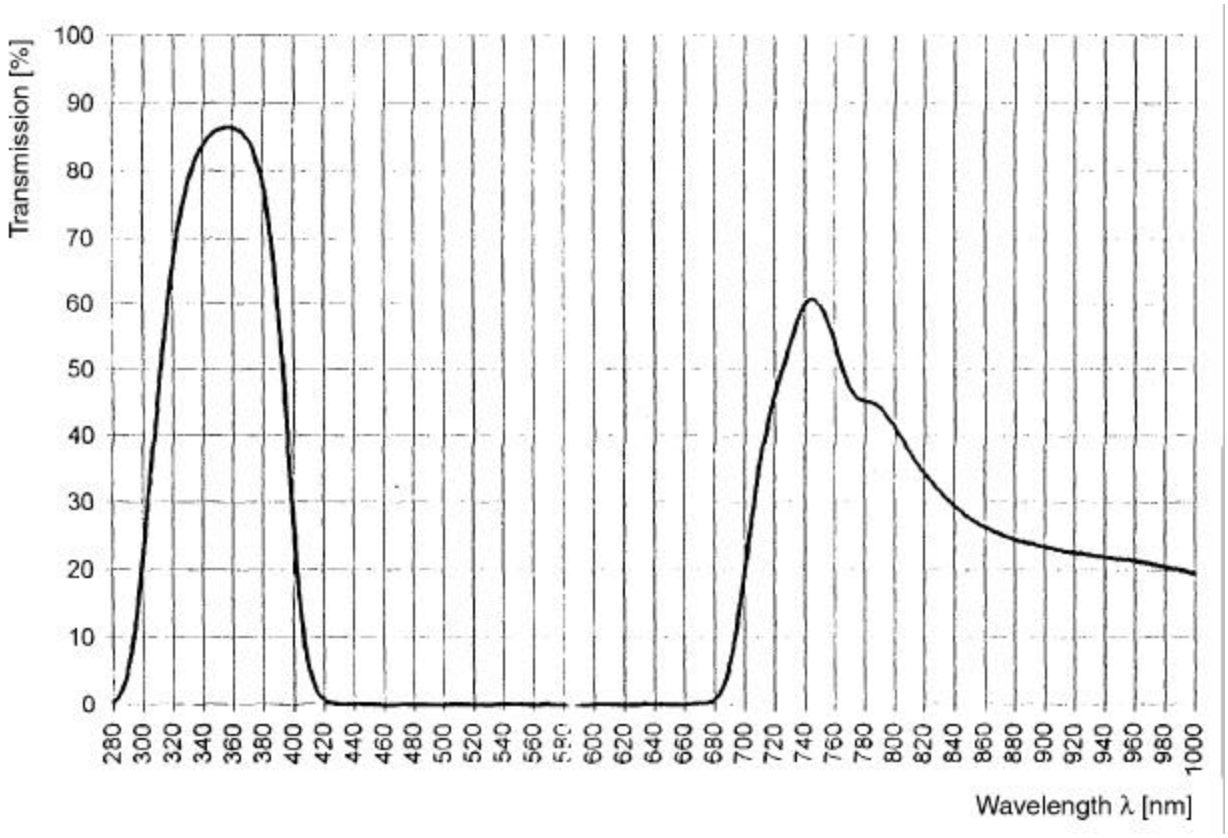

Figure 1.2 The transmission for Mug-6 glass, from 280 to 1000nm. The peak transmission is approximately 86% at about 355nm.

Such a study of filter requirements was performed [4] and recently extended focusing on the detection of fluorescence light above 350 nm - that light dominating the reddened spectrum from distant showers. Comparing samples of different absorption filters it was found that an adequate, cost-effective choice for the filter is Mug-6, manufactured by Schott-Desag. The transmittance spectrum of Mug-6 is given in Figure 1.2. It covers a wavelength range that overlaps well with the Nitrogen spectrum. With the techniques described in [4] the transmittance and the figure of merit R (as defined above) were measured for the region of the Nitrogen spectrum above 350 nm. The transmittance (for a ~3 mm thick sample) was measured to be 0.73 ± 0.03 and the figure of merit, $R = 2.02 \pm 0.06$.

Filter specifications also need to include mechanical criteria and longevity requirements. The reference design calls for the optical filter to be the telescope window, exposed to outdoor temperatures and wind on one side, controlled indoor conditions on the other side. The recent progress in the development of construction techniques makes the corrector ring option (see section 1.1.5.1) appear very promising. The circular filter aperture should in this case be increased from the 1.70 m in the reference design to a 2.10 m diameter, making the construction of an adequate mechanical structure even more challenging.

The thickness of the filter should be chosen to optimize light transmission without losing the mechanical strength required. The use of tempered glass is recommended. The number and size of glass sections to cover the aperture should be chosen keeping in mind a compromise between the desire to make many pieces to increase the mechanical strength and the requirement of minimizing joins that affect the aperture obscuration. The fraction of area obscured should not exceed ~5% of the total aperture area.

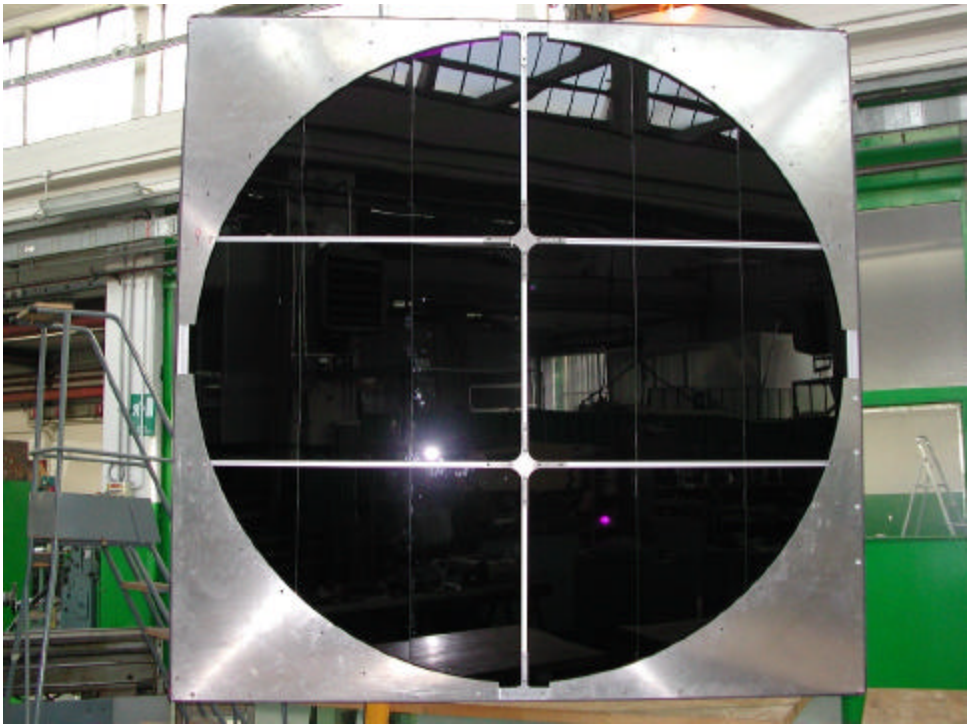

Figure 1.3: Filter prototype for the bays 4 and 5 at Los Leones.

The surfaces of filter sheets should be of sufficient quality not to introduce significant deterioration of the spot size. It is required that, with otherwise perfect optics, the effect of filter surface imperfections should not cause an increase greater than 5% in the radius of the circle containing 95% of the image light, for angles of incidence $< 21^{O}$.

The design of the mechanical support structure must be validated with a finite-element calculation to check for deformations under the structure's own weight and of external forces realistically mimicking those expected on the site.

The two prototype filters presently installed on bay 4 and 5 (Figure 1.3) at Los Leones were built out of 80 cm x 40 cm sheets of tempered Mug-6 glass. The thickness of each sheet is 3.25±0.02 mm. They fulfil most of the above requirements; however the field test is essential and will provide valuable lessons on what additional measures may be required to build a structure capable of surviving the 20 years of the experiment.

1.1.4.1.2.2 Corrector Ring

A corrector ring is being considered as an addition to the baseline design. One such ring is under test at the prototype system at Los Leones (Figure 1.4). This section is currently being written. For an earlier discussion, please see section 1.1.5.1.

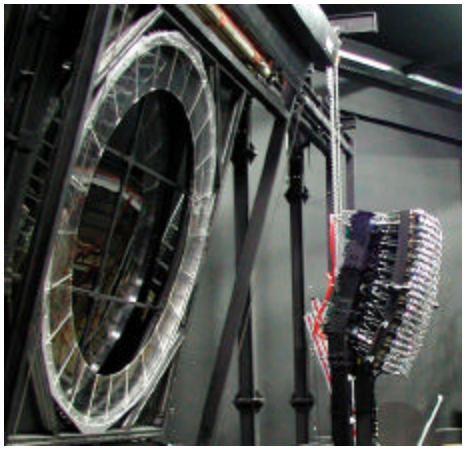

Figure 1.4 Prototype corrector ring in position at Los Leones.

1.1.4.1.3 Mirror System

1.1.4.1.3.1 Guidelines

The amount of light reaching the PMT array depends on :

(a) the coverage of the mirror surface which will have to be segmented,

(b) the reflectance of the coating,

(c) the transmittance of the filter in the nitrogen fluorescence band (300 to 400 nm)

The specifications are a cost effective solution to the problem of obtaining large light collection with small spot size, and uniformity over a large field of view. For all elements a major constraint will be the long operating time of the detector (about 20 years).

1.1.4.1.3.2 Mirror Segments

(a) **Segment shape:** a square shape optimizes the coverage of the quasi-square mirror surface (with less wasted surface at the perimeter of the mirror). Hexagons are favored from the point of view of mechanical stability of the corners of the segments. Both shapes will be used in different telescopes of the Auger fluorescence detector.

(b) **Tessellation:** from a logistics point of view it is desirable to deal with just a few mirror segments, all equal in shape. The maximum size of the segment that can be cheaply and easily built depends on the choice of the technique used in producing the mirrors, and is different for the two techniques chosen.

A tessellation easily realized with the proposed technique of diamond milling of aluminum alloy plates consists of 36 mirror segments of about 0.65 x 0.65 m^2 and 3 different (not exactly square) shapes. It will map the surface almost without cracks. The alternative solution of ground and polished glass mirrors calls for 60 hexagonal elements in 4 different shapes. Both methods can ensure:

i. Tolerance on the variation of the mean radius of curvature, R_c segment-to-segment: ±17mm, measured with an accuracy of ±1mm.
ii. Tolerance on mirror size (cutting inaccuracy): ±1 mm or better.
iii. Mirror substrate quality: 90% of the mirror-reflected light from the center of curvature returns to within 0.5 cm of the center of curvature.
iv. Quality of reflecting surface: the reflectance of the finished surface is about 90% for wavelengths between 300 and 400 nm.

Present plans are to build about 60% of the telescopes with aluminum mirrors and 40% with glass mirrors.

1.1.4.1.3.3 Aluminum mirrors

The production of mirror elements from solid aluminum alloy sheets is done in several steps. First a cast-aluminum backing with an approximate spherical shape is milled to an effective thickness of 18mm and the final radius of ~3400mm. Next, in a separate procedure, a 3mm AlMgSi0.5 sheet is glued to the backing with an appropriate epoxy using high temperature (150^O C) and a high-pressure piston.

Figure 1.5 An aluminum mirror element mounted on an optical test stand for the determination of the effective optical properties – radius of curvature and the intensity distribution of the reflected light.

Thereafter, the edges of the segments and a central hole are milled precisely. The final milling with high quality machines and diamond tools is done in a specialized commercial factory. Back in the Karlsruhe IK, the mirror surface is cleaned and finally protected by electrochemical anodization following a procedure developed by the MAGIC collaboration. A mounting ring flange is glued to the back and the mirror element is put on an optical bench for final testing.

The testing is performed using a point-like (0.2mm or 1mm diameter) light source. This is a blue LED (470nm) or a UV LED (370nm) with diffusers together with a reflective screen near the center of curvature of the mirror. A 12-bit cooled CCD camera is used for the measurement of the intensity distribution of the reflected light. The halo distribution can be measured with high sensitivity when the main intensity is put through a 10 mm diameter hole in the screen.

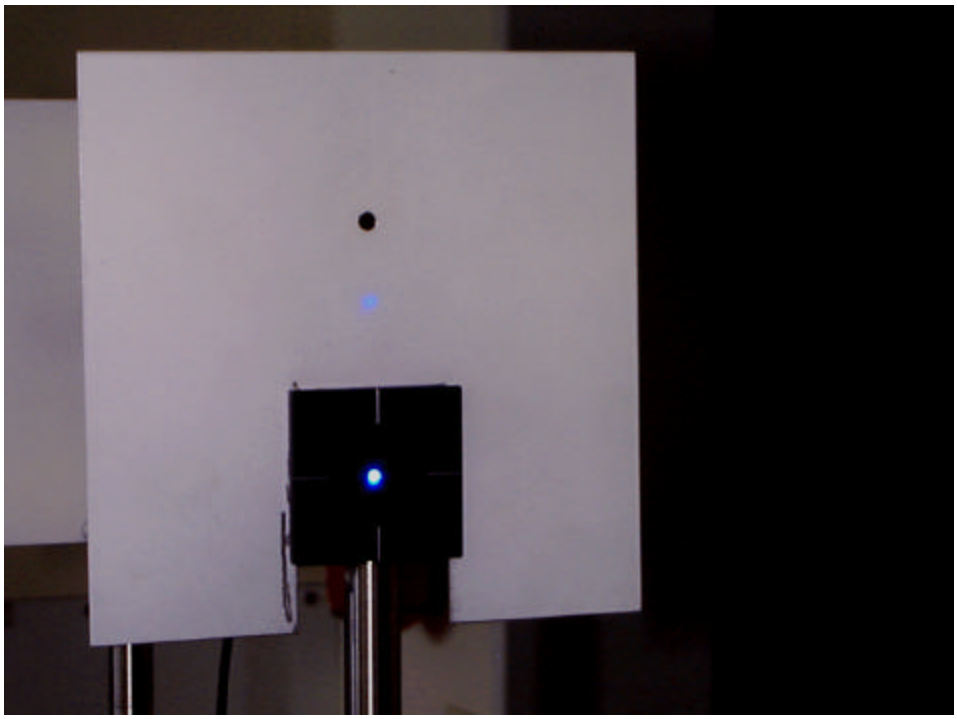

Figure 1.6 A "point-like" light source (LED at 470nm), and the spot of reflected light from a mirror segment. The screen is positioned close to the effective radius of curvature. The hole on the screen has a diameter of 10mm.

In the Engineering Array phase about 40 mirror elements were produced by diamond milling techniques using different methods of backing production. The tests clearly showed that the mirror optical properties easily match the specifications for the Auger FD telescopes. The mechanical stability of the segments has been improved considerably during this prototyping. The method of "hot" gluing will further improve the long-term behaviour of the mirrors. Simple mirror cleaning procedures need to be developed because of the large amount of dust in the telescope bays at Los Leones.

1.1.4.1.3.4 Glass Mirrors

The design of the glass mirrors stems from expertise and technological capabilities of the Joint Laboratory of Optics in Olomouc (JLO) and also from computer simulations of the influence of gravity, tilt and temperature changes on the geometrical shapes of mirrors. Other considerations taken into account are naturally the cost of production and the number of mirrors to be produced.

The rough shape of the mirrors is obtained by pressing molten glass into a mould. Moulding is done in a professional glass factory using a material with a trademark name of SIMAX. It is a borosilicate glass of a type similar to PYREX, with high tensile and bursting strengths (35 – 100 N mm^{-2} and 500 N mm^{-2} respectively), a low coefficient of thermal expansion (3.3 x10^{-6} K^{-1}), and good machining properties using standard optical technology. The glass is melted and homogenized in an electric tank furnace. Liquid glass with a temperature of about 1,450^{O}C is injected into the mould. The pieces are pressed one by one under a mass of 15,000 kg. After pressing, these intermediate products are annealed in an electric conveyer furnace.

Figure 1.7 Mirror milling at JLO in Olomouc.

The semi-finished products are machined at JLO in Olomouc. The machining of mirrors is based on standard operations commonly used in the optical industry (cutting, drilling, milling, grinding and polishing). However, all the operations had to be adapted for producing these large and thick mirrors. The final mirror shape is a hexagon, cut from a circular intermediate mirror. The mirrors used for the FD Engineering Array have a size defined by a circumscribed circle of radius 500 mm. In order to decrease the number of mirror segments required and thus to ease the production burden, the final mirror design has a circumscribed circle radius equal to 630 mm. All the technological operations

remain valid and the number of mirror segments per telescope decreases from 85 to 60. The change of radius also led to simpler tessellation (with 4 distinct shapes).

The next step in mirror production is the deposition of a reflecting layer. Before that, multiple washing and cleaning of the mirror surfaces is performed. A protective silicon oxide (SiO2) layer covers the reflecting aluminium layer. Standard vacuum equipment with an electron gun is employed for the deposition process.

The mirrors are subjected to rigorous control of the machined surface quality, and their geometrical and optical parameters. Final measurements are made of the reflectivity and the size of reflected light spot. For these operations a monochromator and a UV-sensitive camera are used.

Figure 1.8 Ronchi test of a glass mirror surface. Parallelism of the fringes shows the regular spherical surface of the mirror. Irregularity in the shape would be seen as irregularity of the fringes.

1.1.4.1.3.5 Segment Alignment

Each mirror segment is supported by an adjustable mount clamped to the mechanical support structure. The mount is connected to a ring flange glued to the back of the mirror segment.

Two adjustment screws and a spring act together on a central ball bearing. This type of mount has been successfully tested in the prototype mirror system and the design was improved and simplified further taking into account all the experience gained.

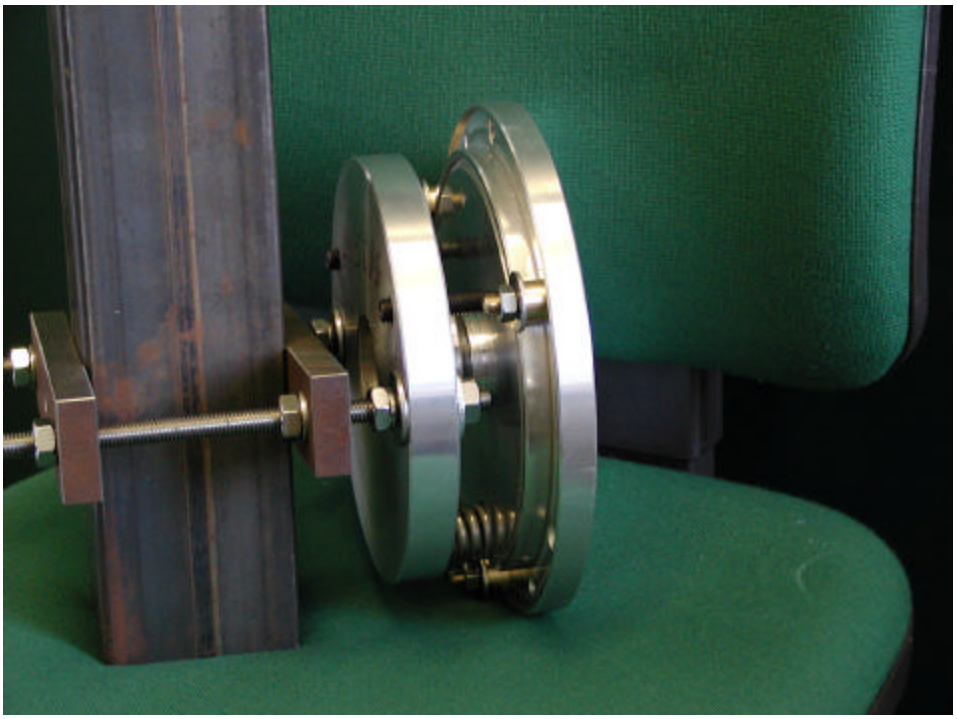

Figure 1.9 Photograph of a new prototype of the mirror mount to be used with both the aluminum and glass mirrors.

Specifications of the mounts include:

(a) Degrees of freedom and range of the adjustable variables: position along the mirror segment axis (±1 cm), polar angle (±5^o), and azimuth angle (±5^o)

(b) Adjustment and tolerance of position along axis: the tolerance of adjustment in the radial motion toward the center of curvature corresponds to a 1mm image shift. The precision achieved on the longitudinal position of the mirror segments is about ±1 mm.

(c) Adjustment and tolerance of azimuth and polar angle: one turn on the adjustment screw corresponds to 20 mrad, shifting the image by about 34 mm on the camera surface. The tolerance required (and easily achieved) is ±1mm. This must be compared with the 15 mm image size.

(d) Tolerance on the positioning of the adjustable mount on the main mechanical structure: in the plane tangent to the mechanical structure ±1mm, with full rotational freedom of the mirror segments.

(e) Mirror surface coverage: assume a tessellation without cracks. To guard against interference between adjacent mirrors coming either from differences in the radius of curvature or from lack of accuracy in cutting, a gap ($\delta_x = \delta_y = 4$mm) is allowed between mirrors. Central holes on each mirror segment proved to be useful during element production and mounting. In addition, for the aluminum mirror elements all corners are cut to enable easy access to calibration light sources on the mirror surface. All these losses add up to less than 2% of the mirror area.

The procurement and production of these mounts will be shared by several groups. Krakow will provide about 10% to 20% of the total, Karlsruhe (with the help of Prague with the mechanical production and assembly) and Puebla will together take care of the remaining mounts.

1.1.4.1.3.6 Mechanical Structure

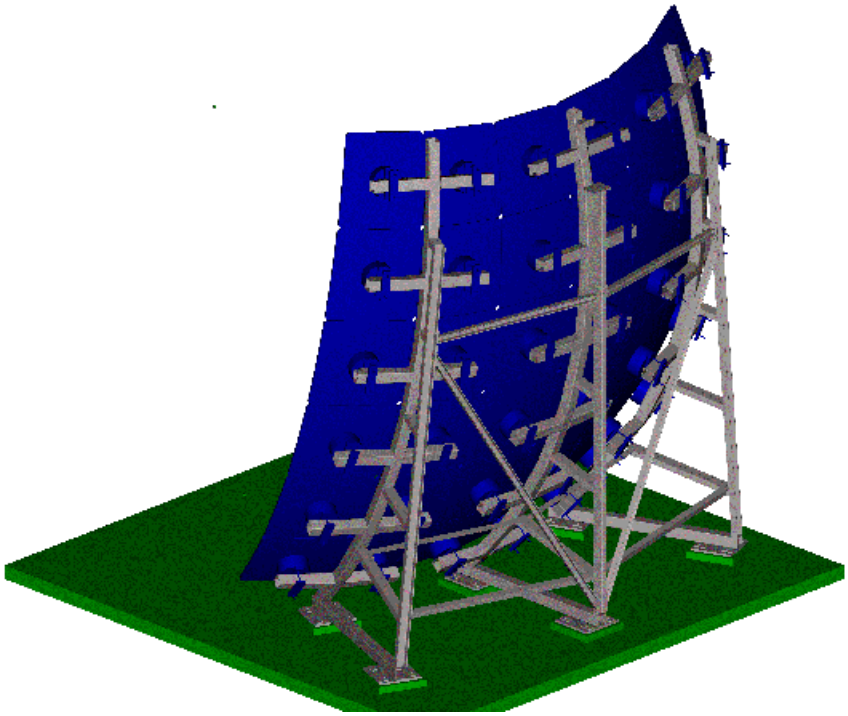

Figure 1.10 The new design of the support structure for the 36 aluminum mirror system for the Los Leones eye. The structure foreseen for the 60 glass mirror telescopes for the Coihueco eye is very similar.

The adjustable mirror mounts are clamped to a simple mechanical structure built from three nearly identical stands (80mm square steel tubes rolled to a radius of about 3.5m) bolted to the ground and connected by cross bars. These structures are aligned to about ± 10mm during installation.

The prototype system showed sufficient stability against external forces. A person climbing on different parts of the support after the mirror alignment produced an image shift of less than 1mm at the focal surface which was completely reversible. The new design will be as stable but easier to mount and align in the bays.

The top of each stand allows the mounting of a small pulley for an easy handling of the mirror elements during mirror installation.

The support structures for all telescopes will be provided by Karlsruhe.

1.1.4.1.3.7 Adjustment tools

To mark and identify the center of the mirror sphere and the diaphragm, a central reference point is mounted in front of the aperture box. It consists of a strong mechanical support which is bolted to the floor with a precise reference plate on top. The removable upper part of the reference point unit fits precisely to this plate and can support various adjustment tools.

A theodolite at the reference point is used for the initial determination of the geometry of the telescope system. After setting the mirror support stands, the position and rough orientation of the mirror mounts on the support structure is determined optically. The distance of each mount from the center of curvature is then measured by a laser distance meter (DISTO) on the reference point and mechanically adjusted to an accuracy of ± 1mm.

A mechanical system coupled to the reference point is used for the alignment of the position and the orientation (inclination) of the diaphragm system and corrector lens annulus. An accuracy of ± 2mm in position and ± 2mrad in orientation is easily achieved. In a similar way the position of the camera body is defined and set with a precision of about ± 1mm.

After the mounting of the mirror segments, a laser pointer on the reference point is used for the precise optical alignment of the axes of all mirror elements. The position of the returning laser beam can be determined to ± 1mm corresponding to an alignment of the optical mirror axis of better than 0.2 mrad.

All these tools have been tested very successfully during the installation of the prototype bays and the first two telescopes. Karlsruhe will provide the reference points and adjustment tools for all further telescopes with no more than minor changes in the design.

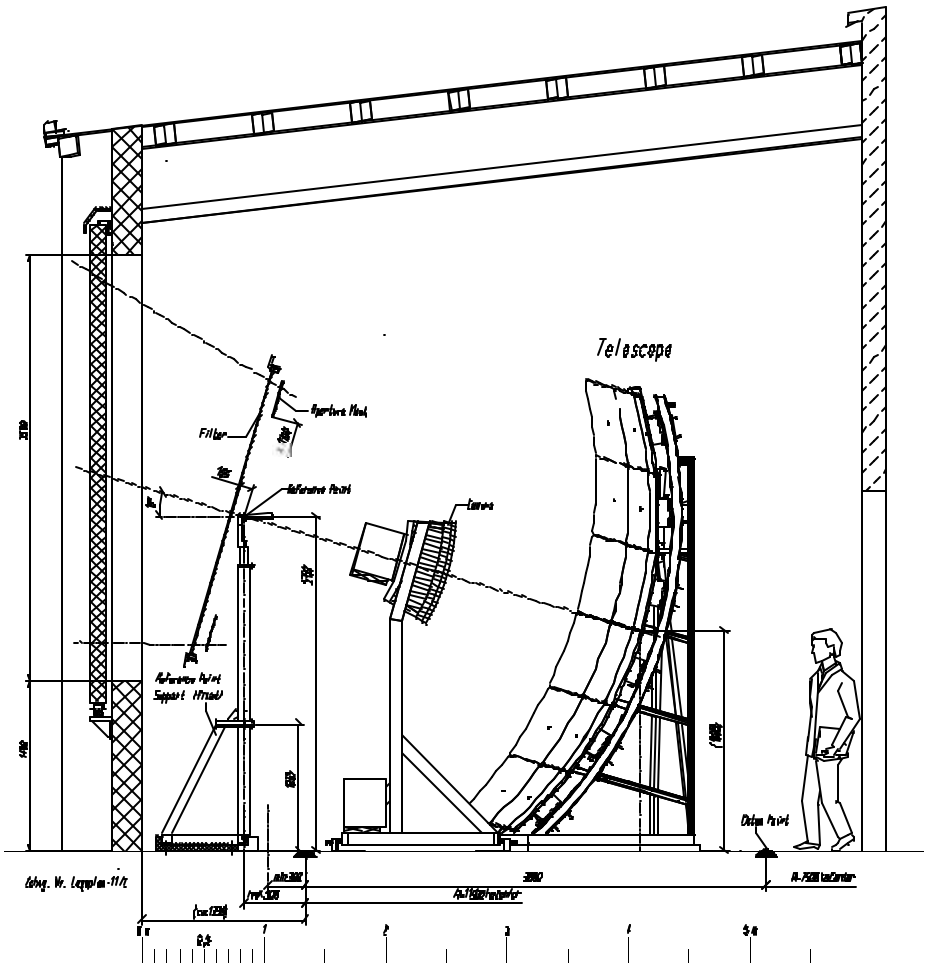

Figure 1.11 The reference point defines the center of the telescope geometry. The orientation of the telescope is defined by datum points on the ground and the 16 degree elevation of the central line of sight.

1.1.4.1.4 Camera System

1.1.4.1.4.1 Camera Body

The main parameters of the camera are fixed by the reference design of the optics which is based on the Schmidt system without corrector plate.

Geometry: The pixel surface must lie on the focal surface, i.e. the spherical surface where the circle of least confusion has minimum size. The radius of the focal surface, R_{foc}, is 1.743 m. On this focal surface the spot is rather well defined with a diameter of 15 mm corresponding to an angular size of 0.5^{O}.

The pixels should be hexagonal. Hexagons with side to side distance of 45.6 mm, corresponding to angular size of 1.5^{O} were chosen. Taking 3 pixels with one vertex in common, the angle between the center of the staggered pixel with respect to the line connecting the other two pixels centers is $\Delta\phi = 1.5^{O}\cos 30^{O} \sim 1.3^{O}$. The pixel centers are placed on the spherical surface by following the procedure shown in Figure 1.12. We use a *xyz* cartesian reference system. In the *xz* plane, pixel centers are placed at a distance R_{foc} from the origin. The first center is placed at $+\Delta\theta/2$ with respect to the *z* axis. The other pixel centers are obtained with increasing (decreasing) $\Delta\theta$ steps. Twenty pixels correspond to 30^{O} azimuthal aperture. The following row of pixels is obtained with a rotation of $\Delta\phi$ around the *x* axis. To produce the correct staggering, the pixel centers are moved by $\Delta\theta/2$ with respect to their previous position. The other rows are similarly obtained.

Once the pixel centers have been defined, the pixel hexagonal shape is determined by positioning six vertices. The angular positions of the vertices are obtained by moving in steps of $\Delta\theta/2$ and $\Delta\phi/3$ with respect to the pixel center as in Figure 1.12(b). Equal steps in angle produce different linear dimensions depending on the pixel position on the spherical surface. Thus, pixels are not regular hexagons, and their shape and size vary over the focal surface. However, differences of the side length are smaller than 1 mm, and are taken into account in the design of the light collectors.

The camera is then composed of 440 pixels, arranged in a 20x22 matrix (Figure 1.12(c)). The corresponding azimuthal range is 30^{O} with an elevation angle coverage of 28.6^{O}.

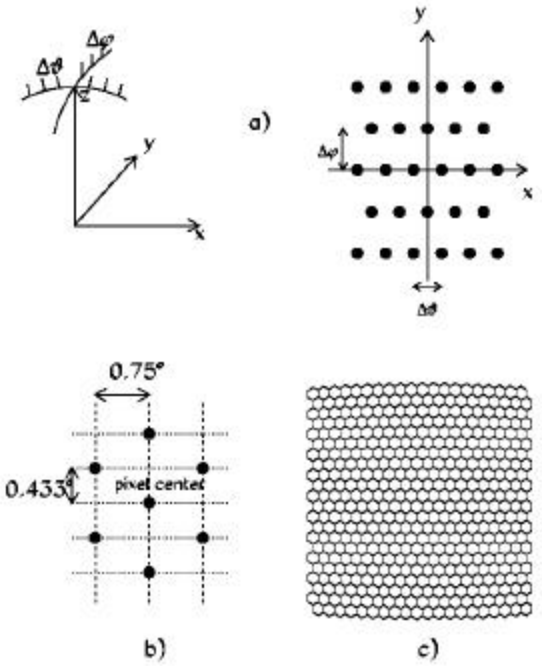

Figure 1.12 Geometrical construction of the FD camera: (a) pixel centers are placed on a spherical surface in steps of $\Delta\theta$ and $\Delta\phi$; (b) positioning of the pixel vertices around the pixel center; (c) the camera with 440 pixels arranged in a 20x22 matrix.

Mechanics: The camera body was constructed according to the geometry previously described. It was produced by numerically controlled machining of a single aluminium block. It consists of a plate of 60 mm uniform thickness and approximately square shape (930 mm horizontal x 860 mm vertical), with outer and inside surfaces of spherical shape. The outer radius of curvature is 1701 mm, while the inner radius is 1641 mm. Photomultiplier tubes are positioned inside 40 mm diameter holes which are drilled through the plate, corresponding to the pixel centers. Holes (3.2 mm diameter) drilled in the camera body at the pixel vertices, with the angular coordinates shown in Figure 1.12, are used to secure the light collectors in place. A picture of the camera body is shown in Figure 1.13. The camera body has area of about 0.8 m^2 and obscures the geometrical aperture of the diaphragm by 35%.

1.1.4.1.4.2 Camera Support

Mechanical Rigidity and Obscuration: The support of the body of the camera should ensure mechanical stability over long periods of time. Unavoidably it will produce additional obscuration of the mirror's field of view. The support designed for the prototype telescope has a cross-sectional area less than $0.1m^2$ (about one tenth of the camera itself) which we consider acceptable. It consists of a simple and robust two-leg steel support. A drawing of the support structure is shown in Figure 1.14. Note that the power and signal cables run inside the two legs of the support (C-shaped steel beams 5 cm wide) without producing additional obscuration.

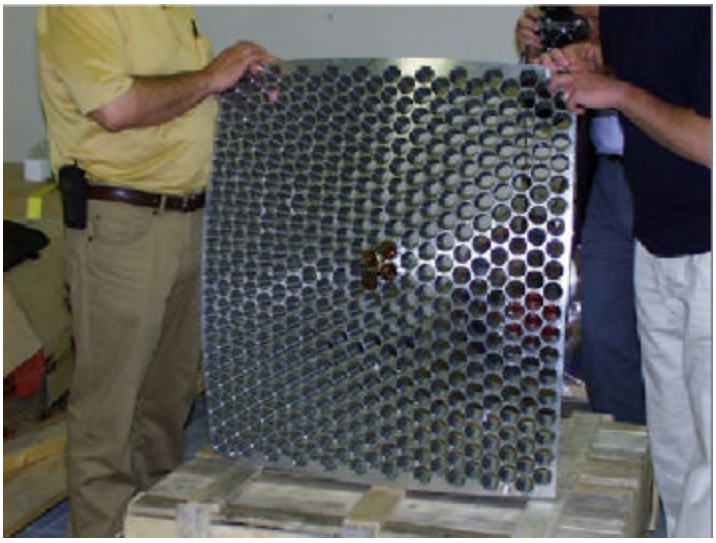

Figure 1.13 Picture of the camera body.

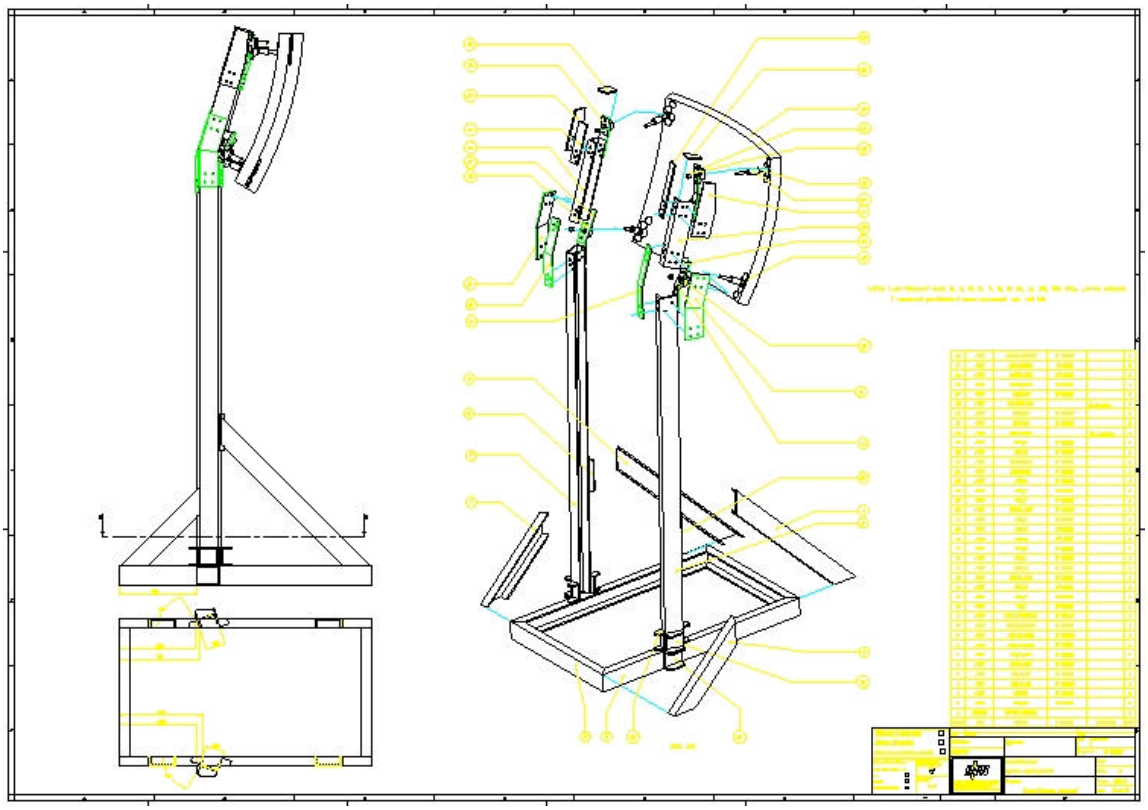

Figure 1.14 A drawing of the camera support.

1.1.4.1.4.3 Mechanical Precision and Alignment

Precision: The spot size increases by about 15% when the longitudinal distance from the center of curvature changes by ± 4 mm [1]. A deterioration of the spot at the 10-15% level is acceptable.

The accuracy on the longitudinal position of the pixels on the focal surface should be better than ± 3 mm. The overall uncertainty in the positioning of the pixels has two contributions:

(i) Point-to-point internal accuracy of the pixels on the camera body. The mechanical precision for the prototype camera body is at the level of ± 1 mm both in the longitudinal and transverse directions. This is in fact due to the positioning of the PMTs and of the light concentrators. The intrinsic accuracy of the rigid metal frame of the camera body is ± 0.1 mm.

(ii) Accuracy of alignment of the body of the camera on the focal surface. This requires mechanical adjustments of the camera body to better than ± 2 mm.

Alignment - Mechanical Adjustment: The basic requirement for the alignment of the camera is that the pixel surface should be placed at the correct longitudinal distance with respect to the center of curvature of the mirror (the reference point), and that the telescope axis should pass through the camera center.

Several mechanical adjustments were included in the design:

(i) the base of the support is placed in a rigid frame on the floor. Screws are provided on the sides of the frame which allow horizontal displacements of the support on the floor by ±5 cm.

(ii) four screws placed at the base of the support allow vertical displacements of the support with respect to the floor level by ± 5 cm.

(iii) four screws which fix the camera body to the support legs can be used for finer adjustments.

The camera is first aligned in the horizontal plane by using a digital level-inclinometer with a precision better than 0.05^{O}. The inclination with respect to the floor is similarly obtained. The camera center is placed along the telescope axis, defined by a line on the floor from the survey, with a plumb. Then, the nominal distance from the reference point is obtained by a precision rod measuring the distance to the back surface of the camera in several points with a precision of 0.1 mm. A laser distance-meter with a precision of ± 1 mm is also used for the same purpose.

The precision of the alignment of the camera was checked by a theodolite survey. Also, measurements of the mirror spot size on the pixel focal surface were performed, which confirm the specifications.

1.1.4.1.4.4 Light Collectors

The design of the FD camera involves a matrix of hexagonal pixels covering a field of view of approximately 30^{O}x 30^{O}, appropriately arranged over a spherical focal surface. Hexagonal PMTs (Photonis XP3062) were used to instrument the camera. Even if their hexagonal shape represents the best approximation to the pixel geometry, a significant amount of insensitive area is nevertheless present. In fact, some space between the PMTs is needed for safe mechanical packaging on the focal surface. Moreover, the effective cathode area is smaller than the area delimited by the PMT glass envelope. In order to maximize light collection and guarantee a sharp transition between adjacent pixels, the hexagonal PMTs are complemented by light collectors.

The requirements to be fulfilled by such light collectors are:

good matching of the hexagonal pixel geometry,

sharp transitions between adjacent pixels,

almost complete recovery of the light falling on the insensitive regions.

Geometry: The basic element for the pixel light collector is a *mercedes star*, with three arms at 120^{O}. We position a *mercedes* on each pixel vertex, so six *mercedes* guarantee the light collection for a given pixel. An illustration of the geometrical structure is given in Figure 1.15. The arm length is approximately half of the pixel side length. The arm section is an equilateral triangle. The base length of 9.2 mm is designed to match the photocathode inefficiency, ~2 mm for each adjacent PMT, plus the maximum space between PMTs glass sides, of the order of 5 mm. The triangle height is 18 mm, and the corresponding angle at the vertex is 14.3^{O}.

We optimized the geometry of the light collectors taking into account the characteristic features of the FD telescope. In fact, the Schmidt optics of the telescope produces a light spot of 15 mm diameter on the focal surface, with light ray angles of incidence in the interval between approximately 10^{O} and 30^{O}. The upper limit is determined by the aperture of the diaphragm, while the lower limit results from the shadow of the camera. We performed a Monte Carlo simulation of the FD telescope optics, where light rays are traced from the diaphragm up to the PMT photocathode, including reflections on the *mercedes*. We chose the geometry of the *mercedes* to maximize the light collection efficiency. The highest light collection efficiency, averaged over the FD focal surface, was found to be 94%, assuming a reflectivity of 85% for the surface of the light collectors (aluminized mylar). We validated the Monte Carlo simulation by performing a dedicated measurement of the camera uniformity (see below).

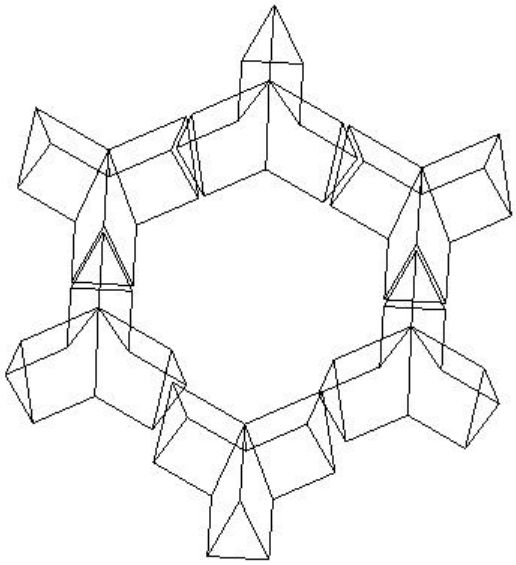

Figure 1.15 Six *mercedes* positioned in order to form a pixel. Each *mercedes star* has three arms at 120^{O}; the arm section is an equilateral triangle of 9.2 mm base length and 18 mm height.

Mechanics: The *mercedes* are produced by plastic injection moulding. Each *mercedes* must be precisely positioned on the spherical focal surface. For this purpose, the camera body has 3.2 mm diameter holes corresponding to the positions of the pixel vertices. Each mercedes is held at its center by a bar, approximately 10 cm long. The bar is fixed on one side at the bottom of the mercedes, and on the other side it is threaded. The bar is passed through the hole on the camera body, and a tapped cylinder is screwed on the bar thereby holding the mercedes in position. A picture of a few light collectors and PMTs mounted on the camera body is shown in Figure 1.16. Note that the pixels are defined on the focal surface where the top edges of the *mercedes* divide one pixel from its neighbors. The PMT cathodes are therefore recessed behind the focal surface.

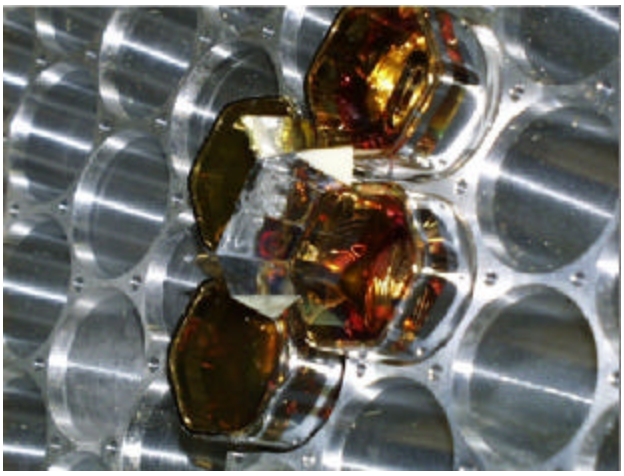

Figure 1.16 The mounting of light collectors.

Reflectivity: The mercedes surfaces are covered by a reflective material. Aluminium guarantees the best reflectivity in the range of interest of the nitrogen fluorescence light (300-400 nm). A reflectivity >80% should be adequate for our purpose. Several options have been considered, such as aluminized mylar, adhesive aluminium foils and standard aluminium evaporation. All guarantee good reflectivity.

For the prototype camera, the reflective surface is obtained by gluing aluminized mylar on the *mercedes* surfaces. The mylar foils are slightly longer than the *mercedes* arm, in order to accomodate the pixel side length variation over the focal surface.

Camera uniformity: We performed detailed measurements of the response to light of the FD camera with a set up which closely simulated the optics of the FD telescope [5]. A small version of the full size camera body held seven Photonis hexagonal phototubes XP3062, arranged in a *sunflower* configuration. A light diffusing cylinder which simulated the FD optics was moved over the *sunflower* surface in steps of a few millimeters. The light from the exit hole would hit one or more PMTs depending on its position over the surface. For each step, the signal of each photomultiplier was measured, and normalized to the value obtained when the light spot was positioned over the center of the PMT. Then, the sum ε of the normalized signals was calculated. For full light collection efficiency, ε is expected to be close to unity.

We took a first set of measurements without the light collectors, placing the exit hole of the light diffusing cylinder very close to the PMT photocathodes. Afterwards, the *mercedes* were mounted on the small camera body and we repeated the light scans placing the exit hole of the light diffusing cylinder very close to the edges of the light collectors. One example of results from a scan is shown in Figure 1.17.

In the measurements performed without light collectors, we observed significant losses of light at the pixel borders, with up to a 70% loss at a pixel vertex. Also, we measured a non-uniformity over the photocathode surface of at most ±10%. The non-uniformity is particularly evident at the edges of the PMT, and has a similar structure for different PMTs. It is related to the shape of the electric field collecting the photoelectrons and to the position of the first dynode.

On the other hand, the light collectors are efficiently recovering the light loss. The uniformity within a given pixel is also improved, since light rays which were hitting the photocathode borders are now redirected by reflection off the *mercedes* into the central region of the photocathode.

We determined a complete efficiency map of the *sunflower* equipped with light collectors. From these measurements, the light collection efficiency averaged over the FD focal surface was found to be 93%.

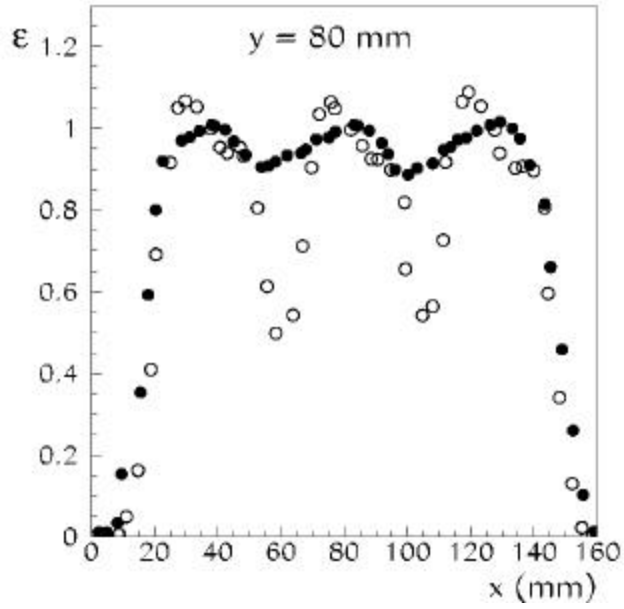

Figure 1.17 Measurement of the light collection efficiency, with a light spot moved along a line passing over three pixels. The full dots represent the measurements performed with the *mercedes*, while the open dots represent the measurements without the *mercedes*. In limited regions of the photocathode the light collection efficiency can be greater than one, since ε is normalized to the average light collection efficiency integrated over the photocathode surface.

1.1.4.1.4.5 Photomultiplier

Shape and size: The pixels of the camera lie on the spherical focal surface. They are hexagonal in shape. Therefore hexagonal PMTs are to be preferred because the system of Winston cones for optical coupling between pixel and photocathode becomes much simpler. The specifications of the overall optical system require pixels of 1.5^{O}. This corresponds to hexagonal pixels with side-to-side distance of 45.6 mm. The maximum external size of the PMTs must be somewhat smaller to allow the required configuration of the camera on the focal surface, the axis of each PMT being aligned with the center of curvature of the mirror.

Uniformity of response over the photocathode: All commercial PMTs have some non-uniformity of response over the cathode. It is generally a slowly varying function of the distance from the center of the cathode. We require that the non-uniformity should be in the range of good commercial tubes, within ±15%. We must keep in mind that the size of the light spot for a point source at infinity is about one-third of the size of the pixel and therefore the uniformity of response is not a critical parameter.

Spectral response: The reference design value considers a quantum efficiency that averages 0.25 in the range 330-400 nm. This corresponds to standard bialkali photocathodes. We allow a reduction of not more than 10% below this value.

Gain: The nominal gain for standard operation will be around $5x10^4$-10^5. Therefore an 8 stage PMT should be adequate.

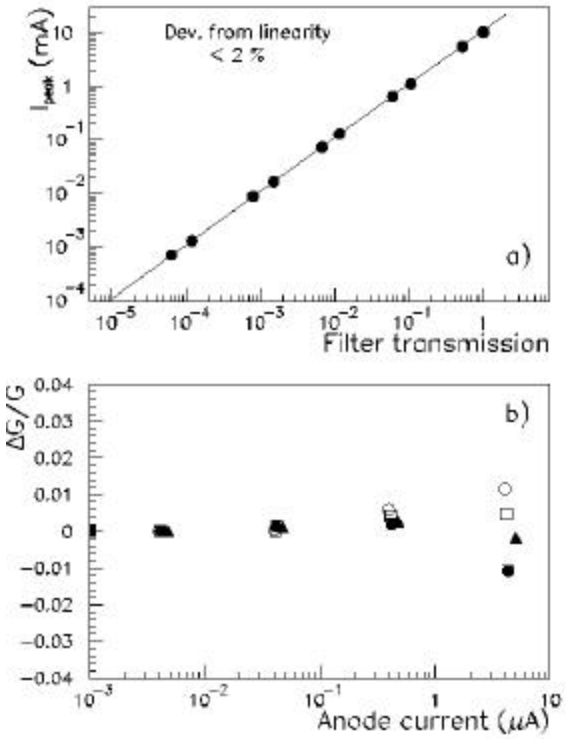

Figure 1.18 Measurement of (a) PMT linearity and (b) gain variation vs average anode current for four PMTs.

Linear dynamic range: This property is actually more related to the divider chain than to the PMT itself. In any case we require that the tube, operated at nominal gain (see directly above), should have linear response within better than 3% over a dynamic range of at least 10^4 for signals of 1μs. The upper limit of the signal can be fixed at an anode current of 1 mA (10 mA) for signals of 1 (0.1) μs width, which corresponds to $6x10^4$ photoelectrons for a gain of 10^5.

Moonlight tolerance and longevity: The gain of a tube deteriorates during operation as the integrated charge increases with time. Apparently the half-life of a tube (the time for reduction of the gain to one half) is correlated with the integrated charge collected at the anode. We require that the integrated anode charge corresponding to the half life of the tube not be less than 350 C.

Single photoelectron: Even though the standard operation of the PMT will not require the measurement of single photoelectrons, the PMT should have some single photoelectron capability, which guarantees a good resolution for the tube. No specific peak to valley requirement is needed, the evidence for a peak being sufficient.

The hexagonal photomultiplier XP3062 from Photonis was chosen as the detector PMT. A detailed study of its characteristics is available in [6]. Figure 1.18 shows an example of a measurement of the PMT linearity, and of the gain variation as a function of light intensity.

1.1.4.1.4.6 Photomultiplier Unit

The PMT, the base and the preamplifier will be a physically single unit. We have adopted a solution with flying leads on the PMTs.

In the prototype design, the leads are soldered to a small circular printed circuit card that contains the HV divider chain. A second card mounted axially, close to the divider chain card, contains the preamplifier circuit and some additional circuitry. A third card is needed to house the connector for HV, LV and signal distribution. The present design, involving three printed circuit cards, is imposed by the space needed for the additional circuitry of the anode current measurement and the electronics test pulse. The card diameter is 32 mm, which allows the mechanical mounting of the PMT units on the spherical camera body.

For mass production we recommend the design where a circular card containing the HV divider chain is soldered to the flying leads of the PMT at the factory. The preamplifier card could be mounted either axially or orthogonally and integrated at the factory according to our design and prescriptions. A test of the unit (PMT+base+preamplifier) should be made at the factory with our supervision, using the PMT unit test system developed by us. Control tests on samples of the production will be performed in the collaborating institutions.

1.1.4.1.4.7 Backplanes, Cables and Connectors

High voltage for the PMT base and low voltage for the preamplifier/driver are needed for each tube. Also, differential signals from the PMT preamplifier are driven in twisted pair cables up to the front-end boards.

In the solution adopted for the FD prototype, cables are distributed through backplanes positioned in the camera shadow. Each backplane supplies HV and LV to 44 PMTs. The differential signals are grouped into multi-pin connectors. Also, the facility for a test pulse signal to the preamplifier/driver is provided.

Cables and Connectors (PMT to backplane): A single cable brings HV and LV to the PMT from the backplane, and drives the differential signals out of the preamplifier. Eight wires are used in the current configuration: two for the differential signal (twisted), two for positive and negative LV (twisted), two for HV and ground (twisted), and two for the test pulse signal and additional ground. A compact (1.3 x 0.5cm) 10-contact connector is used at both ends of the cable. Two contacts near the HV are left free for further insulation. The cable length is 35 cm. The assembly has been produced by 3M. HV insulation was tested up to 2 kV.

Backplane: The camera backplane is a printed circuit card of rectangular shape (22 cm x 32 cm). The card is composed of six layers: one HV and one LV distribution layer, one signal layer sandwiched between two ground layers, and a test pulse layer. HV from one input connector is distributed to 44 PMTs. The low voltage distribution is analogous. A fuse for overcurrent protection is included in each

distribution line. Differential signals from 11 PMT units, corresponding to half of a pixel column, are grouped into a low profile 26-pin connector. Each card has four of these connectors. The grouping was chosen in order to avoid crossing of signal lines and HV/LV lines, therefore minimizing crosstalk. The 440 PMTs of a FD camera are served by ten backplanes. The space between backplanes (~ 15 cm) allows access to photomultipliers and light collectors.

Cables and Connectors (backplane to Analog Board): A round shielded cable with 11 twisted pair signal wires, ground and test pulse wires is plugged into each of the four connectors on the backplane. Two of these cables, from two corresponding upper and lower backplane cards, are joined into one single connector at the Analog Board (AB). Thus, the 22 pixels of each pixel column are mapped into one AB as specified by the FDE group.

A special support, which closely follows the spherical shape of the camera body, holds the boards and cables in the shadow of the camera, *i.e.* inside the pyramid with a vertex on the common center of curvature of the mirror and camera and sides at 15^{O}. A picture of the back of the camera with boards and cables in place is shown in Figure 1.19.

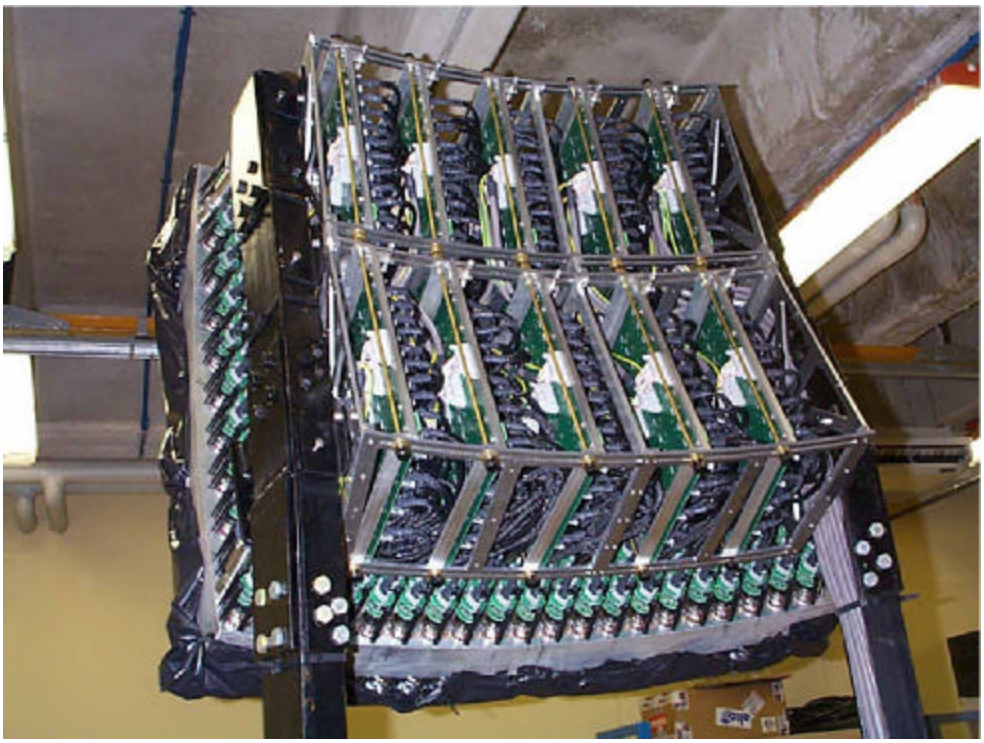

Figure 1.19 Picture of the back of the camera, showing the distribution boards and cables.

1.1.4.2 **Buildings**

Each eye will be housed in a single building. The central eye will consist of 12 telescopes. The perimeter eyes will have only 6 telescopes. The Los Leones perimeter eye was the first to be constructed. The ground plan of the 7m high single story building is shown in Figure 1.20. The radius of

the building is 14m. The 6 telescopes point radially outward through 6 windows of 3m (w) x 3.5m (h) each at the perimeter of the building. Attached to each window is the aperture system on the inside and two sliding doors on the outside. The rear part of the central area contains the data acquisition room, a small laboratory room and a room for calibration equipment. Above these rooms is a gallery providing space for equipment needed for calibration and atmospheric monitoring. All rooms, the telescope bays and the gallery are connected to the data acquisition room through a Local area Network (LAN), the data acquisition room has an optical fibre ETHERNET link to the communication tower located at the south perimeter of the eye area. The light sources in the calibration room deliver light to the telescopes by optical fibre. Many details had to be considered about how the telescope bays are partitioned from each other, how the lighting should be arranged, cable tray locations, etc. The layout of the building at Los Leones turned out to be a satisfactory solution. Based on the experience gathered during the installation and operation of two prototype telescopes in the Los Leones building, only minor modifications are required for the design of future buildings.

1.1.4.3 Heating, cooling, and humidity control

The building temperature should be maintained at 21±3 degrees Centigrade. This is partly because the PMT gain varies by approximately 0.5% per degree. If we maintain a temperature of 21^{o}, the PMT gain will not change due to temperature, and a 3^{o} deviation causes only a 1.5% gain variation. This will not be a significant contribution to our calibration uncertainty. Other electronic components may change characteristics under large temperature changes. The specified range will prevent that. Perhaps the strongest constraint on temperature variation is mandated by the optics. The mirror shape will change a small amount with temperature. To keep the spot size small, we need to keep the temperature constant to within $\pm 3^{o}$ C.

For the sake of the electronics, the relative humidity should not exceed 70%. Experience with the prototype detector will tell us whether or not we need to incorporate humidity control in the eye buildings. Probably the building interior will rarely have such high humidity at night in the desert when the weather is suitable for observations.

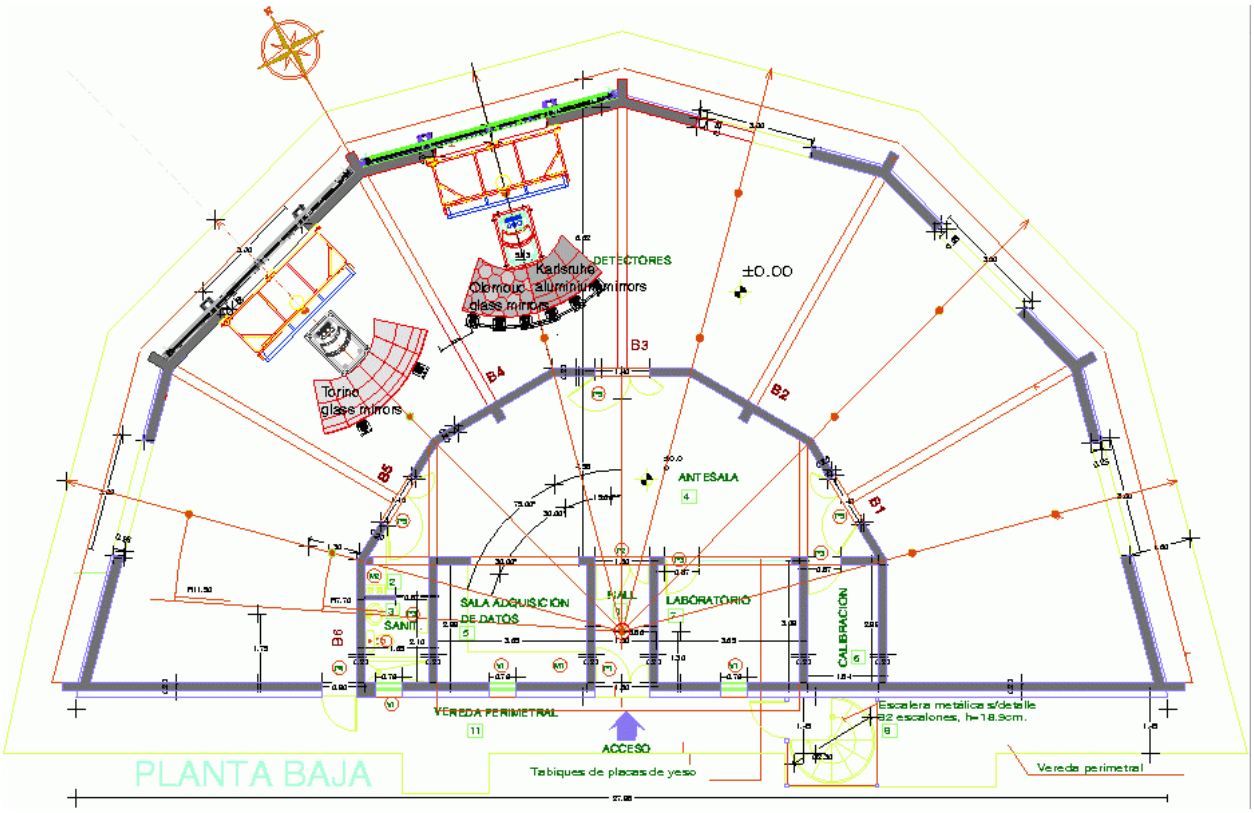

Figure 1.20 Layout of the FD building at Los Leones with prototype telescopes in bay 4 and 5.

1.1.5 Options and Development Work

1.1.5.1 Corrector Plate

From TDR Version August 2000: This design option exploits the possibility of reducing the spherical aberration, which is not eliminated by the diaphragm, by putting a corrector plate at the center of curvature of the mirror, turning the FD into a true Schmidt camera. This approach can be reversed and the use of a corrector plate is then seen as a way of increasing the diaphragm aperture while keeping the spot size under control, thereby increasing the effective light collection area of the detector, which increases the S/N ratio.

The first option is a corrector plate of Type II [7] having:

(a) radius: 1.13m (compared with a baseline design diaphragm radius of 0.85m)

(b) thickness of the center of the plate, $T(0)$=10 mm

(c) tolerance: +/-1 mrad on the normal to the surface of both mirror and corrector plate.

The material would be UV-transmitting acrylic (refractive index 1.49). Such a corrector plate would increase the effective light collection area by 90% while keeping the spot diameter under 0.6^{o} [1,2,8]. The cost would be under US$500 per corrector plate. The fabrication technique is under study. (September 2001: This option has been abandoned).

Alternatively, there is an option of using a corrector ring or annulus. The possibility of correcting for spherical aberrations and/or increasing the diaphragm radius while keeping the spot size controlled, also reducing fabrication difficulties and costs, prompts the study of this alternative design with the Schmidt correcting device having the shape of a ring covering the outer region of the diaphragm.

For this option,

(a) inside diameter: 1.7m

(b) outside diameter: 2.2m

(c) shape: Type II (see above)

Here the spot diameter is kept under 0.6^{o} while increasing the light collection area by almost 40% [9]. (September 2001: Progress on this option is described in section 1.1.4.1.2.2)

An alternative corrector plate method is the Maksutov-Bouwers design in which the corrector plate is a thick miniscus lens. The Puebla group have studied 4 different variations [10]. In these designs, the corrector plate does not disrupt the spherical symmetry and there is no chromatic aberration introduced. Like the other Schmidt corrector plates, it remains to be demonstrated that it is practical to incorporate such a lens in a camera of this large size that must operate for many years. (September 2001: this alternative has been abandoned).

1.1.5.2 Interference filters

From TDR Version July 2000: Wide band interference filters are an interesting alternative to absorption type filters used by the Fly's Eye and HiRes [11]. Such interference filters can be designed to have a nearly flat transmittance of 85% from 320-410 nm. We have done angular dependence tests on some interference filters not designed specifically for Auger. For a shift of 25 degrees in incidence angle, we have observed a 12 nm shift of the transmittance curve in the case of ZrO_2 SiO_2 16-layer structure with transmittance around 85% in the UV region and up to 600nm, while the transmittance drops above this wavelength.

In the case of a 16 layer structure of a WO_3MgF_2 filter, we have achieved an average transmittance of 74% in the range 350-400nm. The transmittance curve shift for a 15^o angle is less than 6 nm and the peak transmittance value is roughly invariant. By redesigning the layer thicknesses, we hope to achieve a steeper drop of transmittance above 415 nm. This can be done by adding about 4 layers of film on the other side of the substrate. At any rate, the average transmittance in the range 415 to 600 nm is about 9.5%. One has to take this average value of transmittance in the visible range to consider the effect on the S/N ratio. In the range above 600 nm, where the transmittance is rising again, there seems to be no concern since the PMT quantum efficiency (Philips XP3062) is greatly reduced. At any rate, by adding 4 layers of coating, the transmittance in this red range can be reduced to a certain extent if it is considered necessary after detailed Monte Carlo study.

The mechanical stability of the wideband filters depends on the construction method. Of the two most widely used methods, electron-beam deposition and reactive DC sputtering, the former produces more porous thin film multilayers. This may be prone to humidity attack if a special protection procedure is not followed. The effects of humidity could be significant if the filter has significant porosity due to the construction method and in the absence of protective coating. The second method gives better quality filters (less porous). However, it is normally a slower method and most probably more expensive and needs stricter control of the oxygen flow in the process chamber.

We hope to study both methods, and in particular we would like to have more filter samples produced by sputtering to assess the merits of this method.

For the sake of mechanical stability of the filters, we suggest that they are produced, if we use the e-beam deposition method, by substrate heating. In this case, a specific crystal phase dominates which leads to more favorable mechanical compatibility of the heterostructure to be chosen (most probably ZrO_2SiO_2). These thoughts are supported by work of Dobrowofsky et al. [12].

Strains can produce long-term aging in the filters and thus they should be well understood. A method for measuring the strains and stresses must be selected ensuring it is accurate, easily available, inexpensive and fast. One may examine the possibility offered by Raman scattering techniques [13].

Cost considerations are quite intricate. If some institutions participating in Auger have the infrastructure (coating plants) to produce wide-band interference filters, then the filter may cost less per given area than if the coating equipment needs to be purchased. The same is true for other types of filters such as absorption filters. If they can be produced by private companies or by research institutes in a way that meets the technical specifications, then this is better than if only one or two companies exist which give poor satisfaction to the specifications for the fluorescence detector. From the existing data on

the absorption filter of HiRes, it seems that the filter approaches Elbert's maximum "improvement factor", but this maximum performance factor evaluated for an "ideal wide band interference" filter is perhaps somewhat underestimated. This is the opinion of E. Fokitas, since it may be possible to produce interference filters with UV transmittance better than the 80% assumed by Elbert. It cannot be excluded that interference filters of around 85% transmittance between 320-420nm are possible.

September 2001: The development of a suitable interference filter is too far behind schedule to be a realistic alternative to commercially available absorption filters which have already been tested successfully in the prototype systems. Further development of this filter option has therefore been abandoned.

1.1.5.3 Filter at the camera

Positioning the optical filter in the diaphragm (ie the reference design) has some clear advantages:

We need a window there and we don't want additional light losses (at least 10% for any window without anti-reflective coating).

The range of incidence angles extends only to 21^o at the corners of our field of view (versus a cone of 27^o half-angle for a pixel's view of the illuminated mirror portion).

The alternative of putting the filter directly in front of the camera also has some important advantages:

Less filter area is required (less than $1m^2$ versus $2.3m^2$, or $3.8m^2$ with corrector annulus).

Every pixel has the same distribution of incidence angles. (This is strictly true only if the filter follows the camera curvature. The cone is not centered on normal incidence if the filter is a plane in front of the camera.)

The filter is not subjected to outdoor temperatures and abrasives.

The filter is decoupled from the corrector plate option.

However, the filter in front of the camera should be made of only one piece of approximately 90cm x 90cm, which is not a standard commercial size. In fact, several pieces of glass would introduce at their borders inefficiencies on the camera.

The requirement of a spherical shape for a single glass piece implies additional cost for the production, and care for the glass thickness.

Instead of a plane sheet of filter in front of the camera, a filter could be cut for each PMT and bonded to the PMT face, thereby eliminating additional surface losses in the filter. It should be noted that, in this case, there are some large incidence angles due to photons that have reflected off the mercedes walls. It should be verified that the filter is effective also at large incidence angles.

If the filter is not placed at the diaphragm, a window of UV transparent glass must be introduced. The cost of the glass and the mechanical structure to hold it in place should be taken into account.

The option of taking the filter out of the diaphragm does not show a clear cost or physics advantage. It should be considered only if a deterioration of its performance due to environmental damage is observed during the engineering phase.

1.1.6 Prototype Plans and hybrid engineering

1.1.6.1 Objectives

The engineering phase is intended to be a learning experience in which we discover flaws in the design, find the best design, develop optimal fabrication methods, refine the analysis procedures, and demonstrate that the hybrid shower detection capability meets the project's requirements. Our goal is to construct a world class fluorescence detector that measures air shower longitudinal profiles with high sensitivity. It may be useful to state some specific aspects of this goal:

Optics demonstration. Independent of event triggering and longitudinal profile measurements, we wish to prove that the telescope achieves the expected quality of optical performance. One way to do this is to cover the camera with a stretchable white material, then fly a bright light around in the field of view with an airplane. The spot should be clearly visible on the white focal surface (if the optical filter is not present), and a normal video camera can document the optical performance. Captured still frames can be used to measure the effective spot size at different parts of the field of view. This should verify that the spot is circular and independent of position in the field of view, and not larger in diameter than 1/3 of the pixel diameter. (This general procedure was used successfully to test a Schmidt diaphragm at the dual mirror test stand in Millard County.) An alternative to the airplane and bright light is to make multiple CCD camera time exposures during the transit of a bright star or planet across the telescope's field of view. The star or planet moves less than 0.1^{o} during a 20-second CCD integration, and that may provide ample signal-to-background for determining the image of the point source.

Laser profiles. A pulsed laser beam mimics an upward-going shower in the sense that light is emitted (scattered in this case) from a narrow segment that moves along the axis at the speed of light. The longitudinal profile seen by the telescope generally decreases with altitude because the beam attenuates and the density of scatterers decreases with altitude. Wispy clouds or smoke plumes show up as bumps on the longitudinal profile. If the laser pulse is produced by a lidar system, the amount of scattering is recorded by the lidar as a function of altitude. The longitudinal development measured by the telescope should agree with what the lidar records. (Some difference might be expected if the total phase function changes with altitude, and that can occur as Rayleigh scattering becomes dominant over aerosol scattering.) The first objective is to see a continuous longitudinal profile that tells us that the pixel-to-pixel calibration is sensible and that we are recording sensible signals.

Event trigger tests. Laser pulses can also be used to test the trigger sensitivity of the telescope. On a very clear night, the amount of light scattered from a pulse can be reliably calculated as simple Rayleigh scattering. By measuring the pulse energy, the light flux at the detector can be well estimated. In this way, one can approximately simulate a shower of a given energy at any distance. This allows a quite rigorous demonstration of trigger sensitivity. Assuming a 15-km attenuation length, a laser beam pulse at 350nm requires 21 μJ/EeV to simulate the light production by an air shower at its maximum size.)

Shower-detector plane reconstruction. By varying the position and pointing direction of such a pulsed laser beam, we can evaluate the accuracy of the telescope in determining the geometry of the shower-detector plane. A roving laser scope will be used for this. A lens in front of the laser can be used to make the beam diverge as a crude simulation of a shower's lateral distribution.

Timing tests. For a known laser geometry (produced with the laser scope as above), one can calculate exactly the time when the center of the spot passes each pixel center. his should be compared with the

pulse-center time determined from each pixel's FADC trace. Alternatively, one can calculate from the pixel trigger times at what instant the laser must have fired at its known location. A GPS and flash detection system at the laser site could be used to test those predictions. Note that this is a good test for hybrid reconstruction accuracy. Picking out the correct axis within the shower-detector plane relies on getting a prediction from the FD pixel times for the shower front arrival at any ground position. We can demonstrate our ability to do this accurately using pulsed lasers in this way.

Monocular shower detections. The telescope will observe a large number of air showers, mostly lower energy showers landing near the detector. The reconstruction of those showers will be handicapped without surface array information. But the shower-detector plane distribution and the light intensity distribution are calculable from the known isotropic cosmic ray intensity.

Hybrid showers. Most important is to demonstrate that we do indeed measure the expected number of showers in coincidence with the engineering surface array. For the one prototype telescope operating with a 10% duty cycle with the 40-tank engineering array, Fick's simulations give the following expectations for the event rate per year above a given energy:

Energy (EeV)	0.5	1	3	5	10	30
Events/year	683	386	78	31	9	1

Options testing. It should be emphasized again that the purpose of the prototype is to optimize all aspects of the FD detector. We will compare different types of mirror segments. We will test a Schmidt corrector plate to find out if it can increase our light-collecting power without degrading our spot size. We will compare different atmospheric monitoring techniques and different detector calibration procedures, so we can focus our resources on the most worthy. We will test and refine all aspects of the detector electronics. We will enhance the data acquisition system and improve the detector simulation and analysis procedures. We will work out any bugs in the communications system and hybrid triggering and data merging. We will find out what features are needed in the eye buildings that have not been anticipated.

1.1.6.2 Prototype building

The prototype telescope will be housed in the building being constructed for the first fluorescence station at Los Leones.

1.1.6.3 Organization, subtask responsibilities, and work breakdown

The FD prototype telescope has been a European initiative since its inception. A collaboration of Italian institutions and the Karlsruhe groups are supplying strong support for the rapid development of the telescope itself. The entire FD engineering phase of the project is still a broad international effort, however. The division of tasks and leadership responsibilities can be expected to change over the years of the detector construction. Levels of support in different countries have not yet been determined. From experience with the prototype detector we will learn the most efficient ways to take advantage of our international collaboration.

Paul Sommers (Utah) was the task leader for the fluorescence detector during the design, prototype development and installation phase assisted by Jonny Kleinfeller (Karlsruhe) as coordinator

of the FD and FDE tasks to complete the prototype telescopes. Hartmut Gemmeke (Karlsruhe) was one of the co-leaders for fluorescence detector electronics until recently.

From April 2001, the task leaders for the fluorescence detector are Jonny Kleinfeller (Karlsruhe) and Paolo Privitera (Roma). Matthias Kleifges (Karlsruhe) and Daniel Camin (Milano) are the present co-leaders for the fluorescence detector electronics tasks. Principal subtask leaders are Hans Klages (Karlsruhe) and Rosanna Cester (Torino) for the mirror system and optics overall, Giorgio Matthiae (Roma) and Paolo Privitera (Roma) for the camera system, and Roger Clay (Adelaide) and John Matthews (University of New Mexico) for calibration and atmospheric monitoring. Carlos Escobar (Campinas) is in charge of developing the aperture system and all its optical components, except for the optical filter which is the responsibility of Rosanna Cester (Torino). Norberto Fazzini is in charge of the telescope buildings. Additional subtasks may be warranted to deal with buildings and infrastructure, diaphragm optics, simulations and analysis, operations and safety, etc.

Responsibility for delivering the various components for the engineering phase are summarized below:

Shutter - Krakow

Diaphragm - Campinas, Karlsruhe, Krakow

Corrector annulus - Campinas, Czech Republic, Karlsruhe, Puebla

Optical filter - Torino

Reference point and mechanical alignment tools - Karlsruhe

Mirror support - Karlsruhe, Torino

Mirror mounts - Karlsruhe, Torino

Mirror segments - Czech Republic, Karlsruhe, Torino

Optical alignment and quality control - Czech Republic, Karlsruhe, Torino, Puebla

Camera system - Catania, Roma

Building - Argentina

Furniture and installation equipment - Karlsruhe

Slow control - Karlsruhe

Calibration - Catania, Colorado, Louisiana State, New Mexico, Utah

Atmospheric monitoring - Adelaide, CBPF, Chicago, Ljubljana, Michigan Tech., New Mexico, Torino, Utah

Detector simulations and data analysis - Adelaide, Campinas, CBPF, Czech Republic, Karlsruhe, Roma, Torino, Utah

Electronics - see FDE section of TDR (section 1.2)

Institutional responsibilities for the various components may also be subject to change based on our experience during the engineering phase of the project. The present agreements for production are:

Diaphragm (with shutter and corrector ring) - Campinas

Optical filter - Torino

Reference point and mechanical alignment tools - Karlsruhe

Mirror support - Karlsruhe, Krakow, Puebla

Mirror mounts - Czech Republic, Karlsruhe, Krakow, Puebla

Mirror segments - Czech Republic, Karlsruhe

Optical alignment and quality control - Czech Republic, Karlsruhe

Camera system - Catania, Roma

Building - Argentina, Karlsruhe

Slow control - Karlsruhe

Calibration - Athens, Catania, Colorado, Louisiana State, New Mexico, Utah

Atmospheric monitoring - Adelaide, Athens, CBPF, Chicago, New Mexico, Ljubljana, Torino, Utah

Detector simulations and data analysis - Adelaide, Campinas, CBPF, Karlsruhe, Krakow, Roma, Torini, Utah, and the whole collaboration.

Electronics - see FDE section of TDR (section 1.2)

1.1.7 Four sites at Pampa Amarilla

1.1.7.1 Layout

The reference design layout is shown in Figure 1.21. The surface detector area is approximately 3000 km^2 with fluorescence detectors on the perimeter on hills called Leones, Morados, Amarilla and Coihueco. The four perimeter eyes will view 180^O of azimuth towards the array.

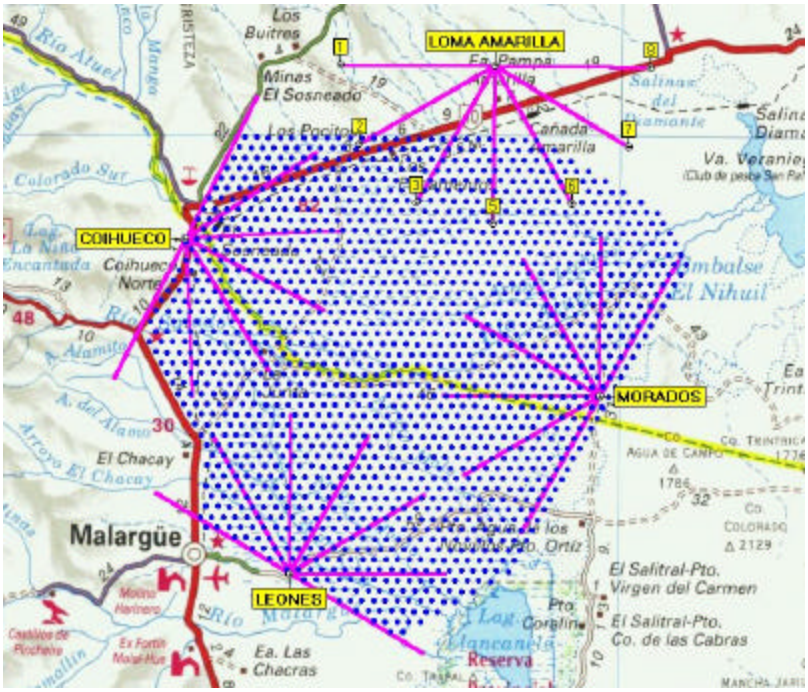

Figure 1.21 The planned arrangement of the 4 fluorescence detectors at the southern site. Four perimeter sites are situated at Los Leones, Coihueco, Loma Amarilla and Los Morados. Each of these sites view 180^O of azimuth. The array shown covers an area of approximately 3000 square kilometres - the spacing of the surface detectors is 1.5 km.

1.1.7.2 Schedule

Construction of the full observatory should commence immediately after the 2-year engineering phase, which began with the ground-breaking on March 17, 1999. Construction of the first eye would then begin in the spring of 2001, and the southern hemisphere observatory should be completed in 3 years (spring of 2004).

1.1.8 Quality assurance, hazard mitigation, and safety

1.1.8.1 Optical testing

Verifying the optical quality of the Auger telescopes is an important task. Calibration work may emphasize an end-to-end calibration which folds together all the optical and electronic components. We need to know precisely the quality of the optical components separately also. Procedures are needed for measuring the optical filter's transmittance as a function of incidence angle and wavelength. How much variation is there over its area? Procedures are needed for measuring the optical quality of each mirror segment. The Puebla group demonstrated a new Ronchi tester at the Morelia meeting. We also need to quantify the alignment accuracy of the mirror segments. It would be good to have a system that allows alignment (and measurement) with the camera in place, rather than relying on light returning to the optical center of curvature. The mercedes reflector efficiencies can be measured in a laboratory. We plan to use star transits or other techniques to monitor their efficiency *in situ.*

1.1.8.2 PMT testing and database recording

The typical PMT characteristics are known from the specifications provided by the manufacturer and by our laboratory tests. The manufacturer shall provide for each tube the following information: photocathode sensitivity at the wavelength of 337 nm, photocathode sensitivity with a Corning blue filter, high voltage needed for a gain of 10^5, and anode dark current at a gain of 10^5. In addition, we have defined a test procedure that is applied to each PMT when it is delivered by the manufacturer. The test is performed on the PMT unit, *i.e.* the PMT with the voltage divider and preamplifier cards soldered onto the flying leads, with an automatic PMT test system [14]. In particular, we check the linearity of the PMT unit and the photocathode uniformity. We measure the gain vs. high voltage, which is needed for a proper grouping of the PMTs with similar gain. The relative PMT gain and the relative photocathode sensitivity at different wavelengths are also measured. We plan to perform these tests at the factory before shipping the PMT units to the Observatory. A fraction of the PMT units will be tested in the collaborating institutions.

The information for each individual PMT unit is collected into a database. The database will also track the PMT characteristics after installation, including calibration measurements performed *in situ.*

1.1.8.3 Failsafe mechanisms

The PMT photosensors have a lifetime measured by the anode charge collection. It is essential that they not be exposed to strong light when the high voltage is on. Under normal operating conditions, the diaphragm will be open only during the dark of night. The shutters will not be opened before the end of twilight after sunset and will close again before the start of twilight in the morning. The shutters will be electrically-powered mechanical devices, however. They may fail because of electrical failure or mechanical jamming. A sensor (perhaps embedded between mirror segments) should automatically switch off high voltage if a significant amount of light persists for an appreciable length of time.

Even without high voltage, the camera can be damaged by high light levels. If direct sunlight is focused on the camera, it could burn up despite the optical filter in the diaphragm.

Another battery-operated sensor should be mounted outside the building. It should detect the shutter position as well as light level. If it is light outside and the shutter is not closed, then it should cause the release of a curtain that falls behind the diaphragm to prevent the outside light from reaching the mirror.

1.1.8.4 Safety equipment and operation procedures

The fluorescence detectors will conform to the Project's safety standards for buildings, electrical equipment, fire prevention, etc. Special attention is needed for the eyes because they are expected to be run remotely with a lot of high voltage and electronic equipment concentrated within a single building. We require strict adherence to safety standards for wiring, conduits, circuit breakers, etc. Smoke detectors should be installed with the capability of shutting off all non-essential power and broadcasting alarms.

The detector operating instructions will emphasize safety issues so as to minimize the possibility of accidents. Personnel should work in teams of 2 or more persons at remote sites.

The use of high-power UV lasers constitute a severe danger of eye damage both for Auger personnel and unwitting bystanders. In particular, safeguards are essential to avoid any possibility of blinding an aircraft pilot in the area. The use of beam divergers might solve the problem. If not, a simple radar system may be warranted to identify any aircraft in the danger volume.

A simpler method has been suggested. The idea is to mount a photosensor with about 10^{o} field of view on the laser. Whenever the sensor detects a light flash (possible airplane strobe), it disables the laser for one minute. A laser pulse would then only be possible if the solid angle around it has been clear of airplanes for at least one minute. High-power UV lasers should be mounted in such a way that their beams can never hit the eye of bystanders at ground level.

1.1.9 Calibration System

1.1.9.1 Reference Design Specifications

1.1.9.1.1 End-to-end calibration

The reconstruction of air shower longitudinal profiles and the ability to determine the total energy of a reconstructed shower depend critically on being able to convert an ADC count to a light flux for each pixel that receives a portion of the signal from a shower. To this end, it is highly desirable to have some method for evaluating each pixel's response to a given flux of incident photons from the solid angle covered by that pixel, including effects of diaphragm area projection, optical filter transmittance, mirror reflectivity, pixel light collection efficiency and area, cathode quantum efficiency, PMT gain, pre-amp and amplifier gains, and digital conversion. While this response could be assembled from independently measured quantities for each of these effects, the FD calibration group is persuing an alternative method in which the cumulative effect is measured in a single end-to-end calibration.

The technique being developed is based on a portable light source that will mount on the external wall of the fluorescence detector building, filling the diaphragm of a mirror with a uniform pulsed flux of photons and triggering all the PMTs in the camera array. One portable light source will be stationed at each FD building. Cameras will be calibrated one at a time.

This source consists of a pulsed UV LED embedded in a small teflon sphere, illuminating the interior of a 2.5 m diameter cylindrical drum, 1.25 m deep. The sides and back surface of the drum are lined with Tyvek, a material diffusively reflective in the UV. The front face of the drum is made of thin sheet of teflon, which is diffusively transmitting. A silicon detector mounted near the LED monitors the relative intensity of each flash.

The geometry of the source and drum is arranged so that the intensity is independent of position on the diaphragm and uniform over the range of the camera's solid angle. These uniformities of intensity and angular emission are measured in a laboratory using a CCD camera, viewing the drum from a distance of 15 m. Pictures are recorded for several angles of emission from the drum, in the range of the telescope field of view. Software has been been developed for comparing the relative intensities of regions of the drum surface. Current drum geometry gives non-uniformities of less than 5%. The largest non-uniformity is a decreasing intensity with radius on the drum face. While perfect uniformity is desirable, non-uniformities which are small and well mapped over the surface of the drum can be accommodated in analysis.

Ideally, this calibration would occur at many wavelengths in the N_2 spectrum, between 300 and 400 nm, and at several intensities. The design discussed above uses the single wavelength of the UV LED (375±12 nm). It is planned that, as the calibration sophistication evolves, fiber optics will be used to pipe light to the teflon sphere, allowing selection of frequency and intensity from a light source such as a monochromator or filtered xenon source. Currently, the pulses are variable in width, from 500 ns to 7 μs.

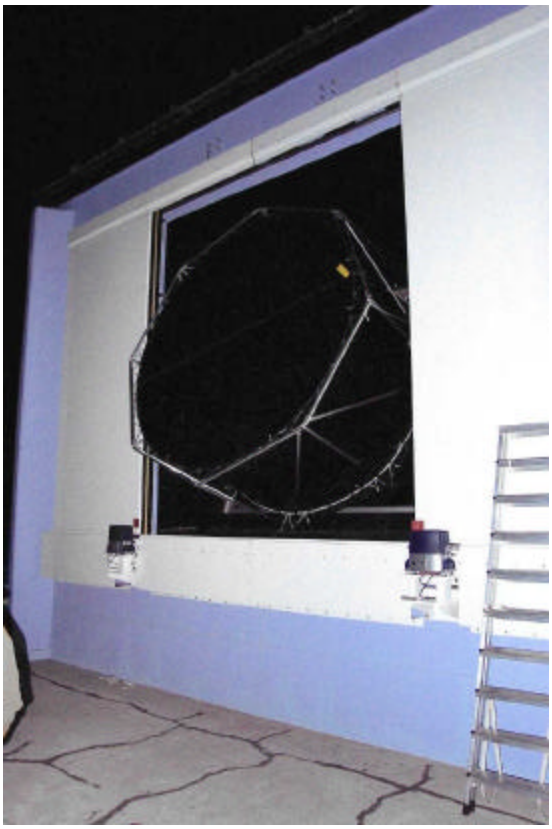

Figure 1.22 Drum calibration device mounted on the outside of the building at Los Leones.

1.1.9.1.2 Calibrating the Drum Using the Central Calibration Facility

While the uniform light source described above provides a means of determining relative responses of the pixels in a telescope, measuring the energy of an air shower requires an absolute calibration of pixels. To accomplish this, the drum calibration must also be absolute.

To establish this absolute calibration, a small optics lab will be established at the central Auger assembly building. The basic lab components will include a molecular deuterium UV light source, a diffraction grating monochromator, beam splitter, and a NIST-calibrated UV silicon detector. This Si detector will be the reference standard for the calibration. The lab components will be used to transfer the NIST calibration from the Si detector to a PMT and then to the drum. (The low sensitivity of the Si detector makes it unusable for directly calibrating the drum.)

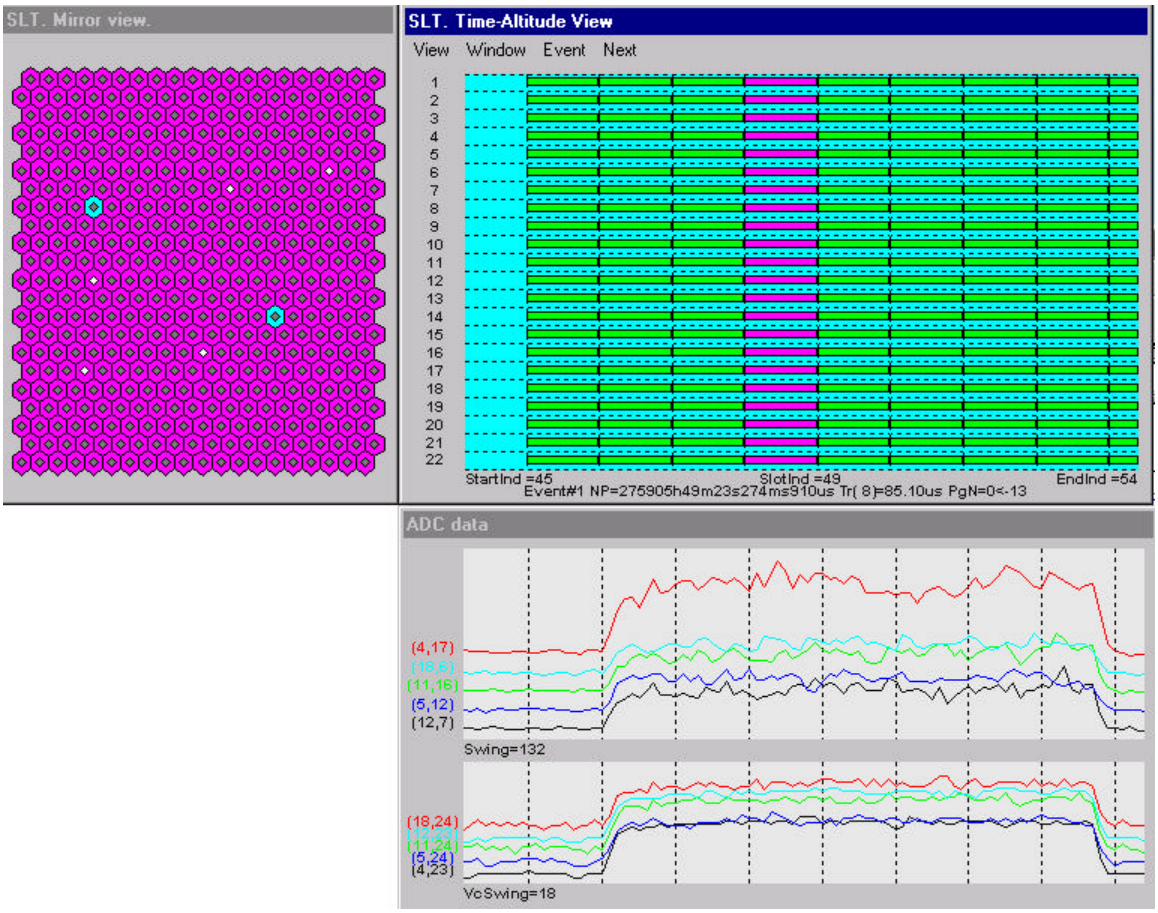

Figure 1.23 The online display from the data acquisition software showing the results of a single 7 μs pulse from the calibration drum when mounted in the mirror aperture. At the top left is shown the pixel array, indicating that all pixels in the camera (except two known dead channels at this time) went above threshold. Top right contains timing information for the triggers in each row of pixels. Bottom is the response from several randomly selected pixels in the camera (dotted pixels in top left) for the seven 1 μs ADC bins. Such events can be written to disk at about 10 Hz; several thousand events at 5 pulse widths from 0.5 to 7 μs have been written to disk for analysis.

The first step in the calibration will be made using techniques paralleling those used by NIST [15], where the detector to be calibrated is compared to the known standard detector under identical conditions. The monochromator will scan UV wavelengths between 300 and 400 nm using the molecular deuterium source as input. The beam splitter sits at the monochromator output. With the Si reference standard and the PMT monitor viewing the two beams from the splitter, detector outputs as a function of wavelength can be compared. (To allow for the ~10^6 difference in detector sensitivity, a neutral density filter is required on the PMT beam.) A ratio of the outputs (including the measured nuetral density filter factor) at a given wavelength gives the calibration of the detector relative to the standard at that wavelength.

The uncertainty in the calibration of the PMT will include the uncertainty in the UV Si detector calibration, provided by NIST. The wavelength-dependent efficiency uncertainties are given in Table 1.2.

wavelength (nm)	uncertainty (%)
200	13.02
250	1.36
300	2.06
350	1.68
400	1.46
450	0.38
500	0.38

Table 1.2 NIST wavelength-dependent efficiency uncertainties for the UV Silicon detector.

Once the PMT response is known, it can be used to calibrate the (low) intensity of the drum. If the PMT is placed far from the drum, photon incidence angle effects are minimized. It has been shown in the lab that the response of a suitable PMT to light emitted by UV LED pulses in the drum can lead to measurements which are good (statistically) at the 1% level.

The uncertainty in the overall calibration is expected to have contributions from uncertainties in the stability of the LED-monitoring Si detector in the field, the uniformity of the diffuse surface of the light source, and the cumulative uncertainties of calibrating the drum relative to the UV Si calibration detector through use of the PMT. Of these, the first and the second, which can be minimized in software, are expected to be small. The last is expected to dominate the overall uncertainty. Since each of these is expected to be less than 5%, a total absolute uncertainty on the order of 8% or less is expected.

1.1.9.1.3 Relative Night to Night Calibration

The end-to-end calibration using the flat field drum illuminator (described above) will be done on a periodic but not on a nightly basis. To track the PMT response between end-to-end calibrations, a relative optical calibration system provides light pulses to three computer-selectable places in each FD telescope:

at the mirror center with the light directed at the camera;

at the middle of the 2 sides of the camera with the light directed at the mirrors;

at the entrance aperture with the light directed at a reflector (TYVEK screen or TYVEK targets on the telescope doors) to direct light back into the telescope entrance aperture.

The light is distributed from a programmable light source (at each FD site) via optical fibers. Typically the optical fibers end with a diffuser to equalize the light directed to the PMTs. The geometrical

projection effects (for the fiber/diffuser at the mirror center) can be calculated, thus this source provides a relative calibration of the camera pixels within a single camera.

The programmable light source provides light at different intensities and/or wavelengths using neutral density and/or interference filters respectively. The light source is a xenon flash bulb with a characteristic pulse time of ~ 1μs matched to typical fluorescence signals in the PMTs. The high pulse to pulse stability of a xenon light source results in light calibration signals with RMS widths < 1%. Light source intensities are monitored and recorded in the calibration data base.

1.1.9.1.4 Principle of electronic gain determination[i]

The absolute optical gain as determined with the Drum Calibration relates the ADC output (in ADC counts) to the photon flux (at fixed wavelength of 370nm) through the telescope aperture. In contrast, the Electronic gain defines for each pixel the ADC signal amplitude per photoelectron current at the PMT's first dynode. The ratio of both quantities - the optical gain and electronic gain - depends only on geometry of the telescope (shadowing effects, reflectivity), PMT quantum efficiency and collection efficiency. It is constant as long as these conditions are kept unchanging.

The electronic gain – and thereby the optical gain - can be adjusted by changing the PMT's high voltage or by programming the gain of analog amplifiers on a per pixel basis. The adjustment made as part of the Drum Calibration is such that the response to light pulses is uniform for all pixels. If the ratio of optical to electronic gain is constant due to unchanging conditions, it is sufficient to measure the electronic gain to predict the absolute optical gain. Since the electronic gain is only weakly depending on the photon wavelength, this measurement can also be carried out with a blue LED of a different (470 nm) wavelength.

A statistical method to determine the electronic gain based on a fluctuation analysis of the camera response was presented in [xx]. It allows a fast measurement of the electronic gain with only a few 10, but relatively long square light pulses from a LED. The top of the signal recorded by the ADCs has an exponential decrease due to the AC coupling of the PMT and amplifier as shown in figure xx. The electronic gain G is calculated by

$$G = \frac{D}{M} \cdot \frac{10}{(1+u_g) \cdot 2F} \cdot$$

Here $(1+u_g)$ is the single photoelectron resolution, F is the noise equivalent bandwidth of the analog chain, M - the amplitude of the recorded signal and D - the variance of the recorded samples.

For now, the single photoelectron resolution is assumed to be equal 1,412 for every PMT, but we have also plans to measure this value for each PMT individually in a special measurement with a much higher PMT high voltage. The noise equivalent bandwidth F is measured periodically (quarterly) and the results

[i] TDR_LEDcalibration.doc

are stored in the calibration data base as array F(22,20). The measurement of F with 1% accuracy (rms) requires about 500 LED pulses and a more sophisticated analysis.

Relative Night to night calibration with the LED

The measurement of the electronic gain with statistical method will be performed for each pixel on a nightly basis. The DAQ will trigger on 50 LED shots which are sufficient to achieve a 1 % statistical error in the gain determination. The results are stored in a data base as array of pixel gains G(22x20).

In addition, the nightly recorded data are analyzed to find changes in the calibration system. The LED amplitude is recorded with a Si photodiode pulse by pulse. The relative optical response of the camera (array OR(22,20) is calculated by the average of the recorded ADC amplitude divided by the photodiode signal. Changes of the optical response for all pixels in all cameras indicate problems with optical system of the calibration. Changes for single pixel not correlated to changes of electronics gain of that pixel indicate variations in the PMT characteristic.

The electronic is equipped with 2 virtual channels per camera column to increase the dynamic range. These extra virtual channels (VC) are the analog sum of the 11 non-adjacent pixels which are amplified with a factor 30 lower gain. Ideally, each pixel contributes to the associated virtual channel with the same weight. However, imperfections in the analog electronic can cause deviations and it is thus required to determine the ratio of the electronic gain for high gain (normal channel) and low gain (virtual channel) per pixel.

The determination of this ration requires successive pulses in individual pixels exploiting the potential of the electronic test pulser available for every channel. Therefore the nightly calibration will be complemented by a test pulser run which verifies all front-end functions and calculates the array GV(22,20) holding the ratio of gains in normal and virtual channel per pixel.

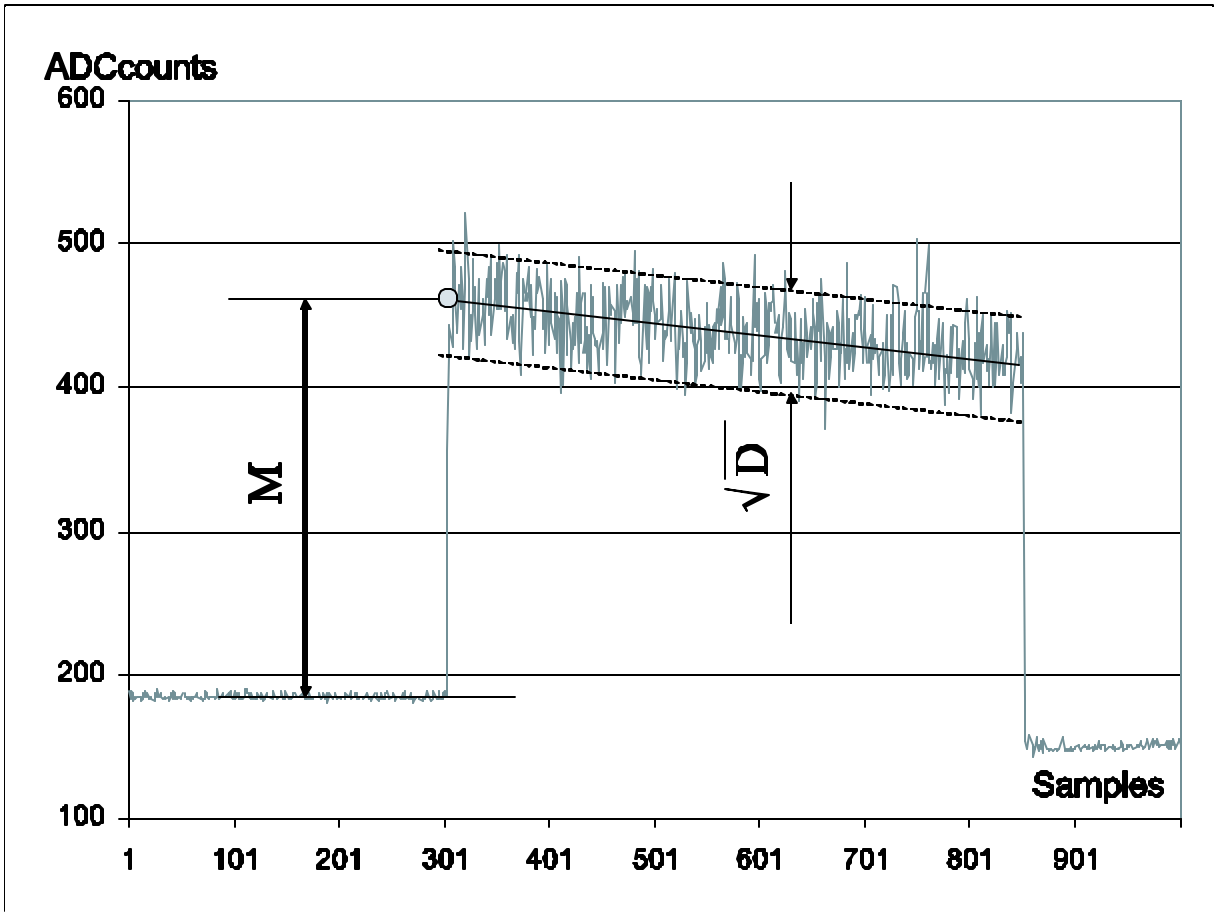

Figure xx: Recorded signal of a pixel in response to a squared LED pulse. The electronic gain is proportional to the ratio of the variance D and the pulse amplitude M.

References:

1 A. Menshikov, M. Kleifges, H. Gemmeke, "Fast Gain Calibration of Photomultiplier and Electronics", IEEE-TNS Vol. 50, No. 4 (Aug.2003) 1208-1213

1.1.10 Atmospheric monitoring

The observed light intensity, I, from a shower is reduced from the light intensity of the fluorescence source, I_0, by geometric and by transmission factors. The relevant transmission factors are T^m and T^a corresponding to *molecular* and *aerosol* scattering of the light in the atmosphere between the air shower and the fluorescence detector(s). There are also higher order corrections from multiple-scattered light and scattered air Cherenkov light (that increase the observed signal somewhat). Uncertainties in the source light intensity will arise from uncertainties in the (correction) factors. To minimize these atmospheric uncertainties, fluorescence experiments are located in dry desert areas with typically excellent visibility (*i.e.* small corrections).

The scattering of light in a pure or molecular atmosphere is from Rayleigh scattering. The scattering of light on much larger scattering centers in the atmosphere called aerosols is referred to as Mie scattering. In practice the Rayleigh scattering related corrections, while large, can be made with precision using conventional atmospheric data: the temperature and pressure at the fluorescence detectors, and the adiabatic model for the atmosphere. In contrast the corrections related to Mie scattering, while typically less than the Rayleigh corrections, are *a priori* unknown. Thus most of the atmospheric monitoring is focused on the aerosol (Mie scattering) component.

In a 1-dimensional model of the atmosphere (not un-typical of the night time atmosphere in large, desert valleys at locations well away from the valley walls) the aerosol transmission correction needs only the aerosol vertical optical depth (AVOD(z)) to height z above the fluorescence detectors. This will be measured using a number of different instruments. Multiple, and in some cases redundant, measurements provide a monitor of non-1-dimensionality as well as cross checks and a monitor of systematic uncertainties. In all cases the measured quantities include both aerosol and molecular contributions. The aerosol values are obtained by subtracting the molecular (Rayleigh) contributions.

1.1.10.1 Reference Design Specifications

1.1.10.1.1 Weather recording

Automated weather stations will be located at each of the FD sites (eyes). They will provide a record of the local temperature, pressure, wind speed and direction, and humidity. The temperature and pressure are essential to define the *Rayleigh* atmosphere. Wind speed (and direction) are important for safety interlocks for the FDs. Humidity is relevant for the IR cloud cameras and provides information on the formation of fog.

1.1.10.1.2 Horizontal attenuation

The horizontal attenuation length will be measured at 1 hour time intervals and along 3 (independent) light paths across the Auger Southern array. Thus they will provide information on site and instrument-related systematic uncertainties in the horizontal extinction length. Each light path includes a Hg-vapor light source and a CCD based receiver. The receivers are ~50 km from the source to minimize the uncertainty in the horizontal attenuation length measurement from variations in the source brightness or photometer sensitivity. Measurements will be done at 4 wavelength between 365 and 546nm. These measurements, combined with the local temperature and pressure, will determine the aerosol horizontal attenuation length at 365nm and the wavelength dependence of the attenuation length.

1.1.10.1.3 Vertical aerosol profile

The observed fluorescence light signal must be corrected for the finite transmission of light from the extensive air shower to the fluorescence telescopes. To make this correction we need to know the cross section weighted, vertical profile of the atmosphere, and in particular of the aerosols. The plan is to use scattered laser light as a light source to monitor the atmosphere. By using steerable laser beams, the light sources can be positioned to make a measurement of the vertical optical depth versus height, *z*, above the fluorescence eyes. In practice this will be done using backscattered LIDARs. Backscattered LIDARs will be installed at each of the three fluorescence sites on the periphery of the Auger ground array. Each backscattered LIDAR consists of a pulsed, 355nm, laser beam and a receiver telescope. Comparison of the three LIDAR results will monitor site and instrument related systematic uncertainties in the optical depth measurements.

1.1.10.1.4 Aerosol phase function

The observed light from an extensive air shower includes both the air fluorescence signal plus some Cherenkov light (mostly in a few degree cone centered on the air shower axis). Through scattering of the Cherenkov light in the air, some of the Cherenkov light appears as a background into the fluorescence data. To estimate the fraction of Cherenkov light scattered on aerosols we need the aerosol extinction length, at height *z* above the fluorescence detectors, and the aerosol phase function (normalized aerosol differential scattering cross section) for scattering angles $\geq 10^{O}$ (from the initial light direction).

The observed light from an extensive air shower also includes a contribution of multiple scattered light. This will be true for the air fluorescence signal and for the Cherenkov background light. In making a correction, it is most important to know the Mie phase function at forward scattering angles where Mie dominates Rayleigh scattering.

In the constant composition, 1-dimensional model for aerosols, it is sufficient to measure the aerosol phase function at the altitude of the fluorescence detectors. The measurement can then be made using a near-horizontal, pulsed light beam directed across the field of view of one of the fluorescence sites. As each fluorescence detector views $\sim 180^{O}$ in azimuth, even a fixed direction light beam will allow the aerosol phase function to be measured over most of the range of scattering angles. This will be done using a dedicated light source located near two of the Auger fluorescence sites. In addition LIDAR beams, from one fluorescence site directed across the field of view (and at near grazing incidence to) adjacent fluorescence sites, provide a good measurement of the small angle aerosol phase function.

1.1.10.1.5 Cross Checks

To monitor and to help minimize systematic uncertainties, all of the atmospheric monitoring measurements are made in at least two independent ways. For example the horizontal extinction length measurement will be compared with horizontal LIDAR measurements. The aerosol optical depth measurement will be compared to measurements from a dedicated star monitor. In addition laser *side* scattered light from the LIDAR at one fluorescence site will be observed by the fluorescence detector at a different fluorescence site. A comparison of the predicted *versus* observed signal (as a function of

time) provides the essential cross-check of the aerosol model and the ingredients of the model: the horizontal extinction length, the vertical profile of aerosols and the aerosol phase function.

In addition spatial variations in the aerosols are monitored using the 3 different horizontal attenuation length light paths and by the azimuthal variations in the backscattered LIDAR measurements at a given site and by differences in the vertical optical depth as measured at the 3 LIDARs.

1.1.10.1.6 Cloud Monitoring

The presence of cloud is a key factor in the operation of the FD system. It can determine the effective aperture of the system, and the presence of broken cloud between the shower track and an eye can distort the apparent longitudinal development of individual showers. Cloud can be detected at night in the absence of terrestrial light sources by its emission in the infra-red due to its higher temperature than the night-sky background. Apart from the highest and coldest cloud, such detection can be readily achieved for cloud at high at high elevation angles. Close to the horizon, particularly in humid conditions, detection against the warm atmosphere may be more difficult. The plan is to install infra-red (in the vicinity of 10μm) cameras at each of the FD eyes, and to scan the sky with them using a pan and tilt drive approximately every 10 minutes. They will provide each FD pixel with a cloud/cloud-free decision and, with a 0.2^{O} angular resolution, will be used collectively to triangulate sparse cloud over the array fiducial volume. A test image is shown in Figure 1.24.

Figure 1.24 A cloud image taken with a Raytheon Series 2000B camera from the top of the physics building in Adelaide - looking north-east. Its a pyroelectric 320 x 240 pixel camera sensitive to 7-14μm infra-red radiation. A negative image is shown - dark (cloud) areas are warm compared to white (clear sky) areas. The image shows cumulus cloud low over the Adelaide Hills - at least 10 km distant. Some closer cumulus is evident in the middle of the image. This foreground cumulus is in front of some higher altitude diffuse/cirrus type cloud (faintly visible in the upper centre of the image). On the left is part of the physics building and in the lower right a construction crane. The horizon is the Adelaide Hills.

1.1.10.2 Balloons[ii]

The evidence of various atmospheric influences on the development and detection of EAS using the fluorescence technique demands detailed measurements of the atmospheric conditions at the location of the Auger experiment [1]. In this part, the technique of measurements is described for obtaining atmospheric profiles concerning the molecular atmosphere.

At the Pampa Amarilla, periodical radio soundings are performed covering all seasons and daytimes with an emphasis on measurements during nights. Radio soundings are a common meteorological procedure for acquiring data about air temperature, air pressure, relative humidity of air, wind speed and wind direction in dependence of height. Radiosondes are small, full automatic sensors which are launched with helium filled balloons, see Fig. 1.

The size of the helium filled balloon at ground is about 1 m³ and between the balloon and the sonde is a small parachute for retarding the falling velocity after the balloon has burst. The radiosonde of type DFM-97 with GPS option itself is a product of the company *Dr. Graw Messgeräte GmbH & Co* [2]. The measured data are permanently transmitted from the radiosonde to the receiver ground station GK-90C [2]. The transmitting frequency with a bandwidth of 15 kHz is selectable between 402 - 406 MHz, in steps of 20 kHz. The range of sensor accuracy is laid out for altitudes up to 40 km a.s.l. and the transmission range is more than 250 km. In Figure 2, a detailed view of the radiosonde with its different types of sensors can be seen.

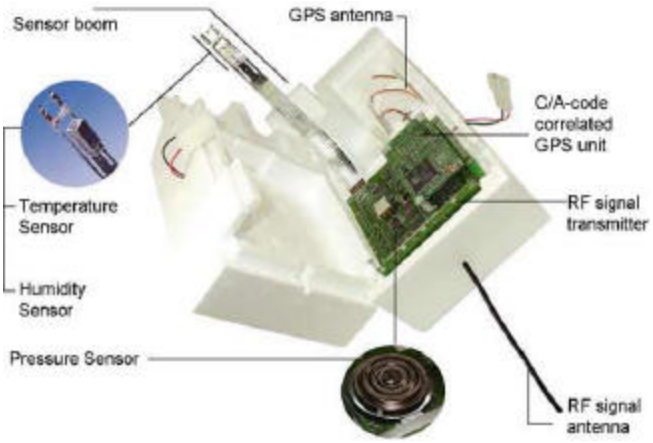

Figure 2: Opened radiosonde with all types of sensors.

During the measurements performed at the Pampa Amarilla, the sets of data are stored every 3 – 4 seconds on average, but at least every 8 seconds. This ensures values in height steps between 3 m and 50 m, with an average

[ii] TDR_Balloons.doc

Figure 1: Radiosonde launched with helium filled balloon.

step size of approximately 20 m. A set of data consists of eight parameters which are time since launch, air pressure, air temperature, relative humidity of air, wind speed, wind direction, GPS height, and geopotential height. The balloon rate of climb depends strongly on pressure and wind conditions as well as the balloon filling pressure ranging between 100 m/min and 500 m/min with an average of roughly 200 m/min. The upper limit of the measurements is given by the height of balloon burst. Typical heights around 22 km a.s.l. can be reached with a maximum for the highest balloon of 28 km a.s.l. up to now.

The following Table 1 summarizes some technical details about the sensors of the radiosonde which has in total a weight of 225 g.

Data Type	**Error**	**Resolution**	**Useful Range**	**Measurable Range**
temperature	< 0.2°C	0.1°C	-80°C to +44°C	-90°C to +80°C
rel. humidity	< 5 %	1 %	not specified	0 % to 105 %
pressure	< 0.5 hPa < 1.0 hPa	0.1 hPa 0.1 hPa	5 hPa to 200 hPa 200 hPa to 1080 hPa	2 hPa to 1100 hPa

Table 1: Accuracies of the radiosondes [2].

The used transmitter has a deviation smaller than 5 kHz with a typical power of 20 dBm or 100 mW. The maximum power is below 21 dBm. The receive antenna is omnidirectional with 3.5 dBi on the horizontal plane. The radiosonde is standard with a C/A-code-correlated GPS receiver for evaluation of

the exact position of the radiosonde. The position information is calculated by the GPS module in the radiosonde. The position is transmitted to the ground station, where it is corrected with the stationary GPS signal of the ground station (differential GPS). Additionally, the geopotential height is acquired.

Bibliography

[1] B. Keilhauer, Auger Technical Note GAP-2003-107 (2003) **OR**
Forschungszentrum Karlsruhe, Wissenschaftliche Berichte, FZKA 6958, ISSN 0947-8620 (2004)
B. Keilhauer et al., Proc. 28th ICRC (Tsukuba), Vol. 2, 879 (2003)

[2] Dr. Graw Messgeräte GmbH & Co., Nürnberg (Germany), www.graw.de

1.2 FD electronics and software

Overview

The main tasks of the telescope electronics are to shape the PMT signals from FD cameras, digitize and store them, generate a trigger based on the camera image and initiate the readout of the stored data. A computer network compresses the data, refines the trigger decision, gathers data of the same event from different telescopes and transfers it to the central computing facility CDAS.

The organization of the front-end (FE) electronics follows the structure of the telescopes in the FD buildings. Each of the 24 telescopes is readout by one FE sub-rack through its associated Mirror PC. Each sub-rack covers 22 x 20 pixels of the camera and contains 20 Analog Boards (AB), 20 First Level Trigger (FLT) boards and a single Second Level Trigger (SLT) board.

The contradicting requests of the experiment are a challenge for the design [16]:

- low price,
- good testability to achieve remote operation and low operation costs,
- high reliability and robustness for 20 years of operation,
- absolute time synchronization with the surface array stations below 120 ns,
- flexibility of the triggers to be open to new physics.

The concept for the front-end electronics, the data flow and the data processing rests upon the system requirements. The design uses reprogrammable FPGAs to obtain a *cost-effective* and *flexible* solution whenever possible. The large-scale integration of modern FPGAs allowed a massive parallel solution for recognition of tracks and suppression of background. The supervision and readout task is carried out by low cost PCs under LINUX operating system. Using this concept we are able to fulfill our main design goals - low price and flexibility.

This chapter of the report describes the electronics, the trigger, the computing facilities and the software associated with each of the front-end sub-racks. Figure 25 shows the block diagram of the Fluorescence Station (FS) electronics and readout system. Following the signal chain from the PMT to the central side the system consists of 4 main parts:

a) the camera with 440 PMTs and the head electronics as shown in figure 26,

b) FE sub-racks, 19” VME-like racks containing the analog and digital front-end boards,

c) Mirror subnet, linking the MirrorPCs with the EyePC via a LAN switch, and

d) Eye network to the telecommunication tower and with connections to the FieldPC (used for slow control) and other computers for calibration and atmospheric monitoring.

All these hardware parts and the software are explained in detail in the following subsections.

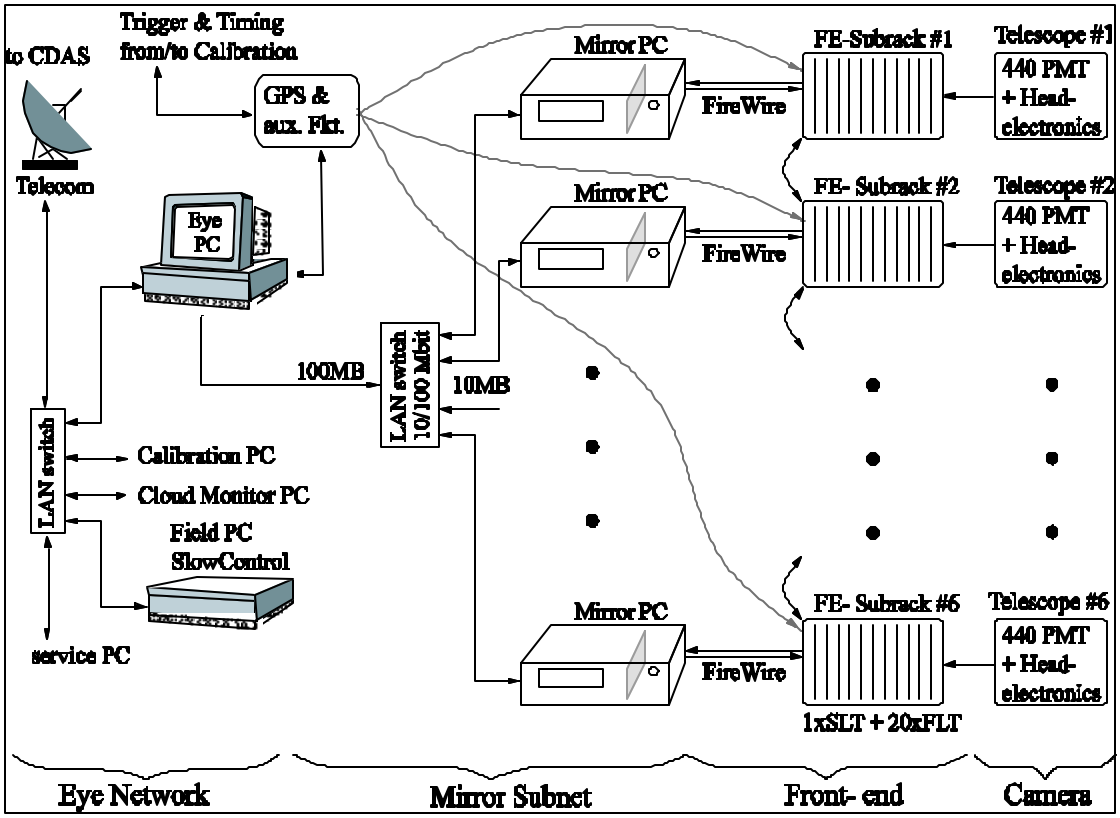

Figure 25: Readout scheme for the FD electronics showing the main components: Eye Network, Mirror subnet, front-end sub-racks and camera.

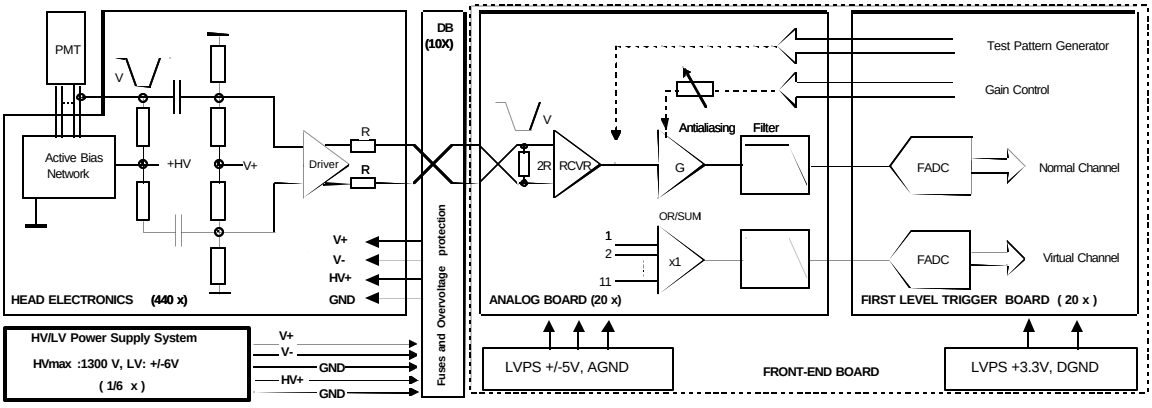

Figure 26: Block diagram of the Analog Signal Processor comprising the Head Electronics, the Analog Board, and the auxiliary systems: Power Supplies and the Distribution Board. There is one set of power supplies for each front-end sub-rack, but only one common HV/LV PS system for all 6 telescopes, with one LV and one HV module for each telescope.

1.2.1 Hardware

1.2.1.1 Head Electronics

Overview

The Head Electronics (HE) is the first unit of the signal processing chain. It converts the PMT current signal into a differential voltage pulse. The pulse is conveyed to the Analog Board using a single twisted pair per channel. A DC biasing level of 1.36 V at the output pins is required to take best profit of the linear range.

The HE unit is mounted directly to the PMT, Fig 1, and its circuitry provides the following functionalities:

- PMT active biasing.
- Signal pre-amplification and twisted pair driving.
- Rejection of common-mode noise.
- HV filtering.

The HE consists of two coaxially interconnected PCBs: the Bias PCB close to the PMT, and the Driver PCB which contains an hybrid driver circuit and the external interface connector. All PCB's are two-sided, circular, 32 mm in diameter, and are interconnected using three highly reliable pins. Use of the hybrid driver circuit avoids use of a third PCB. A plastic piece was designed to facilitate the soldering of the PMT's flying leads to the Base PCB and to ensure mechanical strength.

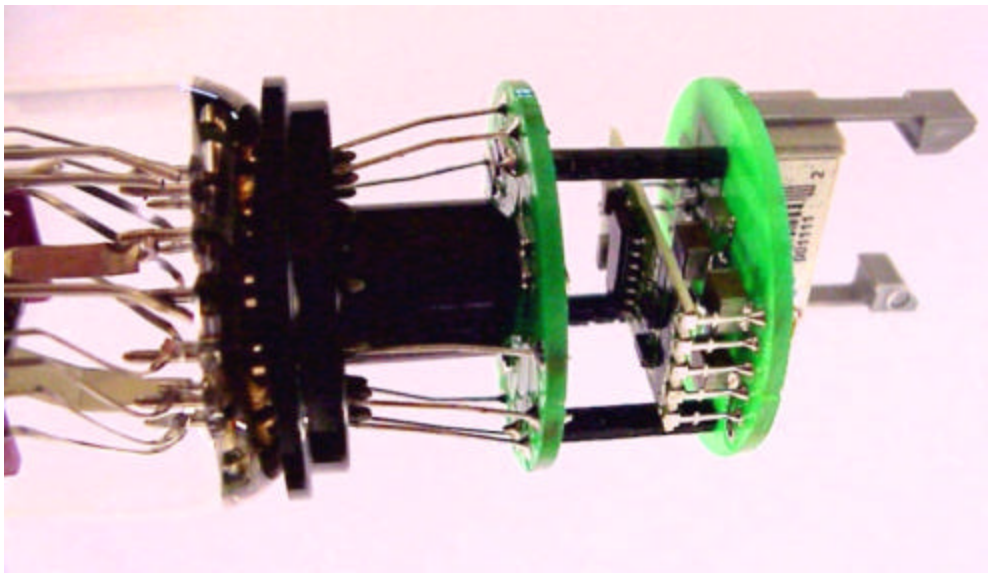

Figure 1: A Head Electronics connected to an XP3062 PMT. Each unit has a bar-coded serial number for identification and tracking. The units are connected to the Distribution Board via a 30 cm cable attached to a 10-pin 3M connector located at the external PCB.

The bias PCB

The PMT is biased using an active divider network whose equivalent resistance is 6.35 MΩ, including a 100 kΩ filtering resistor at the HV side of the chain. The active divider allows constant PMT gain even at relatively large background currents, as well as reduced power dissipation. The low power consumption implies a significant reduction in the cost of the HV power supply. In addition, the lower power dissipation of the active biasing chain translates into a lower operating temperature which improves the reliability. A comparison of performance between the active divider and a conventional passive scheme is shown in Fig 2.

The Driver PCB

The maximum PMT's anode current signal is 5 mA that is converted into a 2.5 V voltage pulse by the 500 Ω load resistance. The maximum signal at the driver's output is therefore 5 V. A differential input, balanced-output chip, MAX4147ESD, reads-out the single-ended current signal from the PMT, with a high rejection of the common-mode noise. In fact, the driver's differential input is used in combination with a symmetrical load resistor network to allow high rejection of common-mode noise. It has to be noted that, at low frequencies common-mode noise can not be effectively filtered by an RC network at the high-voltage end of the biasing network, due to the capacitance limitation of a HV capacitor. In Fig. 3 it is shown the input network, comprising two load resistors and two HV blocking capacitors symmetrically disposed onto the PCB layout, to reduce the common-mode noise.

The PMT current signal instead, enters in only one of the symmetrical branches at the driver's input and appears at the outputs with different levels and polarities. This is shown in Fig 3 where, by inspection, the indicated pulse shapes can be derived. In particular, it can be noted that the non-inverting pin at the input of the receiver chip remains at virtual ground, while the whole signal develops at the inverting input of that chip. The receiver chip is a MAX4145ESD and its gain was fixed to 1.45 which originates a positive going output of 3.6 V, within its linear range.

The differential output terminals of the driver are biased to a common-mode voltage of 1.36 V. This is necessary to better accommodate the PMT signal within the linear region of the driver chip, Fig 4. An overflow of 32 % in the maximum signal developed at the driver output is in this way ensured.

Twisted–pair lines are used for the signal transmission between the HE and the Distribution Board (DB) and between the DB and the Analog Board (AB), at the front-end electronics. The latter lines are much longer than the former and have specified 120 Ω characteristic impedance. The driver circuit therefore comprises two laser-trimmed 60 Ω resistors to terminate the line at both the receiving and sending end. Reflections are in this way avoided and the signal at the input of the receiver becomes identical to the one at the load resistor(s).

The MAX4145 chips drive twisted-pair cables which, after traversing the DB's located at the back of the camera, end with a differential line receiver MAX4145 at the AB. Two diodes and a series resistor, protect the driver chip against HV sparks. The HE can permanently withstand short circuits to ground at the output without damage. Power dissipation increases to 370 mW from its 270 mW at the HV-ON condition, during normal operation.

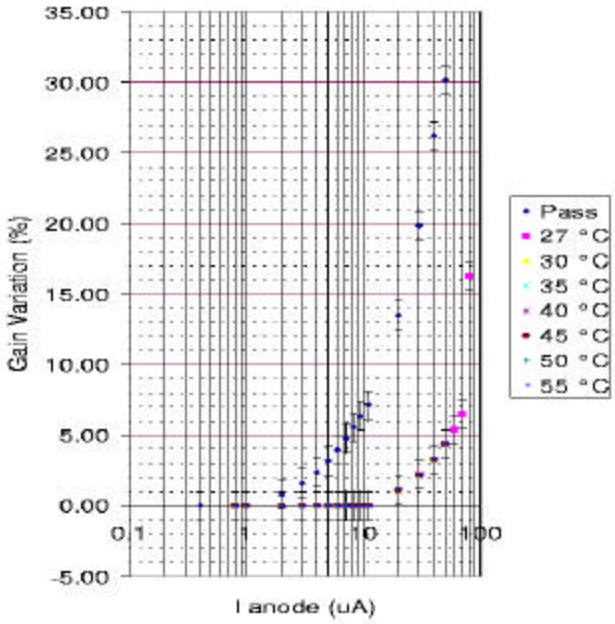

Figure 2: PMT gain variation for a passive bias network taking 270 µA and for an active one taking only 144 µA, at different temperatures. At 20 µA the passive network has a 14 % gain change while it is only < 2 % with the active network. The maximum current of interest is 6 µA when Vega or other similarly bright stars are in the field of view of a telescope.

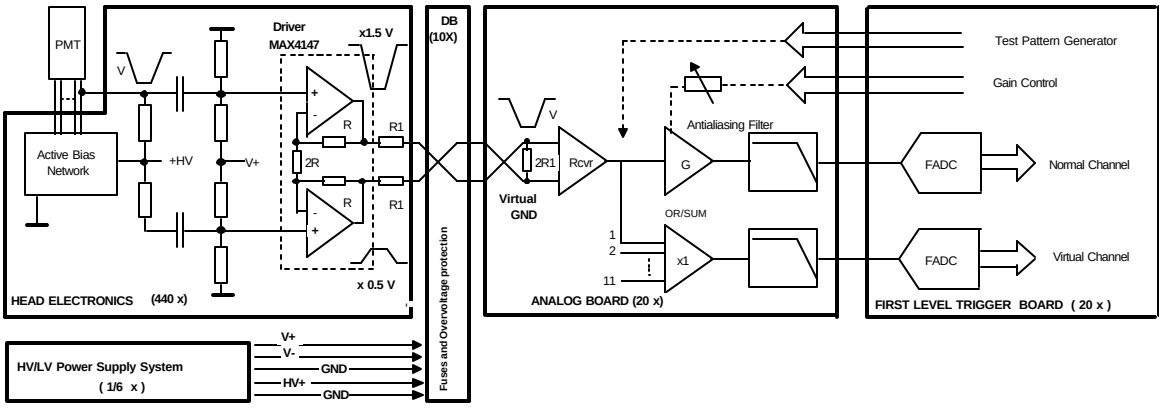

Figure 27: Block diagram of the Analog Signal Processor. The signal shapes are indicated. The symmetrical input circuitry reduces the common-mode noise, while the PMT signal is enhanced.

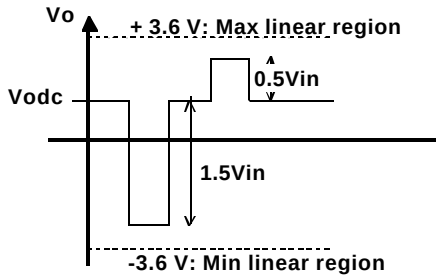

Fig 4: The asymmetric pulses at the driver's output require a DC level to ensure operation in the linear region.

Background light measurements:
During the Engineering Array phase of the Project, the two prototype telescopes were equipped with an optoelectronic system [17] that modulated the DC level at the output of every HE (Vodc of Fig 1.30), according to the intensity of the background light seen by the corresponding pixel. Records every 20 s or 30 s have been taken. Selected results are shown in Fig. 5 together with records taken by an alternative method based on the evaluation of the variance of the baseline fluctuations. That evaluation is performed by taking profit of the high processing power of new FPGA's incorporated in the FLT Board.

Taking periodical records of the average background light in every pixel is important to perform the following actions:

- to control the absolute pointing of the telescope pixels and its long-term stability by tracking bright blue stars.
- to evaluate the photocathode uniformity by analyzing the signal of stars transiting trough the telescope field of view.
- to evaluate the sky quality (presence of clouds, atmospheric attenuation, presence of light sources).

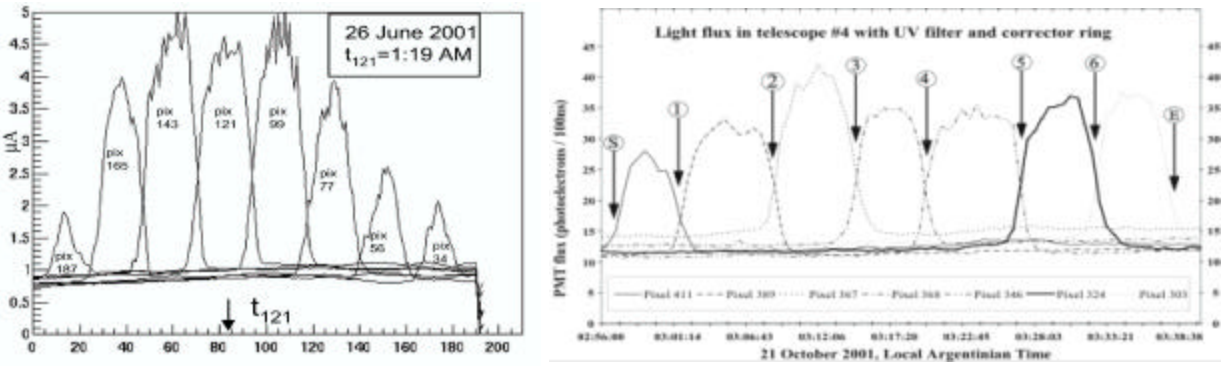

Fig. 5 (left): Signal of the bright star Vega crossing the FD Camera as seen by the optoelectronic based current monitor. **(Right):** Signal left by Elnath (vmag 1.64) as seen by evaluating the variance of the baseline fluctuation.

The anode current in μA corresponds, for a PMT gain of 50000, to 14.2 pe /100 nsμA. The time axis indicates units of 20 s. The pulse width at half maximum of a star signal was about 6 minutes. The pedestals of each pixel correspond to the dark sky light: 0.8 μA or 11 pe/100 ns.

The plots of Fig 5 show that the variance method has sufficient resolution to calculate the absolute pointing of the telescopes using bright stars. It was adopted for the final design.

Production of the Head Electronics

The HEs were produced by Intratec GmbH who has an associated production facility (Elbau) in Berlin. Intratec participated to the INFN call for tender for the fabrication of 12000 units and formulated the best offer. In addition the technical documentation about the technologies they use for the production left a very good impression to the Production Readiness Review committee.

The Head Electronics consists of two PCB's, one hybrid circuit for the driver, and three inter-board pins. They are shown in Fig 6.

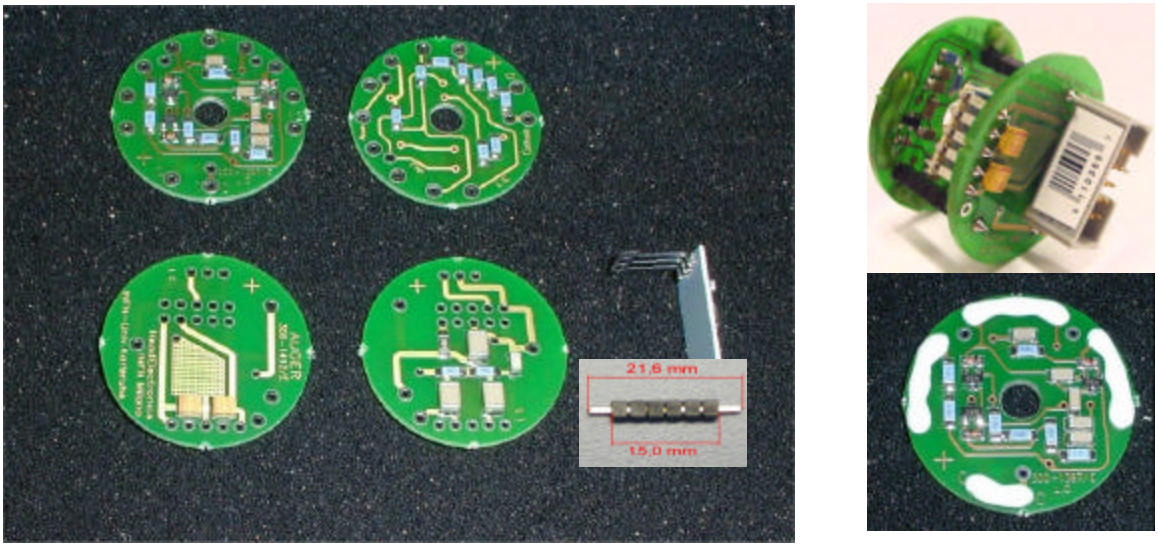

Fig 6: The Base PCB (upper side), the driver PCB (lower side), the hybrid driver circuit and the interboard pins. The soldering pads of the Base PCB are protected against oxidation by a Flex Mask, which is removed just before they are mounted onto the PMTs. The central hole serves to accommodate a plastic piece used to reinforce the mechanical strength of the PMT+HE assembly. At the upper-right corner: a finished HE unit.

The fabrication of the HE is performed in a clean room (class 100000) for assembly and testing operations. The hybrid circuit is made in a clear room class 10000. The only hand made operations are the mounting of the hybrid circuit and the 3M connector, and the soldering of the three inter-base pins. The soldering of all the surface mounted components is done using automatic machines.

Quality assurance:

Reliability of the HE's should be ensured taking into account that the life of the experiment is estimated to be about 20 years. The procedure consists on the optimization of the fabrication process in order to get a highly uniform product. On the other side, a severe thermal stressing cycle (burn-in) is performed on all fabricated units to accelerate the so-called "infant mortality". Pre and post burn-in tests are performed using a test set-up developed on purpose.

The whole production has been scheduled as four batches of about 3000 units each, made approximately every four months. The acceptance test consists on the verification of a series of parameters that are indicated in the following table:

HEAD ELECTRONICS SPECIFICATIONS

General, @ 25 °C	
Low voltage power supply	+6 V/ 13.5 mA +- 0.35 - 6 V/ 9.5 mA + - 0.32
HV supply current	144 μA@ 915 V +- 1.5 %
Total power dissipation	138 mW (+ HV power dissipation), typ 270 mW
Signal Driver:	
Input	Differential
Output	Balanced
Total Output Resistance	60 Ohm + 60 Ohm, 1 %
Signal Gain (over a 120 ohm load)	0.5 mV/μA (R_L=500 Ohm; Voltage Gain = 2)
Slew Rate	2000 V/μs min.
Max Signal Current	5 mA; (~2 mA over range allowed)
Bandwidth	100Hz-10Mhz
White noise density level	9 nV/ vHz max.
Common-mode rejection ratio (CMRR)	At least 28 dB 1kHz-100kHz
Short circuit conditions	Permanent, without damage.
Max power dissipation at short circuit	240 mW, plus HV power dissipation, typ 370 mW total.
V_oDC	1.36 V
PMT bias:	
Type of divider	Active
Divider current	144 μA@ 915 V
Gain change (max) as function of DC anode current	1.8 % @ 10 μA 2.3 % @ 24 μA 5 % @ 50 μA
Max operating voltage	1.5 kV

Acceptance tests: as said above, pre and a post burn-in tests are performed using a set-up designed on purpose in collaboration with the manufacturer, Fig 7.

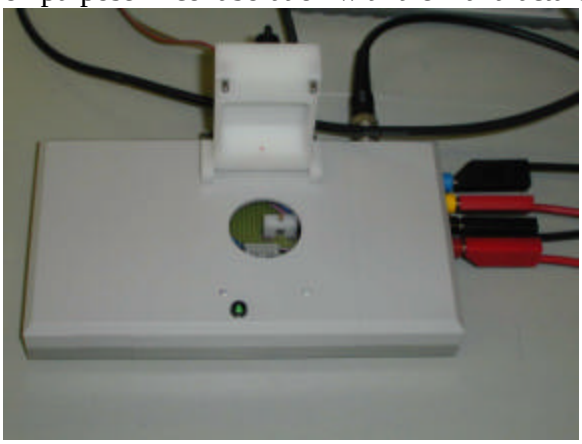

Fig. 7: The test set-up consists on a hardware unit under control of a LabView-based data acquisition system.

The first step is a visual inspection, to screen-out possible assembly and soldering errors. In the Base PCB the values of the resistive chain are also verified.

With the intervention of an operator, the apparatus performs a test consisting in the following steps:

a) DC test: with LV and HV applied, the following parameters are measured. A unit is rejected if a single parameter is outside the indicated boundaries:

- positive supply current I + : within 12 mA and 16 mA
- negative supply current I - : within 8 mA and 13 mA
- common-mode output voltage Vo: within 1.31 V and 1.40 V
- differential output voltage Vo_diff : within –25 mV to + 25 mV
- HV voltage monitor: within 3.73 V and 3.77 V (HV mean = 1500 V)
- HV current pre burn-in: within 1.175 V and 1.800 V (235 – 360) µA
- HV current post burn-in: within 1.175 V and 1.225 V (235 – 245) µA

b) Pulsed operation: a test pulse is injected trough the special Test pad. The output signal is verified using a receiver circuit and a digital oscilloscope that form part of the test system. All samples describing the pulse response are within ± 5 % of the average pulse shape of the lot.

d) Burn-in: A lot is subject to burn in, lasting 40 h, consisting in 20 thermal cycles of 2 h each from 5 °C to 60 °C. LV and HV (1500 V) are applied during the whole burn-in test.
e) Repeat all above after burn-in:

The uniformity of the lot is evaluated once again. Units not satisfying the above mentioned margins are rejected.

Selected results of the first three batches (about 9000 units)

A few results of the first three batches are summarized below. The unexpected behavior of HV_Imon before burn-in and the explanation of the mechanism that originated it, is addressed below.

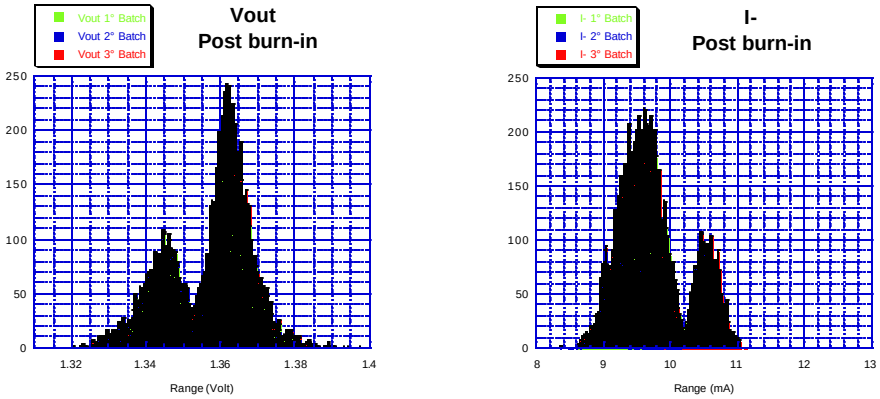

Fig 8: A correlation between the negative power supply current and the output voltage is evident. This is due to the drop of voltage across the 50 Ω resistor used in series with the positive supply, as an RC filter.

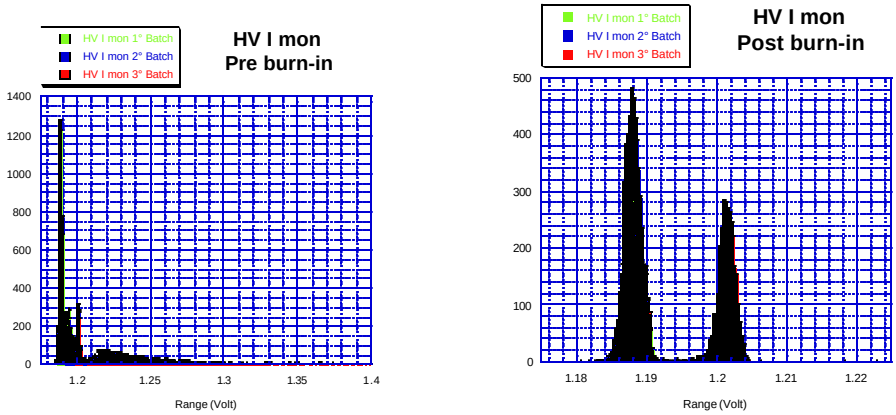

Fig 9: An unexpected long tail towards higher values can be observed in the parameter HV_Imon. The reason was the conductivity in the FlexMask due to the presence of solvents that evaporated during burn-in as it is shown in the right plot.

PRE BURN-IN	Vout [V]	Vdiff [mV]	HV mon [V]	HV Imon [V]	I+ [mA]	I- [mA]
Mean	1.356	-0.4692	3.751	1.220	13.78	10.00
Max	1.402	14.31	3.758	1.740	15.12	11.20
Min	1.319	-18.90	3.732	1.181	12.42	8.360
St.dev	0.0116	3.050	0.002926	0.0611	0.510	0.520
St.dev %	0.85	--	0.078	5.00	3.70	5.21

POST BURN-IN	Vout [V]	Vdiff [mV]	HV mon [V]	HV I mon [V]	I+ [mA]	I- [mA]
Mean	1.3570	-0.544	3.750	1.1930	13.74	9.747
Max	1.3980	14.19	3.757	1.223	15.05	11.13
Min	1.320	-15.17	3.730	1.175	12.41	8.353
St.dev	0.0112	3.107	0.003186	0.006584	0.4925	0.5143
St.dev%	0.82	--	0.085	0.55	3.60	5.28

Fig 10: A comparison of results obtained before and after burn-in. To be noted the improvement by a factor 10 of the standard deviation of HV_Imon, after burn-in.

Concluding remarks

The very high uniformity of the almost 9000 HE units produced gives a very good indication that what we have in hands is highly reliable object. The percentage of rejected units is 1.45 % only.
The burn-in thermal stress made it possible to reduce by a factor 10 the dispersion of HV_Imon.

1.2.1.2 Distribution Board

General
The AB and the HE are interfaced via the Distribution Board (DB) and related cabling. The FD signal from each pixel is conveyed to the AB in differential mode. HV for the PMT biasing and LV for the HE pass trough the DB that provides also protection against surges at the LV and to accidental reverse polarity in the LV and HV supplies.

The modularity is such that each DB serves four vertical pixel half-columns. An upper and a lower board are the minimum number required to read one complete column. Actually two DB's serve 88 channels which correspond to four Front-End Boards (i.e. AB+FLT) for a total of 88 channels.

The boards are not symmetrical and serve all four columns from one side only.

Cabling
AB to DB

A 26 twisted-pairs cable connects the AB to the DB. At the AB the cable plugs into the rear of the analog bus via a 64 pin connector (e.g. 3M 6964), using pin 1 to 26 and rows A and C. This cable is split in two and is connected to the upper and lower DB's using two separate 30 pin connectors, of which pins 1 to 13 of both rows are used.

HE to DB

The connection between the DB and the HE is done via a single cable comprising 7 wires organized in three twisted pairs and one single conductor for the HV:

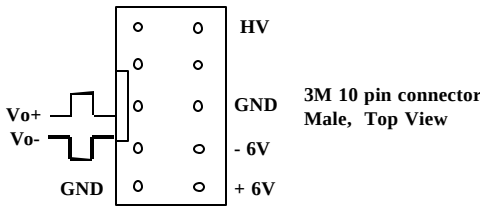

Fig.11: The male connectors at the DB are implemented with 3M type 2x5 pins 2.54 mm pitch connectors. At the HE side, the same connector used at the DB has been adopted for the Driver PCB that is the external board of the HE.

Signal distribution
Pixel signals travel via twisted pairs through the cables and as balanced lines in the DB. The nominal impedance is 120 Ohm. Total lengths are reasonably equalized and a 120 Ohm terminating resistor has been included at the input of the receiving stage and as two 60 Ohm laser-trimmed resistors are included at the driver's output as well.

Protection
0.7 Ohm fuses are used for each LV line of the HE. They are mounted onto the DB. A 1 W Zener diode at each LV leg per DB absorbs over-voltage surges. In addition the diode short circuits the power supply in case of accidental reverse-polarity connection. A HV diode provides protection against reverse-polarity in the HVPS.

Grounding
Each DB has four separate ground planes, one per column, each one associated with the AB reading that column. All four planes are connected together at one point as shown in Figure . Separate ground planes ensure minimum cross-talk and no ground loops.

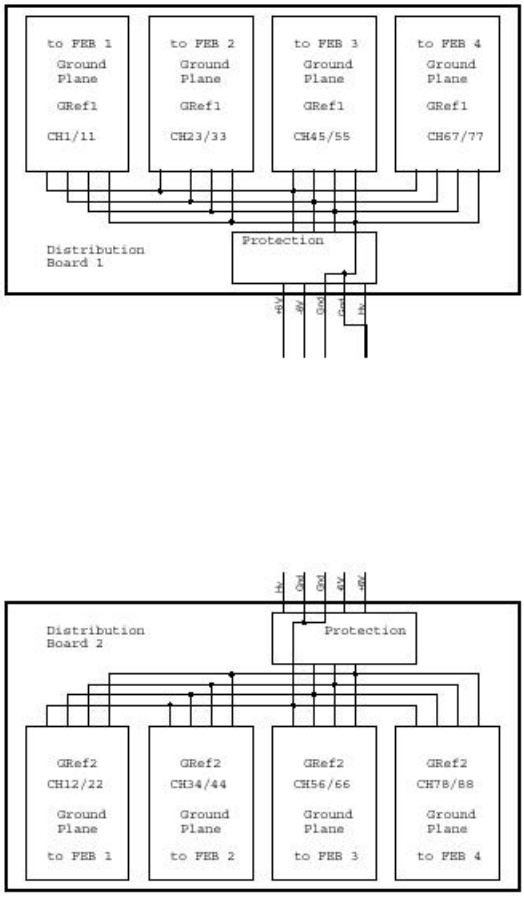

Figure 12: Each group of 11 channels has an associated ground plane. All four planes join at one single strip at the board.

1.2.1.3 Analog Board (AB)

Functional Overview
The Analog Board (AB) is located in the front-end sub-rack. It is connected via twisted pair cables to the Distribution Board and from there to the Head Electronics. The Analog Board processes these

signals as described in the following, and presents them to the ADC located in the First-Level Trigger Board (FLT).

The electronics blocks in the Analog Board [18,19] must perform the following:

- receive the signals transmitted by the Head Electronics via twisted-pair cables, performing a differential-to-single-ended conversion;
- adjust the channel gain to compensate for the gain spread of the PMT's;
- adapt the dynamic range of the PMT signals to the input dynamic range of the ADC;
- provide an adequate signal filtering to prevent aliasing;
- generate test pulses to check the functionality of the electronic chain downstream the FEB and to perform a gain equalization;
- generate internal test patterns to test SLT functionality;
- ensure an adequate reliability for the operation on the site of the Auger Observatory.

Requirements

The requirements for the Analog Board are summarized below.

Mechanical requirements

I) Number of channels per board: 22 (+2 Virtual Channels, see below)
II) Board size: 3 U high, 220 mm deep

Operational requirements

I) Operating temperature: 25 °C ± 3 °C
II) Power dissipation: < 350 mW per channel

Dynamic range

The system has been designed to handle the PMT signals with a 15 bit dynamic range. The minimum signal corresponds to 3 photoelectrons in a 100 ns time slice. It occupies 6 LSBs making a 0.5 pe/100 ns/ADC count. Considering a PMT gain of $5x10^4$, the amplitude of the PMT anode signals would vary between 240 nA and 7.8 mA.

Simulations of EAS detection at the southern site [20] indicate that a 15-bit or even 14-bit signal dynamic range (our specification is 15 bit) might be acceptable, with a maximum signal amplitude between 49000 and 98000 pe/100 ns. With a PMT gain of 50000, the Head Electronics is within its linear range even with a 62500 pe/100ns signal. As the HE accepts in addition an over range of 32 % , this raises the highest signal to 82500 pe/100ns, quite close to the target of 98000pe/100ns. If this target value is anyway required, it can be reached without compromising the system linearity only by

reducing the PMT gain to 32000, or to 42000 taking profit of the available over range. The latter is not advisable as it leaves no linear range margin. The requirements on the signal dynamic range therefore require a compression scheme in order to work with a 12 bit ADC. We adopted the "virtual channel" approach due to its simplicity and reliable behavior.

Noise performance

The analog processor has to preserve the shape of the signals (complying with the ADC anti-aliasing requirements), for timing and amplitude measurements, without introducing sizeable electronic noise.

We define an upper limit for the total noise (i.e. electronic plus sky noise) comparing it to the sky noise. The total noise was specified to be not higher that 10 % the sky background noise. Referring the noise as a current generator i_n in parallel with the PMT anode current signal, and by evaluating the power spectral density $\frac{d\overline{i_n^2}}{df}$ of this generator, we calculate the sky noise spectral density assuming a dark sky noise of 11 pe/100 ns as:

$$\sqrt{\frac{\mathrm{d}\overline{\mathrm{i}_{\mathrm{sky}}^2}}{\mathrm{df}}} = 1.2 \cdot \sqrt{2\mathrm{qI}_{\mathrm{sky}}} \cdot \mathrm{G}_{\mathrm{pmt}} \cong 68 \frac{\mathrm{pA}}{\sqrt{\mathrm{Hz}}}$$

considering an average cathode background current I_{sky} = 11.2 pA, and a conservative estimate of $3x10^4$ for the PMT gain.

The factor 1.2 takes into account the excess noise due to the PMT electron multiplier.

The total noise should be at most a 10 % higher than sky's noise. This is reached with higher PMT gain (e.g. 40000), but this reduces the dynamic range unless the gain of the virtual channel is reduced from its nominal value relative to the normal channel of 1/33.

During the Engineering Array phase of the experiment, data have been taken with a gain

of about 44000 bringing the total noise to only 8 % higher than the sky's noise.

Anti-aliasing filter specifications

According to the analysis carried out in [21], the order of the filter and its cut-off frequency was chosen in order to minimize the residual error in the signal reconstruction from the samples taken by the ADC. As a design goal, the error has to be less than 5%.

Calibration requirements

Provision has been taken to inject a signal at the inputs of an arbitrary, remotely selectable set of channels. The signal amplitude is also remotely adjustable.

Circuit implementation

Signal receiver

The differential-to-single-ended conversion is performed by a MAX4145 differential line receiver. Its noise contribution dominates the electronic noise. In fact it is 14 nV/vHz which is summed quadratically to the driver's noise of 8 nV/vHz and 2.8nV/sqrt Hz of the load resistors giving a total electronic noise of 16.4 nV/vHz. Nevertheless the total noise is still within 10 % above the sky noise. The receiver enable/disable capability allows us to perform channel masking for trigger pattern simulations.

Anti-aliasing filter

The analog channel outputs are connected to ADCs which sample the signals at 10 MHz. To ensure that the samples can accurately describe the signal, the bandwidth is limited to the Nyquist frequency (5 MHz). On the other hand, every practical filter limits the bandwidth only partially. In ref. [22] the residual error in the reconstruction of the amplitude from the samples is studied as a function of the filter order and of its cut-off frequency. We determined that that a 4th order filter with a 4.1 MHz cut-off frequency is adequate, considering the overall resolution requirements of the fluorescence detector. The frequency response of such a filter is shown in Fig.13. It comprises a third-order Bessel filter followed by an RC low-pass filter put just before the ADC.

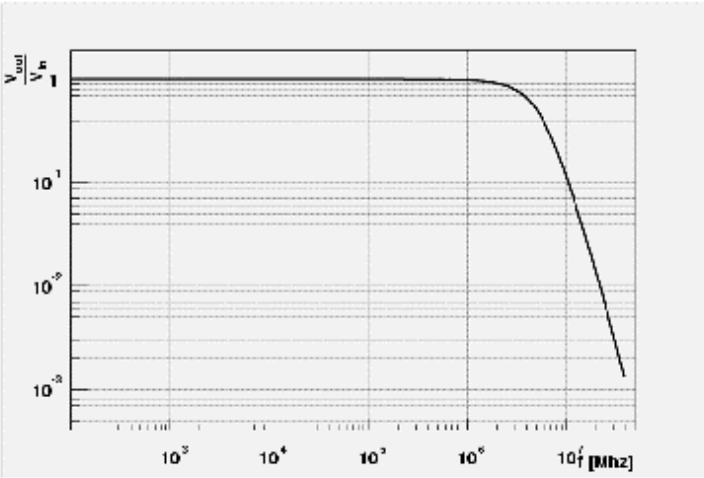

Figure 13: Frequency response of the anti-aliasing filter.

Dynamic range adapter

To readout the 15-bit dynamic range signal with 12 bit ADC's, a dual gain system has been implemented. Different solutions were discussed in ref. [23]. Two of them, not requiring custom chip

developments, have been implemented in the first version of the prototype board: the analog compressor and the virtual channel. The latter has been chosen because of its better characteristics in terms of power dissipation, circuit simplicity, linearity and noise performances.

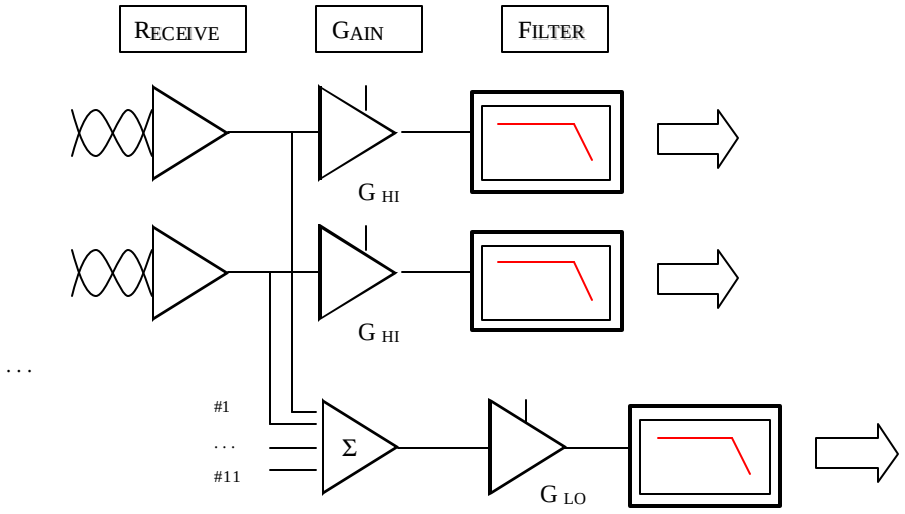

Figure 14: Block Diagram of the Analog Channel with the Virtual Channel for dynamic range adapting.

Virtual channel:

This dynamic-range compressing scheme exploits the fact that the fluorescence detector signal appears sequentially in neighboring pixels. Large amplitude pulses (above 3000 p.e./100 ns) will occupy, at the same 100 ns time slot, only one of 11 non-adjacent channels.

As shown in Fig.14, this compressing scheme uses simple 12 bit linear channels with a high-amplification in the signal path of the normal-channel to the ADC. At the same time, signals from 11 non-adjacent pixels, will be added in a summation (or OR) channel (Virtual Channel) and sent to an ADC. The minimum signal at the high-gain Channel is 3 p.e. / 100 ns (6 LSB), so it saturates at about 2000 p.e./ 100 ns. The virtual channel is analyzed when any one of the group of 11 saturates. Compared to a normal channel, the noise at the VC will be $\sqrt{11} = 3.3$ times higher, but is used with signals higher by a factor 1000 the smallest signal only. Two plots illustrating the virtual channel operation are shown, in linear and logarithmic scales, in Fig 15.

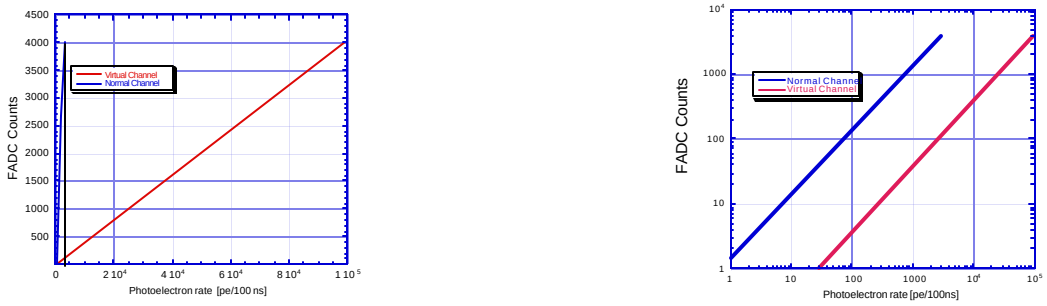

Fig15: The normal (blue) and virtual (red) channel transfer characteristics in linear and logarithmic scales.

Gain adjustment

A gain control capability is necessary to compensate for the gain spread of the PMT's. On the Analog Board this is accomplished by controlling the value of digitally programmable resistors at the gain stage. The system is able to accommodate a factor 1.4 variation of the PMT gain above and below its nominal value.

Test Pattern Generation

This test mode allows evaluation of Second Level Trigger (SLT) functionality without requiring external hardware. A set of analog switches is used to inject a pulse of selectable amplitude and duration into the reference pin of the receiver. In this way, trigger patterns are generated and can be recognized by the SLT.

Production of the Analog Board:

The Analog Board, Fig 16, has been produced by an Italian firm, Dertel Srl, selected by INFN after a call for tender procedure.

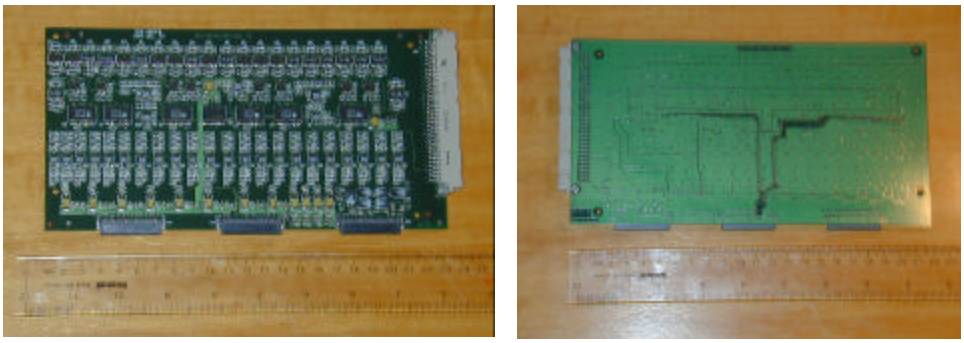

Fig 16: Front and reverse sides of the Analog Board.

Quality assurance:

All 480 Analog Boards requested for the 24 telescopes have been already produced, tested and shipped to the FZK group who is in charge of integrating them with the First Level Trigger board, forming the Front-End Board.

The acceptance test has as main objectives the following:

1. Check that all channels are alive
   - Check that Gain programming works correctly
   - Check Test Pulse injection
   - Check for (relatively) noisy channels.

After soldering phase has been completed, current consumption is checked.

2. Boards undergo an ESS -Burn in cycle with applied voltages [Clark and Dye, GAP 2002-002].

3. Boards undergo an automated test at the manufacturer's plant, which consists of three steps:
   - First level control: Check that all channels are alive.
   - Second level control: Check that Digital Potentiometers have been correctly programmed.
   - Third level control: Acquire all pulse shapes by oscilloscope and save them to disk.

4. Data is ready to be analyzed off line.

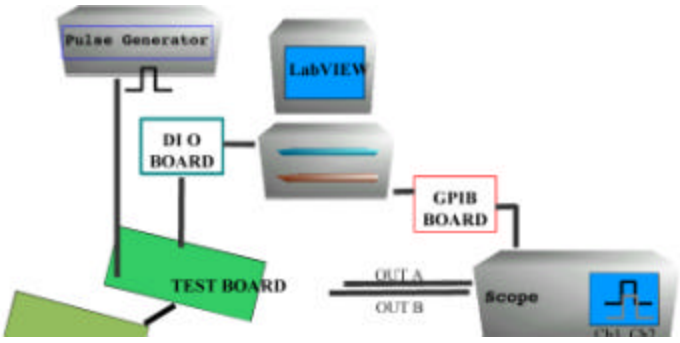

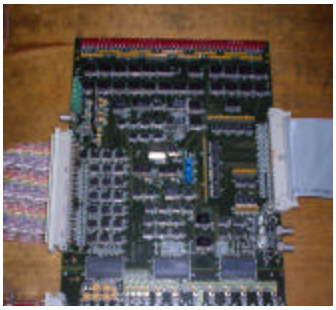

Fig 17: The test setup consists of various instruments interconnected via GPIB bus, under control of LabView. At the upper right corner, an AB is being subjected to the acceptance test.

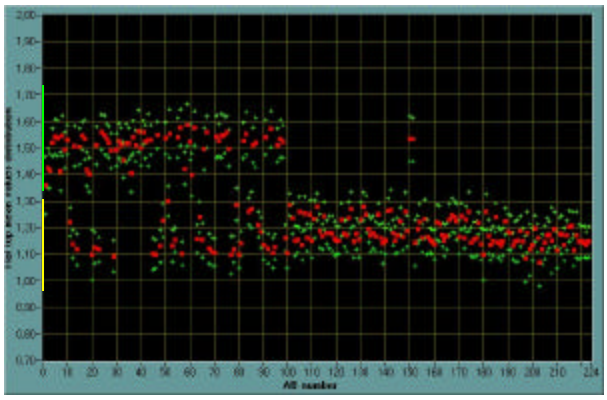

Fig 18: Two different distributions are visible which are corresponding to two different digital potentiometers AD8403-1k production lots. However, the difference can be compensated by appropriate gain programming.

Concluding remarks: An acceptance test system for the Analog Board has been designed and installed at the manufacturer's plant. The tests were performed by the manufacturer who sent the data to Torino for a careful analysis. Two series of boards were defined according to the batch of digital potentiometers used in the production. In either batch, the uniformity of parameters is very satisfactory.

1.2.1.4 First Level Trigger (FLT)

Functionality of the FLT

The First Level Trigger (FLT) is the heart of the digital front-end electronics. Its main tasks are:

- digitize continuously the signals from the Analog Board with 10 MHz,
- store 64 times 100 µs of digitized raw data in memory for later readout,
- discriminate efficiently for each channel the fluorescence light above a certain threshold from night sky fluctuations and generate a pixel trigger,
- measure the pixel trigger rate for each channel,
- compensate changing background light intensities through automatic control of the pixel threshold to achieve constant pixel trigger rates and prevent increasing rates of random coincidences,
- transfer the pixel status and multiplicity on demand to the Second Level Trigger (SLT),
- support access to raw data memory and internal registers through a PBUS+ interface,
- calculate statistical data (Σx, Σx^2) of up to 65 535 ADC values per channel, and
- provide a digital interface to the Analog Board in order to generate test pulses and to set the gain of the analog amplifier stages.

The organization of the frond-end electronics follows the geometrical pixel arrangement in 22 rows by 20 columns. The 440 PMT signals are processed by 20 FLT boards (one board per column) housed in a commercial 19" sub-rack with 22 input channels per board.

To allow concurrent and independent development by Italian and German groups, the analog and digital part of the front-end electronics are separates into two boards (AB and FLT), which are adjacent to each other and connected through three 50-pin connectors as shown in figure 28. A detailed specification of the interface definition can be found at [24].

All functions of the FLT are implemented in FPGA logic for high flexibility, cost-effectiveness and ease of operation. The large number of channels as well as the high connectivity made it indispensable to use 5 FPGA chips. The 22 channels (plus 2 virtual channels) are shared between 4 'slave FPGAs' (Altera EP1K50FC256-3) -- each handling 6 input channels as shown in Figure 28. More general functions of the board (like the communication with the PC and the SLT or the interface to the AB) are implemented into a separate 'controller FPGA' (Altera EP1K100FC256-3). This assignment of the functions to 5 FPGA is the cheapest solution and still leaves resources for future add-on functions. Despite the more challenging soldering technique we assemble FPGAs in ball-grid-array (BGA) package as this package type is only one third in price compared with regular type.

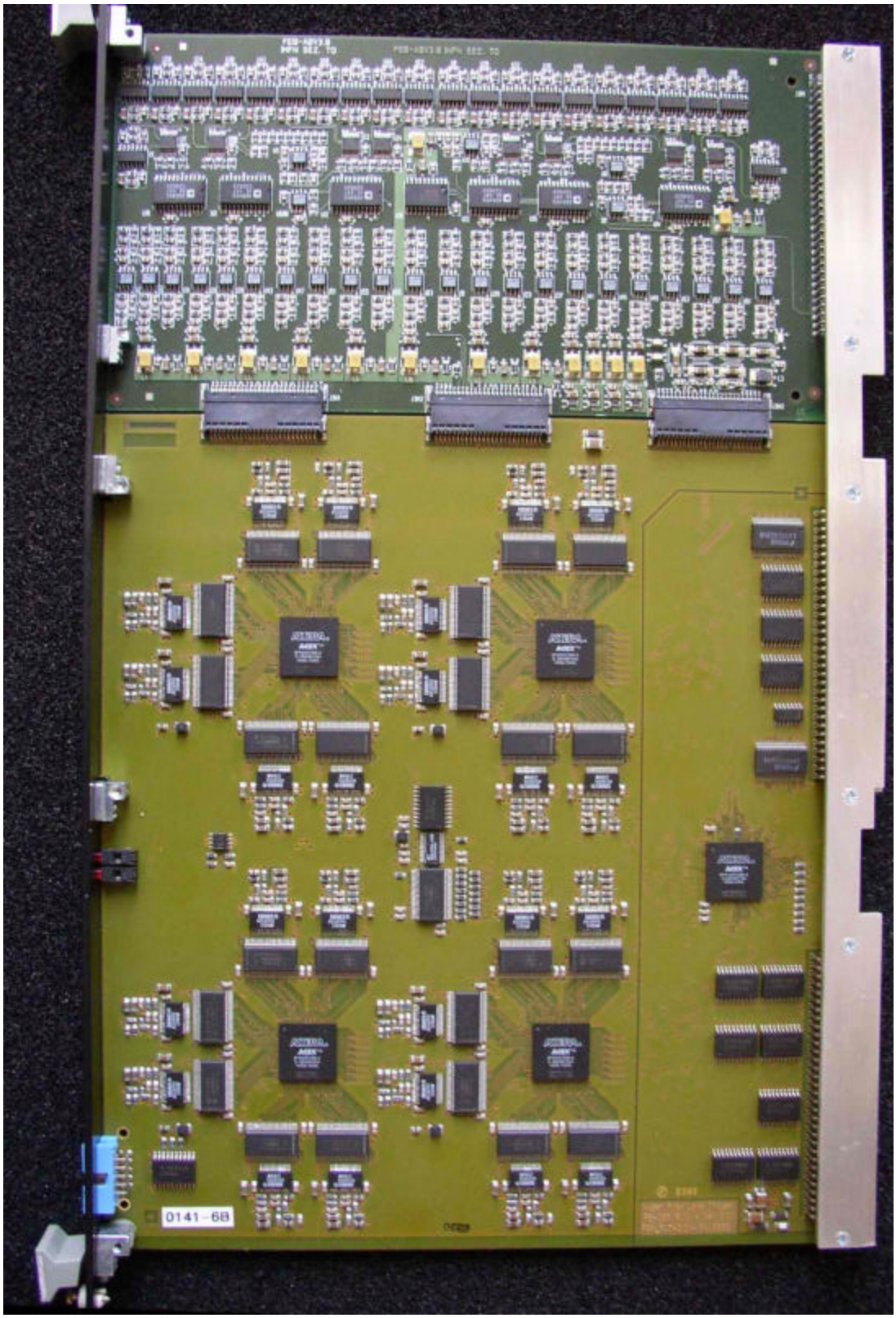

Figure 28: Photo of the First Level Trigger (FLT) (bottom) and the Analog Board (AB) (top). A common front panel and an aluminum stiffener bar combine both boards to a rigid front-end module.

Digitalization and Memory Management

Optimal measurements of the shower profile demand a 10 MHz sampling of the PMT signal. Therefore, a 12-bit ADC (Ti/Burr Brown ADS 804) continuously digitizes the analog signals every 100 ns. Together with the 4-bit status for ADC out-of-range, the threshold changed flag, the pixel trigger state and the pixel status this information is stored as 16-bit word in conventional 64K x 16 bit SRAM's. The address space of each RAM is divided into 64 pages of 1024 words each as shown in figure 29.

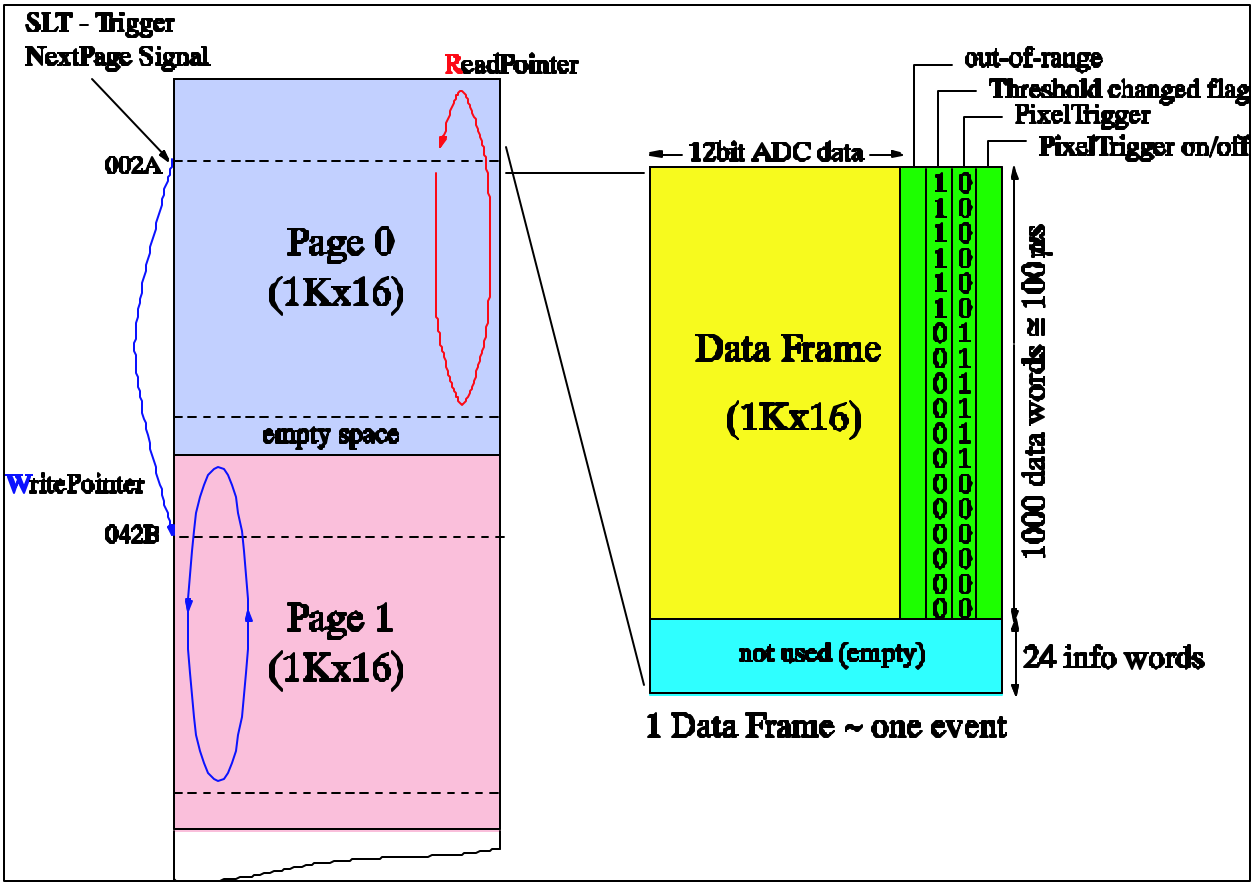

Figure 29: Memory architecture and data format of the FLT.

As long as there is no trigger generated by the SLT each page works as a circular buffer memory to hold the ADC values of the last 100 µs. In case the SLT detects a track, all boards synchronously switch to the same new page address provided by the SLT. By utilizing both slopes of the 10 MHz clock the FPGA can initiate read and write operations and emulate an expensive dual-port memory controller. In this way the system can continue to write into the new circular buffer without dead time while the event data is readout under PC control from any other memory page.

Pixel Trigger

Another task of the slave FPGA is to build the pixel trigger for each of the associated 6 channels. ADC values are averaged by calculating the moving sum of the last N samples as shown in figure 30. The theoretical possible improvement of the signal-to-noise ratio for this most simple digital filter

by a factor of √N is not fully achieved as adjacent ADC values are not statistical independent due to the anti-aliasing filter [25]. The default value for N is 10, but it can be set in the range 5 <= N <=16.

To simplify the logic only the lower 10 ADC- bits are considered in the summation. Over-flow and underflow are handled by replacing the 10-bit value at the summation stage with 3FF or 0, respectively.

A pixel is marked as triggered, whenever the moving sum exceeds an adjustable threshold – a 14-bit value unique to each channel. When the moving sum falls below the threshold a retriggerable mono-flop extends the pixel trigger for a programmable time of 5...30 µs. This extended time is necessary to achieve an overlap coincidence between 5 adjacent pixels.

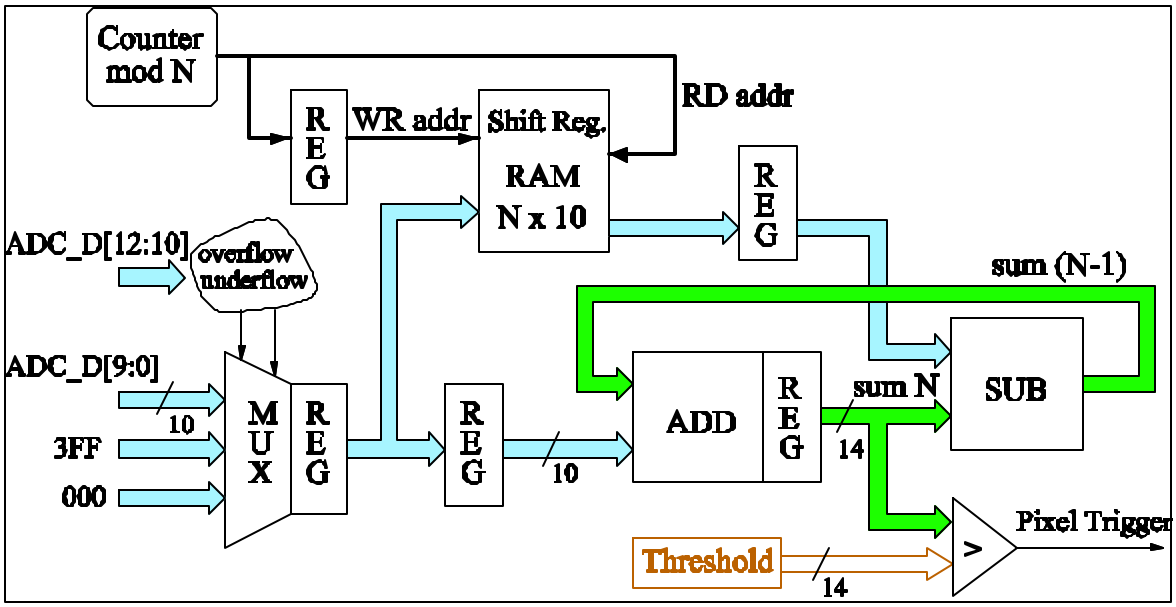

Figure 30: Calculation of moving average of N data words to improve the S/N-ratio.

Hit Rate Measurement

The rate of pixel triggers (or hit rate) is measured in parallel by 15-bit counters for each channel in the control FPGA. Possible measuring intervals are 1, 2, 4, 8, 16, or 32 s long and synchronous to the 1 pps signal from the GPS-clock. The counter values are normalized at the end of each measuring period to represent the rate in Hz and then stored in internal 10-bit registers for readout by the MirrorPC.

Threshold Regulation

The measured hit rate also serves as input variable for the adjustment of the threshold according to figure Figure 31. Six internal 10-bit FPGA registers hold regulation limits L1...L6 to define 7 margins. The latest hit rate is compared with these regulation limits sequentially for all enabled channels. Depending on the result of the comparison the control FPGA will then cause the slave FPGA to increase or decrease the threshold of up to maximal 15 ADC units. The previous and the actual threshold are held in internal 14-bit registers and are accessible at any time by the PC. The time of threshold change is included in the raw data as 'threshold-changed' bit (see figure 29).

The pixel trigger generation and the adjustment of the threshold can be disabled to deal with defective and/or noisy PMTs and re-enabled separately for each channel from the MirrorPC.

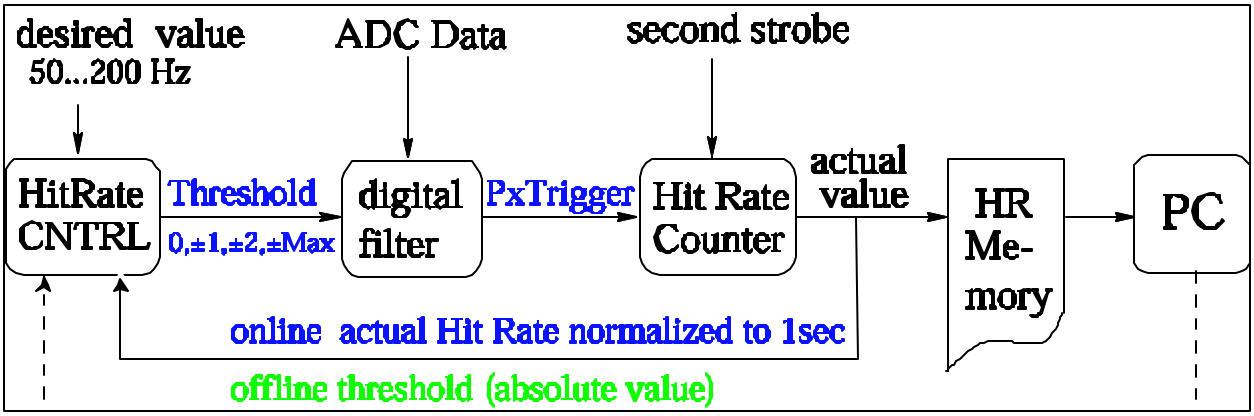

Figure 31: Control loop for regulation of hit rate by FPGA (online) and by PC (offline).

Calculation of statistical properties of the ADC data

Measurements with the EA prototype proofed that the DC brightness of the sky is an important experiment parameter which can be derived from the variance of the ADC data. Thus the slave FPGA calculates periodically for each channel the sum (Σx) and the quadratic sum (Σx^2) of up to 65 535 successive ADC values (equivalent to 6.5 ms) following the scheme of figure 32. A multiplexer selects the ADC date of one out of 6 channels and an 8-bit (plus sign) arithmetic unit subtracts the programmable offset 'ZMean'. ADC values with a distance of more than 255 LSB from 'ZMean' are regarded as shower signals and discarded from the calculation. For all other values we add up values x_i = (ADC – Zmean) and their squares. The square x_i^2 is calculated using a memory look-up table (LUT). When 'NSample' (e.g. 65 535) ADC data are analyzed the sum of all x_i and all x_i^2 is stored in intermediate registers per ADC and the algorithm continues with the subsequent ADC channel. Readout of (Σx, Σx^2) pairs guarantees the correct calculation of mean and variance by the MirrorPC.

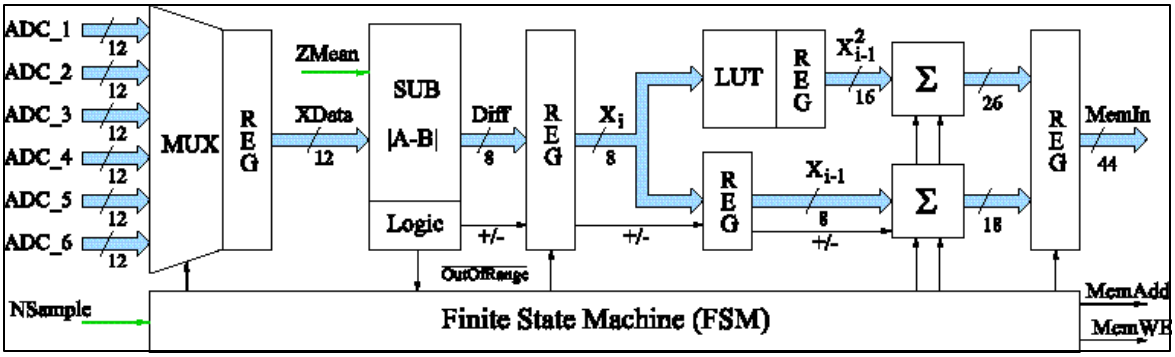

Figure 32: Scheme for mean and variance calculation as implemented in each slave FPGA.

Backplane busses and internal bus

The front-end boards are housed in standard 19” wide sub-racks of 9U height. They are interconnected via connectors P0 to the analog backplane on the top and via connector P1, P2 to a digital VME-like backplanes in the middle and the bottom of the sub-rack (see figure xx).

The analog backplane holds for each slot a VG-Connector to connect the PMT signals through twisted pair cables from the distribution boards. It also supplies 2 analog voltages (+5 V, -5 V) along current rail and distributes the DC signal for the test pulser amplitude. Separate layers for the analog ground (AGnd) and earth reduces the risk of EMC problems.

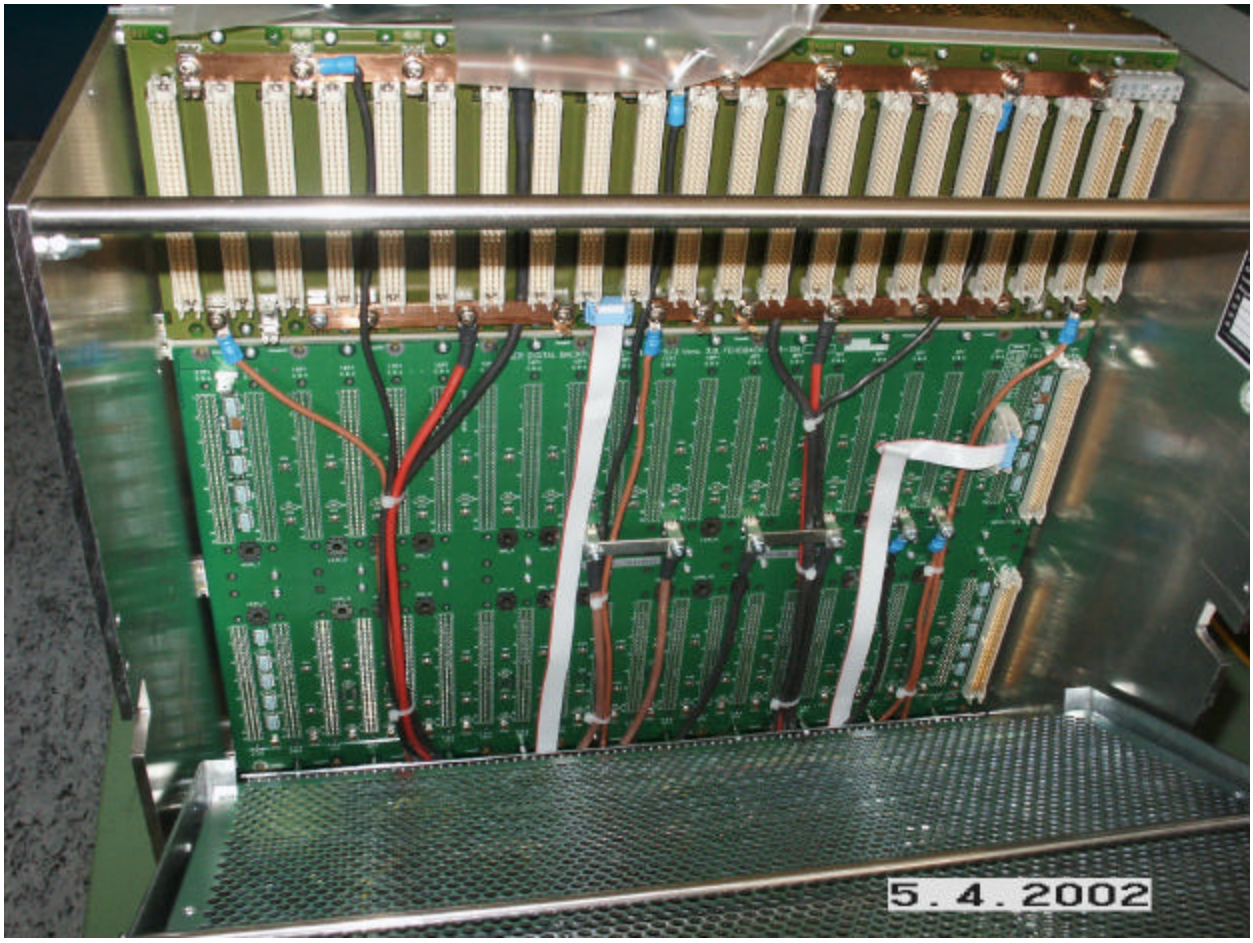

Figure 33: Photo of the analog backplane (top) and digital backplane (bottom) viewed with the power supply tilted 60 °.

The digital backplane is produced by ELMA/TreNew according to our specifications [26]. The 6 layer board has a structure and pin-out similar to standard VME J1-type backplanes. It builds up the 4 digital bus systems shown in figure 34:

- The Readout Bus transfers data from the FLT and SLT to the PC or vice-versa. It is based on the VME bus as physical layer, but uses a simpler bus protocol named PBUS+ developed for the KASCADE experiment. The protocol [27] assumes multiplexed address and data lines and provides an asynchronous handshake mechanism for proper synchronization of a single master (the MirrorPC) and multiple slave (the FLT and SLT) modules. In addition, an interrupt mechanism (with one interrupt level) is implemented to inform the PC on event triggers or error conditions.

- The Pixel Trigger Bus transfers pixel trigger data from the FLT to the SLT. Every 100 ns the SLT addresses two adjacent FLT boards via 5 select lines and requests the pixel trigger data (44 bits plus 2 parity bits). The transfer is synchronous with the central 10 MHz clock.
- The Test & Control Bus distributes GPS derived clock signals (10 MHz and 1 Second-Strobe (1 pps)), a test pulse signal (see chapter 1.2.1.10), and signals to configure the FPGAs. In addition, the bus drives control lines like Inhibit (Inh) and Reset.
- 6 daisy-chain lines forward the multiplicity from the FLT to the SLT.

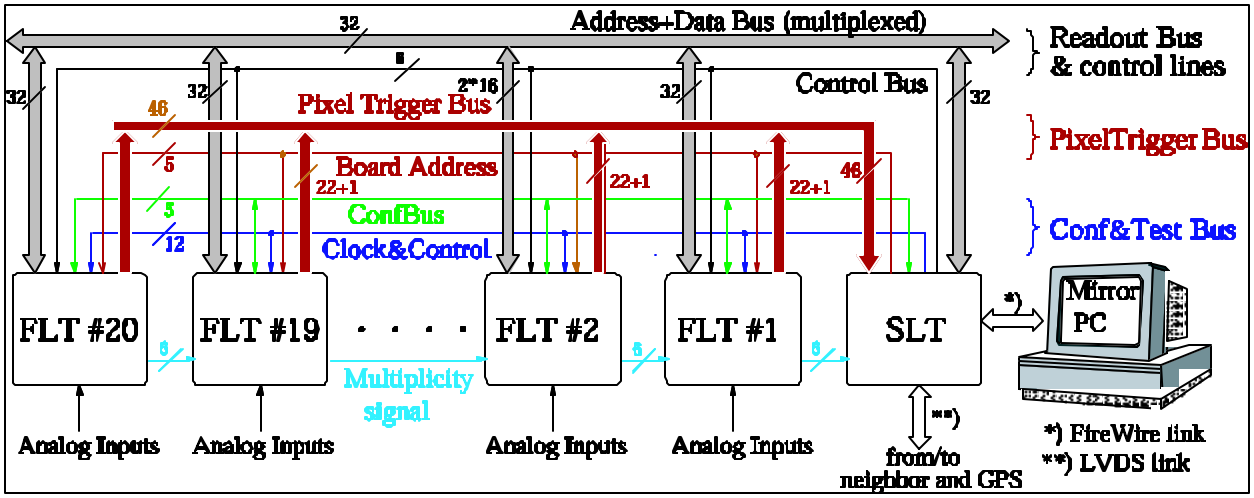

Figure 34: Interconnection of FLT and SLT via busses on digital backplane.

The controller FPGA of FLT and SLT listen continuously to the traffic on the readout and data bus. A coding on the digital backplane allocates an ID from 1...20 for each FLT depending on the geometric slot position. If the PC addresses the board by its associated ID, the card will respond to the demanded action.

Most commands access only the internal registers of the controller FPGA. However, commands to readout the ADC data or the actual threshold level require access to a slave FPGA via internal busses. The readout load is dominated by the huge amount of ADC data. To increase the readout speed 2 adjacent ADC words (each 16 bits) are readout in parallel per cycle. The design provides two 16-bit wide data busses for inter-FPGA communication (see figure 35). These busses are not multiplexed and operate synchronously. Latest measurements showed a data transfer rate of 2.6 Mbyte /s on the PBUS+ and the FireWire interface to the MirrorPC at block sizes typical for shower events.

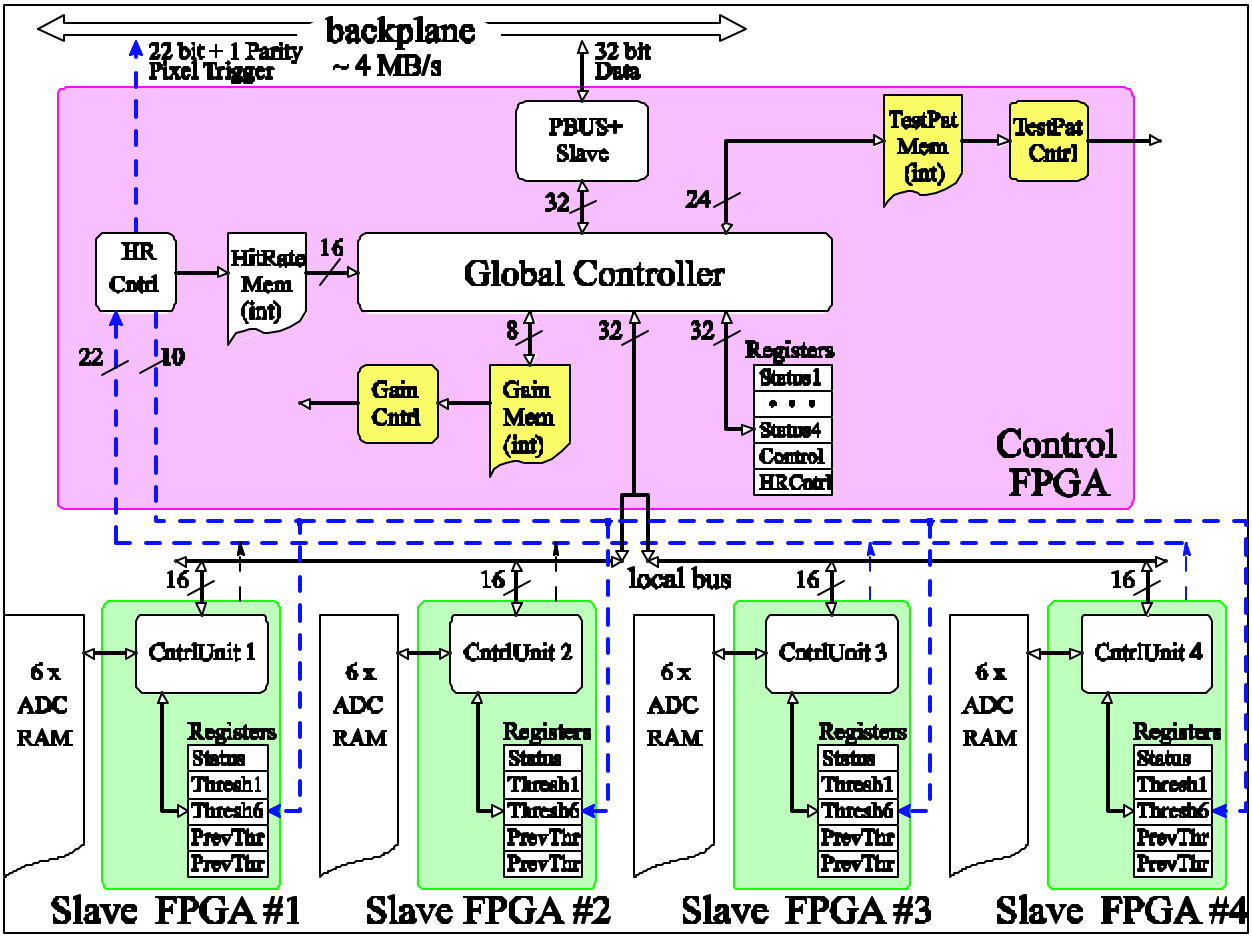

Figure 35: Structure of FLT: A local bus interconnects 4 slave FPGAs with the controller FPGA.

Inhibit Signal

Control lines from the GPS clock to each SLT can start and stop the data taking for all telescopes simultaneously. The SLT forwards an inhibit-signal (Inh) to starts and stops the measurement for all pixels simultaneously. If the signal is present, no ADC data is stored in the buffer and pixel memory, but hit rate measurement, threshold adjustment and access by the PC is left unaffected.

Experience with the FD prototype proofed that disabling the ADC clock signals does not reduce the power consumption. Therefore, we have not implemented a standby mode to be applied during idle times.

Interface to Analog Board: Gain adjustment and Test pulser control

Instead of using individual HV channels for each PMT, groups of 44 PMTs will be connected in parallel to the same high voltage source to optimize the performance/price ratio (see 1.2.1.8) in this way. The drawback of this solution is that a programmable gain amplifier in the analog chain (see 1.2.1.3) is needed to balance out gain variations of individual tubes. The adjustment of gains is based on digital potentiometers of type AD 8403. The controller FPGA drives a protocol to transfer 10-bit values into any of these devices on the AB.

Another supported function is the control of the test pattern generator which can simulate rectangular PMT pulses of variable width and amplitude at the input of each analog channel. The controller FPGA drives a switch on the AB per channel to couple a pulse (fixed DC amplitude) into the analog chain. The pulse width, the number of channels involved and the sequence are parameters of FPGA internal memory of FLT and SLT, and are determined by PC in advance. The involved pixels are coded in FLT memory. The timing and pulse width are controlled by SLT memory; the pulse amplitude is adjustable by a DAC at the SLT board and common to all FLT channels.

Calculation of the multiplicity:

The control FPGA calculates each 100 ns the multiplicity, i.e. the number of pixel triggers of the FLT board. The digital backplane provides 6 bits to transport this information from the right most FLT to the (left most) SLT via daisy chain lines. The 6 daisy chain input lines contain the summed up multiplicity of all FLTs to the right of the current position. The FLT adds its own multiplicity to this information and code the new multiplicity sum in the 6 daisy chain out lines (which are connected to the input of the left side FLT). In this way the multiplicity signal is provided to the SLT with a delay of 2 µs, but with 100 ns resolution.

1.2.1.5 SECOND LEVEL TRIGGER

The pixel triggers generated for each channel of the 20 FLT boards in a sub-rack are read via the backplane into a single Second Level Trigger (SLT) board. The functions of the SLT are shared between two FPGAs: the „Trigger FPGA (T-FPGA)" and the „Controller FPGA (C-FPGA)". They are both connected to a dual-port RAM, which works as a circular memory to store pixel trigger, multiplicity and other trigger information.

Functions of the T-FPGA

The task of the T-FPGA is to generate an internal trigger if the pattern of triggered pixel looks like a straight track that might be produced by fluorescence light. The algorithm of the T-FPGA regards as straight track the 5 fundamental topological types of pattern shown in figure 36 (top) and those created by rotation and mirror reflection (in figure 36 bottom).

A lot of tracks will not pass through the center of the pixel and the PMT may not record enough light to trigger. To allow for this situation and to be fault-tolerant against defective PMTs the algorithm requires only 4 triggered pixels out of the 5-fold pattern mentioned above. Taking into account that identical 4-fold pattern with a gap can originate from different 5-fold hole combinations, we count 108 different pattern - so called pattern classes.

Instead of checking the full matrix for all 108 classes at once – which would be 37 163 combinations – we have implemented a pipelined mechanism (see figure 37), which searches for track segments on a smaller 22x5 sub-matrix. Every 50 ns the T-FPGA reads the pixel trigger of one FLT (22 pixels + parity) into a pipelined memory structure. While the full matrix is scanned in this way within 1 µs, a coincidence logic simultaneously analyses the contents of the pipelined memory structure to find track like patterns. It consists of 2102 4-input AND gates to check all patterns followed by OR gates to group combinations of patterns belonging to the same pattern class. A decoder evaluates from these signals a 7-bit result R and a class multiplicity m_c with the following meaning:

a) if R = 0, then there was no pattern found and $m_c = 0$,

b) if 1<= R<= 108, then the logic has recognized at least one pattern of class number R and $m_c = 1$,

c) if R= 127, then the logic found patterns of more then one class, i.e. $m_c >= 2$.

In case b) and c) an internal trigger signal is generated for further processing by the C-FPGA.

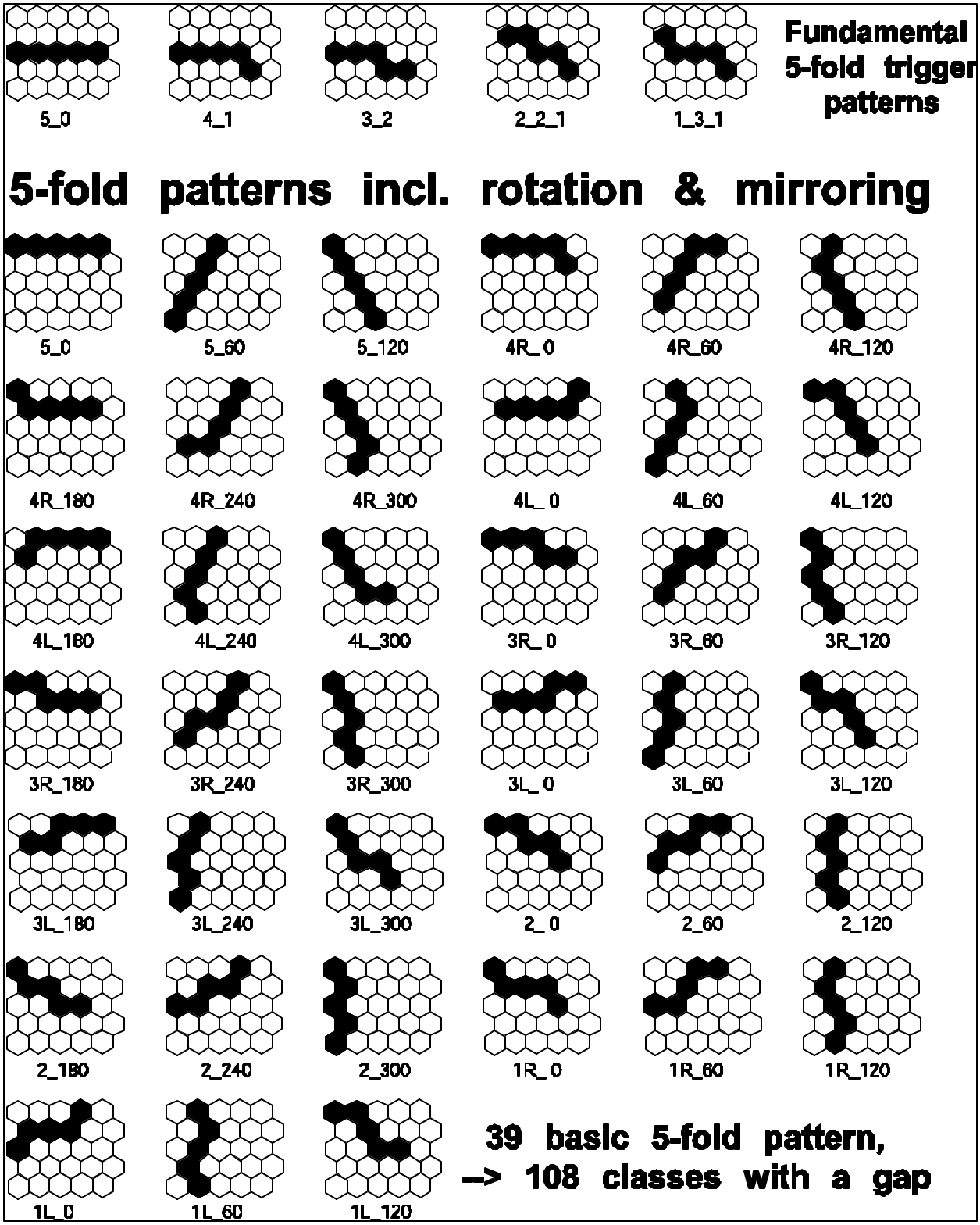

Figure 36: Fundamental types of 5-fold pattern (top) and all 39 basic patterns after rotation and mirror reflection (bottom).

The SLT pixel memory

To avoid finding the same pattern twice, the T-FPGA logic demands a valid trigger in the leftmost column of the matrix. The pixel triggers of this reference column, a parity error bit, the status of the external trigger, trigger status of adjacent telescopes, and the result R are stored in the pixel memory every 50 ns. This information is found to be most useful for the subsequent software trigger stage as it summarizes all necessary information to reject random triggers without the need for time-consuming raw data readout. In addition, we write the 6-bit multiplicity information every 100 ns (3 bit every 50 ns) into this memory. Simple commands are provided to access this information from PC without the need of clumsy bit manipulation operation.

As the memory must be accessible for R/W independently at 20 MHz we use a dual-port, synchronous RAM of 128K x 36 bit, which is divided in 64 memory pages of about 2000 words. This is the same organization as circular memory like the RAMs of the FLT. As the page number of the pixel memory is always synchronous with the FLT page number, the memory management and readout is simplified.

Functions of the C-FPGA

The C-FPGA is responsible for the following tasks of the SLT board:

- System synchronization: The SLT receives from the GPS clock the 1 pps (pulse per second) signal and the 10 MHz clock. These signals are distributed over the bus to the FLT boards and the T-FPGA to synchronize all system parts. Delays in the FPGAs have to be compensated.

- Distinguish different trigger sources in the trigger logic:

  1. internal triggers (ITrg) from the T-FPGA,

  2. triggers from the adjacent left and right telescope,

  3. external trigger (ExTrg) state centrally distributed through the GPS, and

  4. triggers induced by software from the PC.

  When any of this triggers is present for the first time (and not disabled by the trigger mask register), the C-FPGA waits for a programmable time, e.g. t_t=70 µs. Any further trigger during this post-trigger time is regarded as part of the same event. When the waiting time is expired, a next-page-signal (NxPg) is distributed with the next 1 µs strobe to all FLTs and the T-FPGA to cause all cyclic memories to switch to a new page address. In addition – ITrg –Signals are distributed to the adjacent left and right telescopes in case pixels of the outermost 4 column are involved. Neighbor systems can be programmed to except them as trigger source even in case they have no own internal trigger. In this way we compensate trigger inefficiencies for short tracks across telescope boundaries.

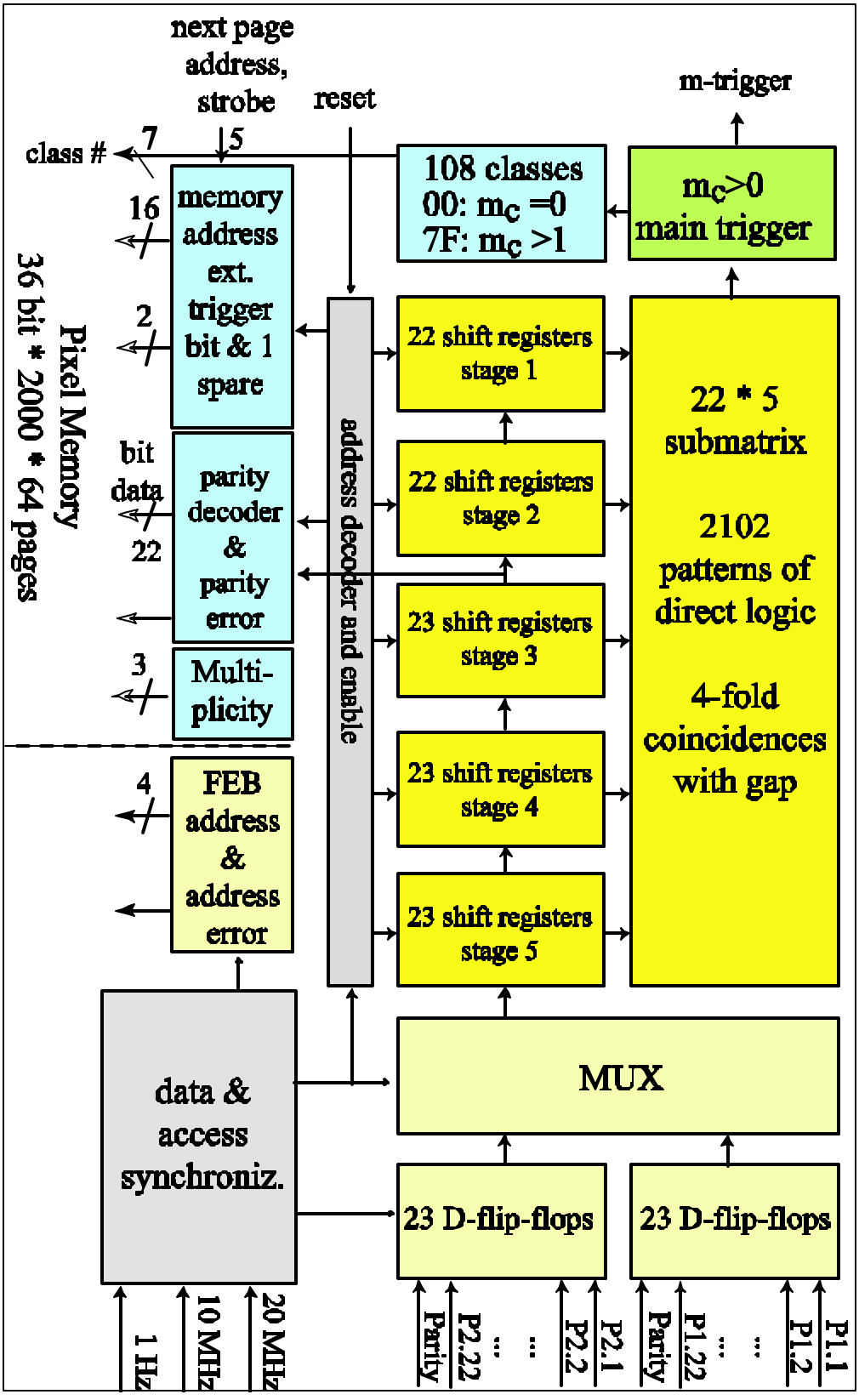

Figure 37: Pipeline architecture of the SLT T-FPGA

- Time management: The C-FPGA keeps a 32-bit counter for the absolute time, which is preset at run start by the MirrorPC with the number of seconds since January 6th, 1980 [28]. It is incremented every second on arrival of the 1 pps signal. Another counter holds the sub-second time: 14-bits are used to code the number 0..9999 of 100 µs steps, 11-bits hold the number 0..1999 of 50 ns steps inside a 100 µs frame which represent the address used to write to the circular memories. The C-FPGA provides for each memory page internal registers for the value of these time counters at the time a NxPg signal is generated and at the time the first trigger occurred. For each trigger source participating in the event a control bit is stored.

- Memory management: A status bit defines any of the 64 memory pages to be either 'empty' (=0) or 'full'(=1). Based on this information a decoder finds the lowest empty page address to be used as new page at the NxPg signal. The bit is set to 'full' for the old page with the NxPg signal. It is reset to 'empty' by the PC after readout of the raw data or in case of event rejection by the software trigger. In addition, the PC can set the status permanently to 'full' for those pages which are found to have faulty memory locations. If all pages are already filled the data writing in SLT and FLT memory is stopped via an internal inhibit signal. The data taking continues as soon as any page is set free by the PC.

- Decode status signals from the GPS clock: 2 signals from the GPS clock define 4 states of the overall system. These states are:

  1. **Global inhibit** state: The experiment is stopped, the inhibit signals is distributed to all FLT.

  2. **Normal run** state: The experiment is running and the telescope will record date unless not blocked by internal inhibit (all pages full) or by software inhibit.

  3. **External trigger** state: During this state the external trigger bit (ExTrg) will be recorded in the pixel memory. If enabled, the transition from run to external trigger state will issue an internal trigger to ensure the data recording of events with artificial light sources e.g. during calibration.

  4. **Veto** state: During this state the data taking continues, but all triggers are inhibited. This mode is useful to avoid recording of events during the operation of the LIDAR in the telescope's field of view.

- Slow control functions: The C-FPGA is connected to a multiplexed 8 channel 12-bit ADC (Max 530). The ADC measures periodically 3 supply voltages and the signal of 3 temperature sensors. The values are monitored to stay within individually programmable margins for each channel. They are accessible as well by PC and can be stored with the raw data.

- Interrupt generation in case of:

  - a valid trigger is found, i.e. a NxPg is generated internally, or

  - the experiment is stopped, because all 64 memory pages are ‚full', or

  - a parity error occurred reading the pixel triggers from the bus, or

  - receiving interrupts from any FLT, or

- any slow control parameters are out of range.

The interrupt generation for each of these trigger sources can be suppressed using the interrupt mask register.

- Test pattern generator: A part of the test pattern generator is implemented in the C-FPGA logic. The logic reserves memory space used to generate a chain of timing signals (TPuls) which start & stop test pulse generation on the FLT boards. A DAC (Max 197) is interfaced and used to generate a DC level equal to the amplitude of the pulses.

- PBUS+ slave controller: The SLT has to respond to the PBUS+ protocol to allow the PC access to the pixel memory and internal registers.

- Configuration EPROM: All FPGAs on SLT and FLT boot in parallel at power up or on demand of the PC. The booted firmware is stored in 5 serial accessible EPROMS (EPC2TC32) located at the SLT. Temporary overwriting of the boot firmware is possible with a special cable via the JTAG connector on the SLT or FLT front panel. Permanent updates of the boot EPROM is possible via JTAG on the SLT.

Future options for the SLT

At present the multiplicity information is written with 100 ns resolution into the pixel memory. If we have in future ascertained a good algorithm to discriminated shower from muons and lightning using the multiplicity we could also implement it in SLT firmware.

1.2.1.6 Interface to PC via FireWire interface (IEEE 1394)

Each MirrorPC is equipped with a FireWire interface card which connects to a FireWire to PBUS+ converter board – called FireWire SIB module. The module provides an inexpensive fast standard serial interface between FE electronics and the MirrorPC. The large amount of memory address space, high transfer rate of 400 Mbit /s and low cost make the FireWire bus a practical solution to bridge between PCI (MirrorPC) and PBUS+ (front-end sub-rack).

The FireWire SIB module is adjacent to the SLT and connected through three 50-pin connectors as shown in figure xx. It shares the front panel and stiffener bar with the SLT.

The system architecture of the FireWire SIB is depicted in figure xx. The TI chip TSB43AA82A has been chosen as an integrated physical and link layer controller for the IEEE 1394 bus. It is compliant with the IEEE1394.a-2000 specification. In addition, an Altera FPGA (EPF10K100QEC240) was used to implement a 32-bit NIOS-CPU and a fast DMA-PBUS link. The internal FPGA memory holds the NIOS program code; two external 64 K x 16 bit SRAMs operate as external data storage. The complete configuration is stored in Altera serial EPROM and is loaded at power up. A higher density Altera FPGA (type EPF10K130) can be mounted optionally to increase internal RAM space for program code.

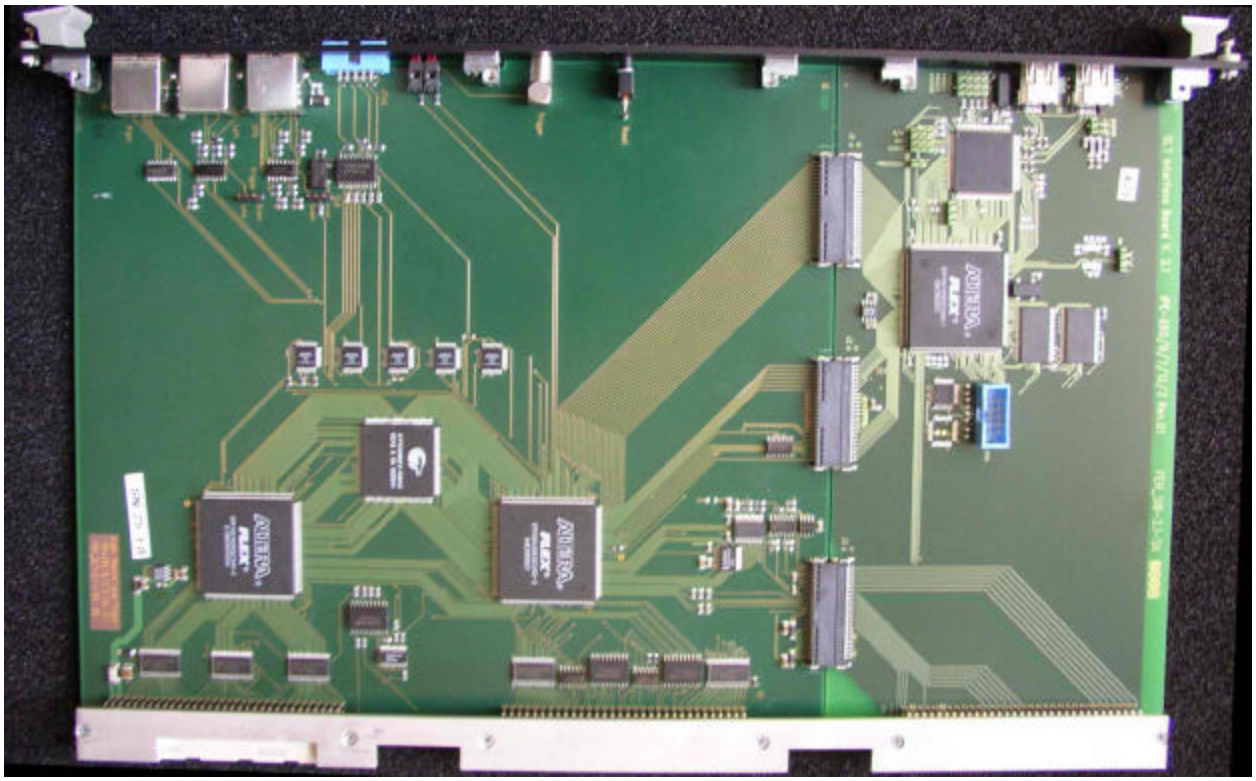

Figure 38: Photo of SLT (left) and FireWire SIB (right)

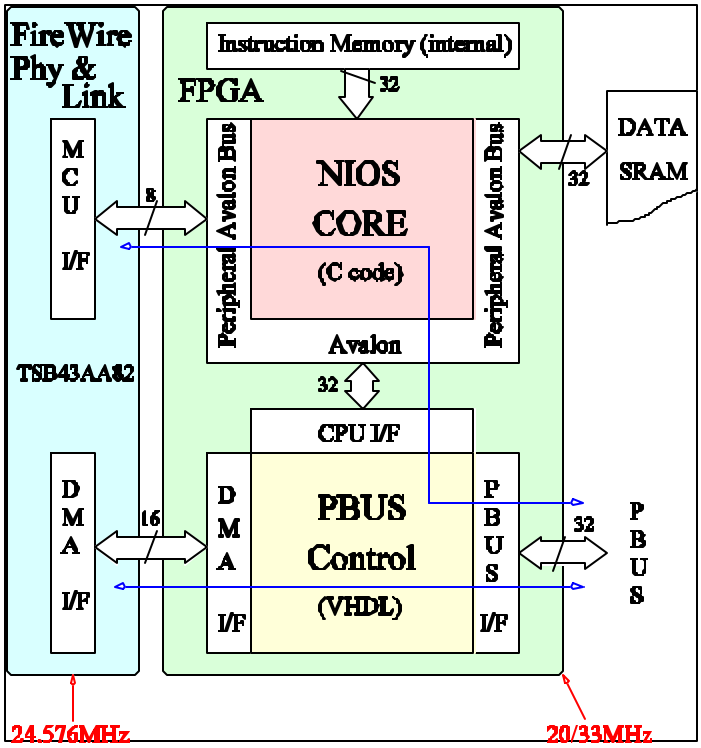

Figure 39: System architecture of the FireWire SIB module

1.2.1.7 GPS Clock module:

The GPS clock is based on the GPS receiver Motorola Oncore UT+, which is the same module as used by the surface detector and shown in figure xx. The main task of the clock is to distribute timing and control signals among telescopes located in the same Fluorescence Station. Following signals are transferred to the front-end through 20 m long LAN cables:

- the 1 pps signal from the Motorola module with an high accuracy of a few 10 ns and a correctable jitter of +/- 50 ns (saw tooth parameter),
- a 10 MHz signal, which is derived from an 80 MHz crystal oscillator whose frequency is permanent monitored by counting the number of periods between successive 1 pps signals,
- 2 control signals to specify the states “global inhibit”, “normal run”, “external trigger” and “veto”.

In addition, the firmware of the GPS module provides following additional features:

- 4 gate generators can produce logic signals to control the external trigger and veto state. The rising edges of the generators (absolute time and sub second time) are programmable as well as the frequency (every n^{th} second), the width and the total number of signals generated.
- 4 input channels: Signals from calibration sources (Xe-lamp, blue LED) or the LIDAR can be used to generate external trigger or veto state.
- 2 capture inputs: The times of leading and falling edges of signals at these inputs will be stored in memory (maximal 256 times). One of the inputs is intended to record the time window of LIDAR system operation.
- One output provides strobe signals to trigger the LIDAR at defined times and a defined frequency of 20 Hz or 1 kHz.
- Auxiliary outputs to monitor the 1 pps signal, the 10 MHz and the control lines. The status of the module is in addition displayed by 8 LEDs on the back side.
- RS232 serial interface to the EyePC: This link is used to configure the Motorola receiver as well as the modes of the GPS module. There are software commands to start/stop the measurement, setup of the gate generators parameters and to readout the register with the capture input times. In addition, the module sends automatically each second the Motorola saw tooth parameter (for correcting the 1 pps), the number of 80 MHz periods and a value defining the phase between the 1 pps and the 10 MHz signal.

All functions of the module are implemented in reprogrammable FPGA logic; details are specified in the user’s manual [xx].

Figure 40: Photo of the GPS module at the test bench: The front panel holds the BNC connectors for input and output signals; the status LEDs, the LAN connectors, the RS232 interface and the "Reset" push button are on the back side. Also visible are the Motorola receiver (right) and the FPGA (center).

1.2.1.8 HV/LV Power Supply System

Introduction:

The Fluorescence Detector consists of 24 telescopes grouped in sets of 6 units in each of the 4 Fluorescence Stations located at the periphery of the site.
Each telescope comprises the Camera consisting of an array of 20 x 22 photomultiplier tubes (PMTs) biased and readout by the Head Electronics (HE) units which are soldered to the PMTs. Each PMT + HE assembly constitutes a pixel and requires both high voltage (HV) and low voltage (LV) supplies. Each FD station has 2640 pixels. The total number required for the whole Southern site is close to 12000 units, including ~10 % spares.

The configuration adopted for the full observatory is based on the new CAEN SY1527 modular system which integrates HV and LV power supplies into a single sub-rack for all 6 telescopes.

The system uses 6 HV modules each one delivering 12 channels with individually programmable HV level. Ten channels are used and two are left as spares. The HV can reach at maximum 1300 V. To help reaching uniform gain in the whole Camera, 44 PMTs with similar gain are grouped together. Each Distribution Board (DB) receives one HV channel that bias a group of 44 channels. The HV for one full telescope is provided by only one A1738P HV module.

The LV modules have 6 channels and, as the Head Electronics require positive and negative supplies, we grouped two sets of 4 DB's (196 channels) and one set of two DB's (88 channels) as the best possible grouping of LV's. The results are very satisfactory as all 440 HE's require the same voltage: +6 V and –6 V. The division in three groups gives additional flexibility, useful during special tests or just for debugging of the telescope(s).

Only one mainframe plus 6 HV modules and 6 LV modules are required for the whole Fluorescence Station. Four such systems will therefore be installed.

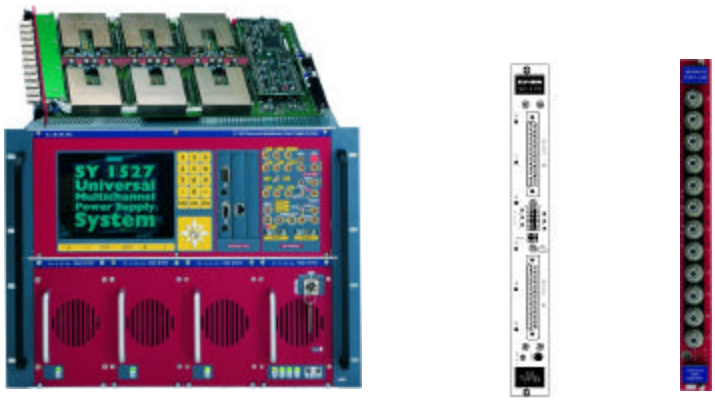

Fig 17: The CAEN SY1527, the LV and HV modules of the HV/LV PS system.

The LV and HV architecture:

H

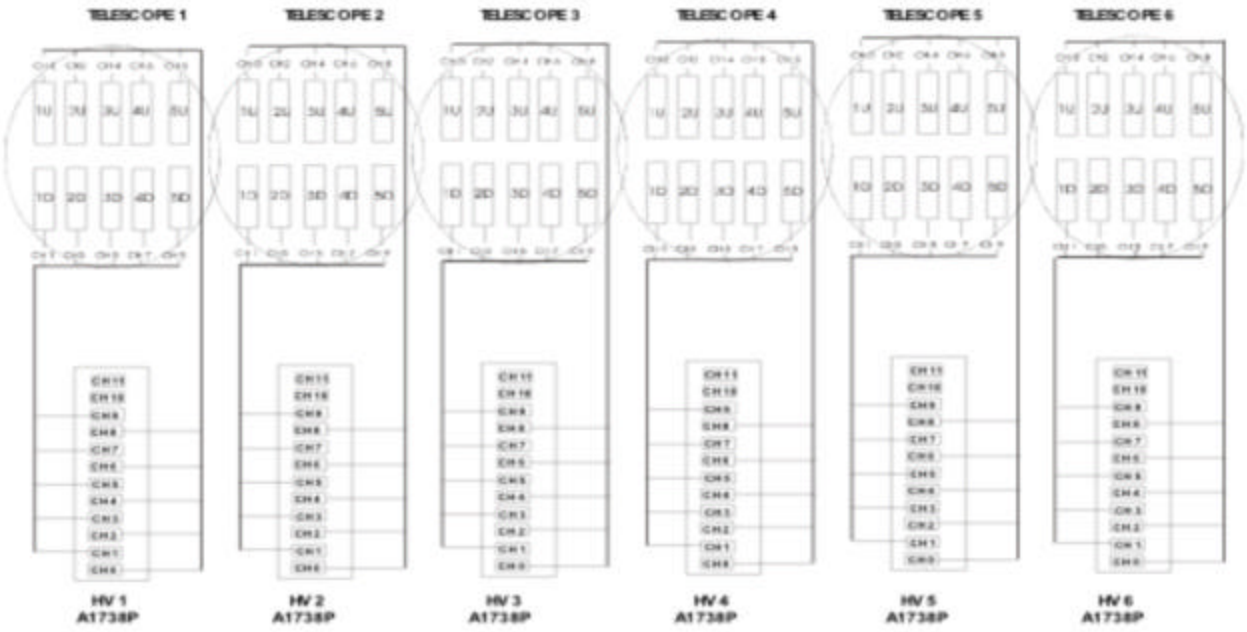

Fig 18a : The architecture of the LV distribution system.

The LV distribution system is based on 6 A1517LV modules with 6 LV channels per module. Two groups of 196 channels plus one group of 88 channels are served by a single LV module. The power dissipation is well below (< 70 %) of the maximum power rating delivered by the module.

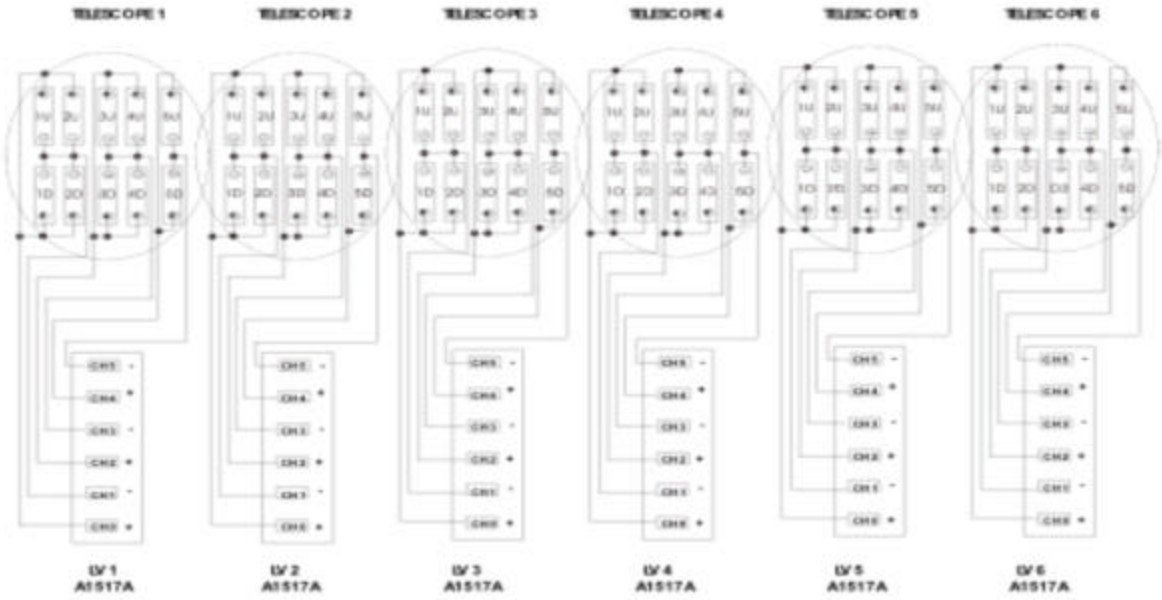

Fig 18 b: The architecture of the HV distribution.

Further technical details are included in a comprehensive report on the HVLV PS system [GAP–094-2003].

Concluding remarks: The HV/LV PS system is reliable and cost effective. The LV and HV distribution architecture adopted ensured an optimal use of a commercially available system.

1.2.1.9 Power supply and fan unit of the front-end sub-rack

The FE sub-rack is a commercial VME/VXI sub-rack (type 6021) from Wiener Plein & Baus GmbH. It consists of the power supply (UEP 6021), the mechanics (bin UEV 6021, 400 mm deep, 9U high) and the fan tray unit (UEL 6020). All power supplies and fan trays are pluggable and easily to exchange, the fan trays even during power-on state.

The power supply (UEP 6021)

The power supply is mounted vertically behind the digital backplane. It can be tilted by 60 ° to allow access to the digital backplane as shown in figure xx (section FLT backplane). The supply is a microprocessor controlled switching power supply designed in the high density Wiener cavity technology for extremely low noise output voltage. It contains power packs for the digital voltage +3.3 V (and +12 V optional) and the analog voltages +5 V and -5 V to supply the AB and the

ADCs on the FLT. The mains input includes a power factor correction (PFC) module according to EN 60555-2/IEEE 555-2 for sinusoidal current consumption. To ease the turn-on of the sub-rack via slow control we have ordered the power supply with the auto-start option, i.e. applying AC power switches the front-end on in case it was on at power down.

To protect the power supply and the FE modules, the power packs are microprocessor controlled turned off in following cases:

- Overheat: in a power pack (each pack is equipped with a temperature sensor) or in the air outlet a maximum temperature is reached.
- Overload: a maximal current (programmable per voltage) is exceeded.
- Overvoltage: a voltage exceeds a programmable value or 125 % of nominal value.
- Undervoltage: a voltage falls below a programmable lower level.
- Fan failure: at least one fan fails.

The power consumption as measured in operation is compiled in table xx below. One has to mention that the consumption at 3.3 V depends very much on the version of the RAM IC: the latest revision reduces the consumption from 1.8 A to only 0.7 A per FLT.

voltage	Imax [A]	Consumer
+ 3.3 V dig.	< 30	digital logic, FPGAs, RAMs
+ 5 V analog	< 30	analog circuits on AB, ADCs
-5 V analog	< 12	analog circuits on AB

Table 3 : Overview of supply voltage and maximum current at worst case condition. The output power stays in any case below 340 Watt.

Grounding scheme

Ground points at the back of the camera body and at the backplane of the sub-rack are used as reference ground points. All ground lines originate from these ground points in a star-like fashion. Different parts of the readout chain are always linked via differential signal lines (LVDS technique) to avoided ground loops. In order to reduce interference through the AC power lines (as was noticed during prototype operation) we have separated each AC line to the MirrorPC or sub-rack with a transformer from the remaining “dirty” network for the air conditioning, motors and lighting. The transformers are very effective: Interferences due to switching lighting or motors, which were present with the prototype, have vanished

1.2.1.10 Production and test procedure:

The high number of channels, the complexity of the system and the expected time of operation require the use of modern tools for testing and trouble shooting. For this reason we have foreseen 4 independent test steps:

1. Electrical defects like short circuits and breaks are detected during in-house production. IPE has procured a needle probe for that purpose which tests all signal lines for continuity and for short cut against neighbor lines. The soldering quality (especially for soldering joints underneath BGAs) is regularly visually inspected with an inspecting tool. Defects found are directly cured by our production center.

2. The analog board (already qualified by Torino group) and the FLT are interconnected, mounted to a common front panel and stiffener bar, and tested in our single board test setup (see figure 41). The FPGA firmware is loaded using the PC parallel port and the FLT JTAG connector. Readout of the FE modules (FLT or SLT) is possible through the microEnable PCI interface card and a PBUS+ interface on the test setup.
   The single board test includes:

   - the measurement of all supply currents to find short cuts or other abnormal behavior of ICs,
   - a memory test to find faulty memory modules and to test thereby nearly all digital lines and the communication via the backplane,
   - the determination of variance (= electronic noise) and pedestals to verify the input stages in front of each ADC,
   - the verification of threshold regulation to check internal FPGA logic, and
   - the test of the full signal chain by injecting an external pulse to all channels in parallel. This simple test finds channels with abnormal gains, problems in the anti-aliasing filter or the ADC.

   The results of all tests are recorded in log files by the FDLabTest program (see 1.2.2.4); the operator gets a passed or failed classification.

3. Working FLT and SLT modules are compiled in sub-racks and have to pass tests with the FDHwDiagnose software. The software can check the full FE functionality and is very useful to set and readout parameters for all 440 channels. PMT signals can be generated (taking advantage of the internal test pulse feature) to verify the full signal and readout chain. In addition, every working sub-rack has to pass through thermal cycling in a climate chamber at full operation. 6 temperature cycles between 0 °C and 40 °C are followed by a 16 hour burn-in test to provoke break down by aging. Functionality tests are repeated before sub-racks are shipped on side.

4. During installation and commissioning we can use all test tools described in section 1.2.2.4. After passing functionality tests, the sub-rack is connected to the camera and the test repeated.

With connected camera, the full signal path from PMT to ADC can best be checked using light from the numerous light sources present for calibration purpose.

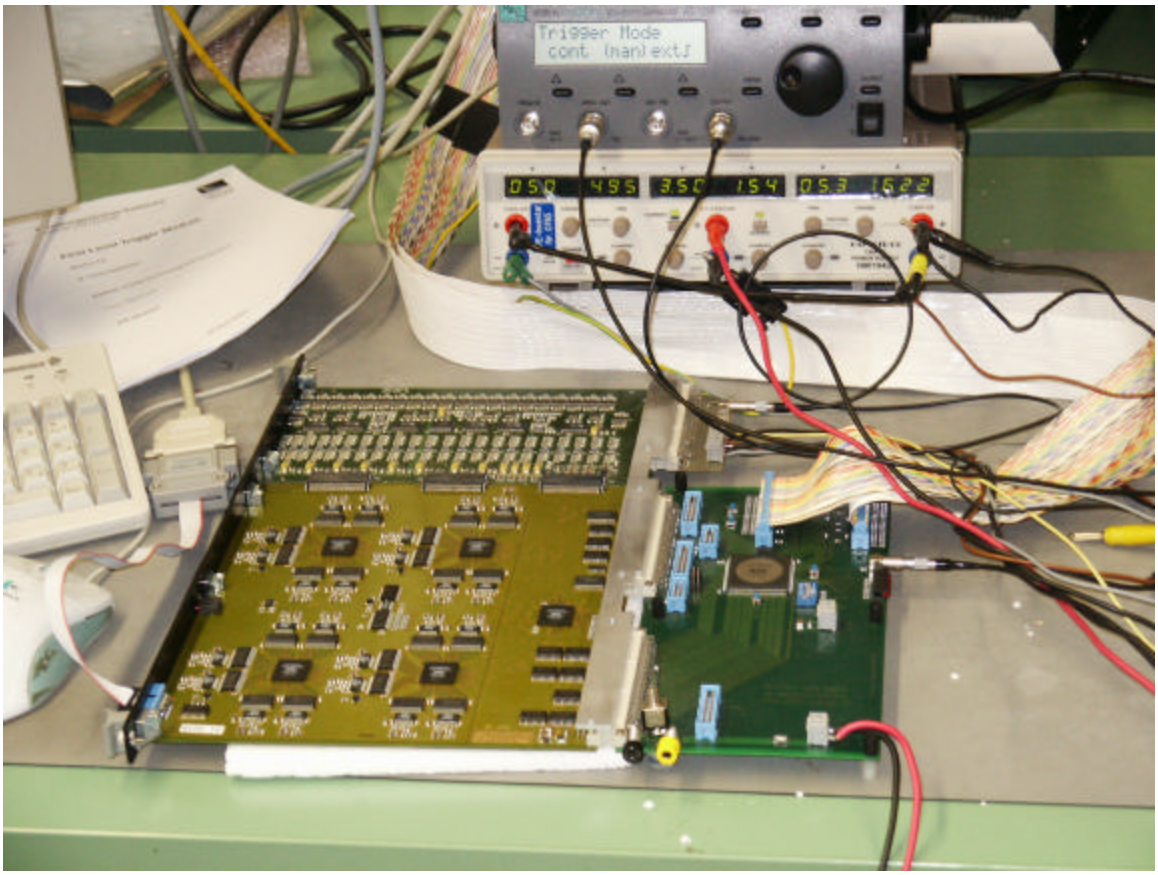

Figure 41: Single board test setup (right) connected to FLT and AB under test. The FPGA firmware is loaded using the parallel port and JTAG connector.

1.2.1.11 LED Calibration Unit

The LED Calibration Unit (LCU) is needed to simplify the electronic gain measurements. It consists of a programmable current pulser to drive a blue LED (470 ± 25 nm), a Si photodiode to sense the LED's pulse shape and 12-bit/10 MHz ADC to record the photodiode's signal. A microcontroller based on a DSP and a FPGA is the logic core of the LCU which provides also an Ethernet port for communication with the EyePC and CalibrationPC.

The amplitude of the current pulse is adjustable by a 10-bit DAC; its duration is programmable in 25 ns steps. Typically, the LED is driven by 500 mA squared pulses of 50…70 µs length. The pulses are distributed via a 1 to 7 optical splitter and via optical fibres to the telescope's mirror centre, pass a diffuser to equalize the light directions and illuminate all 6 cameras simultaneously. The illumination causes anode currents of 300…600 µA (thus well inside linearity range) and signals of 100…200 ADC counts in amplitude per pixel. One output of the optical splitter is connected to the Si photodiode. The photodiode signal is recorded by the LCU's internal 12-bit ADC with 10 MHz sampling rate to verify the rectangular pulse shape and measure the relative LED intensity.

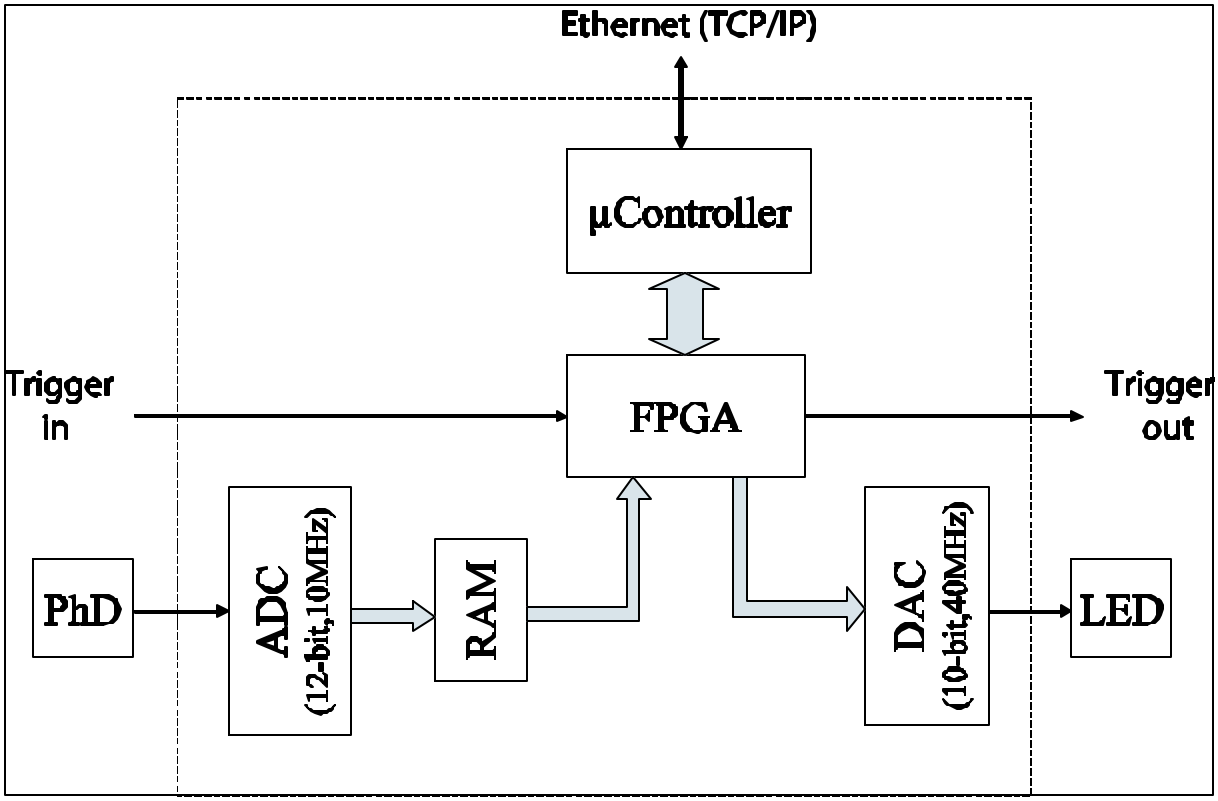

Figure xx: System architecture of the LCU with DSP, FPGA, ADC, RAM and DAC.

1.2.2 Software

1.2.2.1 Trigger Software

Varying conditions demand a flexible and configurable system. Thus a framework incorporating the basic desired functionality provides skeletons to the application programmers which are easily extendable to achieve the desired behaviour. The readout task, in addition, has different readout schemes which allow for an efficient readout adapted to the respective scenario.

The following description of the trigger covers only the scenario of real experiment data acquisition. Data recorded for calibration or test purpose are marked with an external trigger bit and bypass the trigger decision.

Every pattern recognized by SLT will lead to notification (via interrupt or polling) of the readout task running at the MirrorPC. Simulations show that the trigger rate for a 4-fold coincidence will be about 0.1 Hz at a coincidence time of $\tau = 20$ µs and at a mean pixel trigger rate of $f = 100$ Hz. In addition a significant contribution due to direct hits of the camera by cosmic rays increases this trigger rate to 0.3 Hz. This bunch of random coincidences and direct hits must be discriminated against real showers which is the main task of the Third Level Trigger (TLT) algorithms.

An easy way to improve the SLT trigger decision is to check that all pixels participating in an event follow a space-time linearity. Random space-time-orders or velocities far from speed of light are therefore a good indication for the mentioned background events. To test space-time linearity the trigger software reads the pixel memory on the SLT and the ADC data of a few, selected pixels and determines:

row and column numbers of all involved pixels from the pattern class information,

the time when the pixel has fired given by the memory address, and

the sequence in time and in space of these pixels.

Events are rejected if the sequence in time and space are inconsistence. Accepted events are valid T2 triggers and cause the ADC data of the corresponding pixels and eventually of a certain amount of pixels in their vicinity are read from the FLT memories.

1.2.2.2 Data Acquisition (DAQ)

The task of the FD data acquisition system is to collect the data of each individual FD building in a rather autarkic manner and to interact properly with the CDAS DAQ system, with various local calibration systems, and with the local slow control system (SCS).

Basically, it will be operated in three different modes depending on the way data is generated and processed:

acquisition and processing of air shower data,

acquisition and processing of real-like data, which are generated by external light sources for calibration reasons (e.g. laser shots, Xe flashers, LED calibration) and for the purpose of the atmospheric monitoring, and

acquisition and processing of artificial data created by the various test systems.

The expected high event rate during tests and - especially the calibration operation - requires a fast and efficient readout system for raw data transport from the front-end to the MirrorPC and eventually to mounted disks. Therefore, the readout process is the central process around which all the other data path related processes are grouped. These processes are:

readout of the data which is done in several steps,

processing and filtering tasks (e.g. several levels of software trigger), and

filling of histograms, monitoring and event displays tasks.

The FD data acquisition software task includes also the creation of scripts to ensure the automatic start of DAQ relevant processes on the DAQ systems and the establishing of general installation/de-installation procedures which can be followed by less skilled persons.

1.2.2.3 Performance Monitoring Software

The objective of the FD performance monitoring task is the permanent surveillance of FD telescopes hardware parameters, the monitoring of the software performance, the initial setting of hardware configuration and the storage of operating parameters and error/warning messages in log files. It is a concurrent task to the data acquisition activities. Both have to share CPU time and access to the FD electronics, but also have to mutually exchange status data and contact the slow control system. Thus the task is structured in following software programs:

- The *Mirror Monitor Daemon (MiMoD)* running on every MirrorPC reads out the pixel related data variance, pedestal, hitrate and threshold each 16 seconds, stores them in ring buffers of 500 words and compares them with some reference values.
- *The Eye Monitor Daemon (EyeMoD)* collects status information from the slow control system (SCS), the Mirror Monitor Daemons and requests trigger rates from the DAQ process. It fills ring buffers of 2000 words to build up histograms of the time-dependent quantities.
- On (or more) *Graphical User Interface (GUI)* programs can be started on each EyePC or in the Campus to request and display the information collected by MiMoD and EyeMoD for online inspection. The operator is informed about warnings and errors and can react accordingly by switching on/off individual pixels or by stopping the DAQ completely or partly.
- The *Star Monitor Daemon (StaMoD)* calculates for each visible star in the star list the position, i.e. the pixel(s) the star will be seen. These brighter pixels will be excluded from checks of the variance parameter in the MiMoD. In addition, the StaMoD requests automatically the variance (or threshold) data from the MiMoD ring buffers of those pixels, where a star transit has just occurred, and keep them in a file for off-line analysis.

- Messages of MiMoD, EyeMoD, GUI, SCS, StaMoD and DAQ are handled from a central *Logging Server (LogSer)*.

The overall design is shown in figure xx (below). In order to avoid network congestion we have to keep network traffic as low as possible. Data has to be analysed as close to the source as possible.
The inter-process communication is achieved through the use of:

a.) CORBA for the exchange of a few data words (messages and requests for actions),
b.) ROOT sockets for the exchange of huge amount of data like arrays of parameters and
c.) the OPC standard for communication with the SCS.

The performance monitoring software is running permanently as it is started as part of the boot process (except for the GUI and the StaMoD). The later programs are started manually.

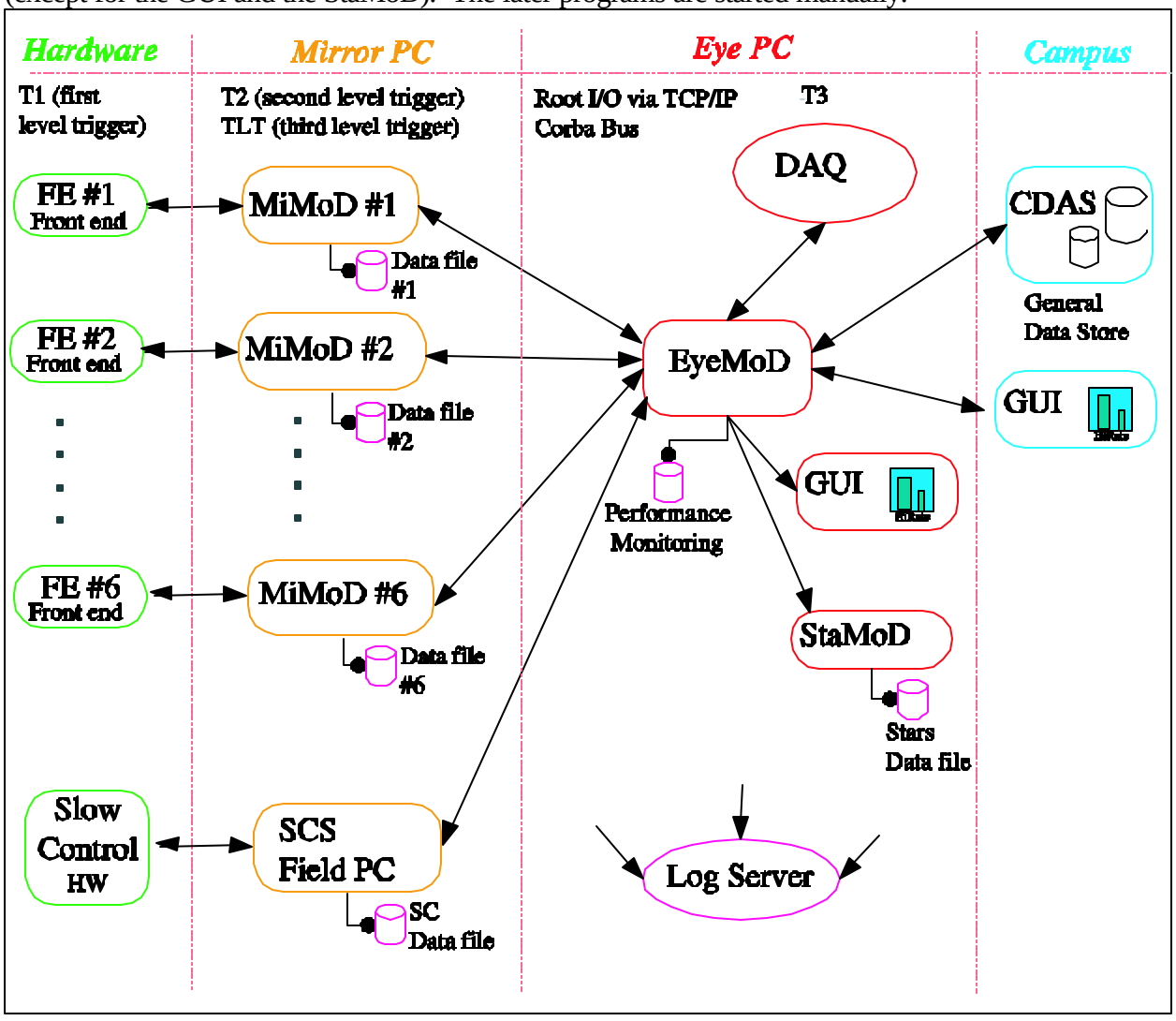

Figure xx: Structure of performance monitoring software components and their communications.

1.2.2.4 **Test Software**

A couple of programs have been developed to check perfect function of the FD electronics and the hardware access library (see 1.2.2.7):

FDLabTest – GUI program used for the test of single electronic module based on LabView (by National Instruments). The program is dedicated for quality assurance after analog board (AB) and First Level Trigger (FLT) modules are assembled to form a front-end module.

FDHwDiagnose – GUI Program to control all parameters of a full FD sub-rack. The application provides functions to readout event data (figure xx) generated with the built-in test pulser and background data. It is used to perform extensive tests of all parts of the FD electronics.

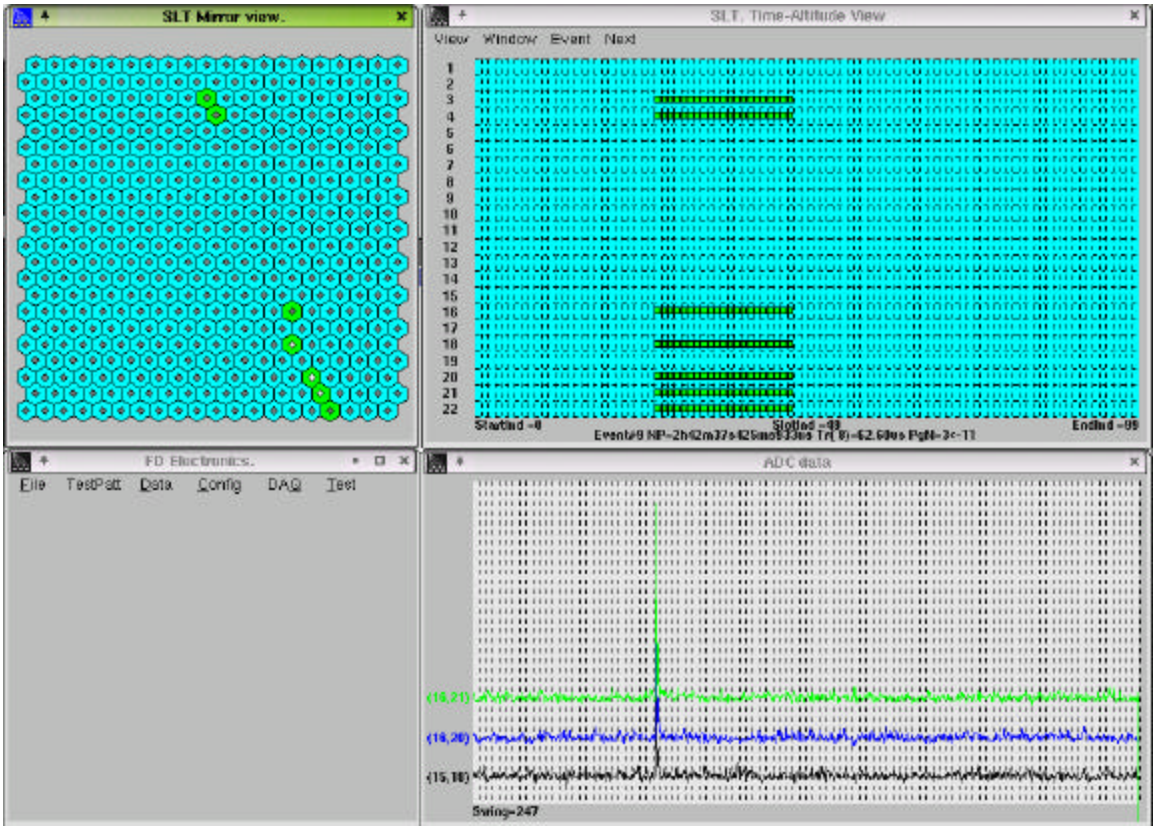

Figure xx: Event display of a muon with FDHwDiagnose. The program shows trigger data together with ADC data. Other functions allow configuration and test of the FD electronics.

FEtools – Collection of command line programs to set and display the status of the FD electronics. The advantage of command line applications is, that they can be used also remote from nearly every platform. The toolset consists of *Semtool*, *Feshell*, *Feexplorer*, *Pbusdaemon* and some more applications.

Semtool – Control of the SystemV semaphores. In case of abnormal program termination it can be necessary to release semaphores that have been left in the locked state.

Feshell – Command line tool to maintain the status of the electronics (figure xx). The program has function comparable to FDHwDiagnose. It can be used to examine the status of the FD electronics without interference a possibly running data acquisition. Parameter sets for every channel can easily be set using command scripts.

Feexplorer – Command line tool to display event data. The program uses the ncurses library for graphic-like output of the event data (figure xx). The program is intended for remote analysis of event data.

Pbusdaemon – Proxy interface to enable remote access to one or more telescopes in the Fluorescence Station.

```
11:46:32-Bay4>status
                                                 _______
     Eye      |||||      |||||      |||||   /  Bay 4 \    Bay 5      Bay 6
-------------------------------------------------------------------------------
 Unit        |Stat|       Load | Messages
 ---------------------------------------------------------------------------
 Telescope   |    |            |                                        crate 19
  +time      | ERR|  -70836  s | Hw-Mirror
             |    |            | Second counter is not synchronized

 SLT         |    |    stopped | 00 events recorded                        |soft
             | ---------+---------+---------+---------+---------+---------+----
  +inhibit   |warn|            | Software inhibit is active
  +trigger   |warn|            | Internal trigger source not selected

 FLT         |    |    running |
  +statistic |    |    running |
             |    |  140.27    +- 20.11 ADC values                    440 pixel
             |    |    4.15    +-  0.25 ADC variances / light level
  +hitrate   |    |    running |
             |    |  100.61 Hz +- 25.04Hz Hitrate                     440 pixel
             |    |    0.61 Hz | Control deviation          margins  90..110 Hz
  +threshold |    |    1.91    +-  0.30 over ADC                      440 pixel
11:46:37-Bay4>
```

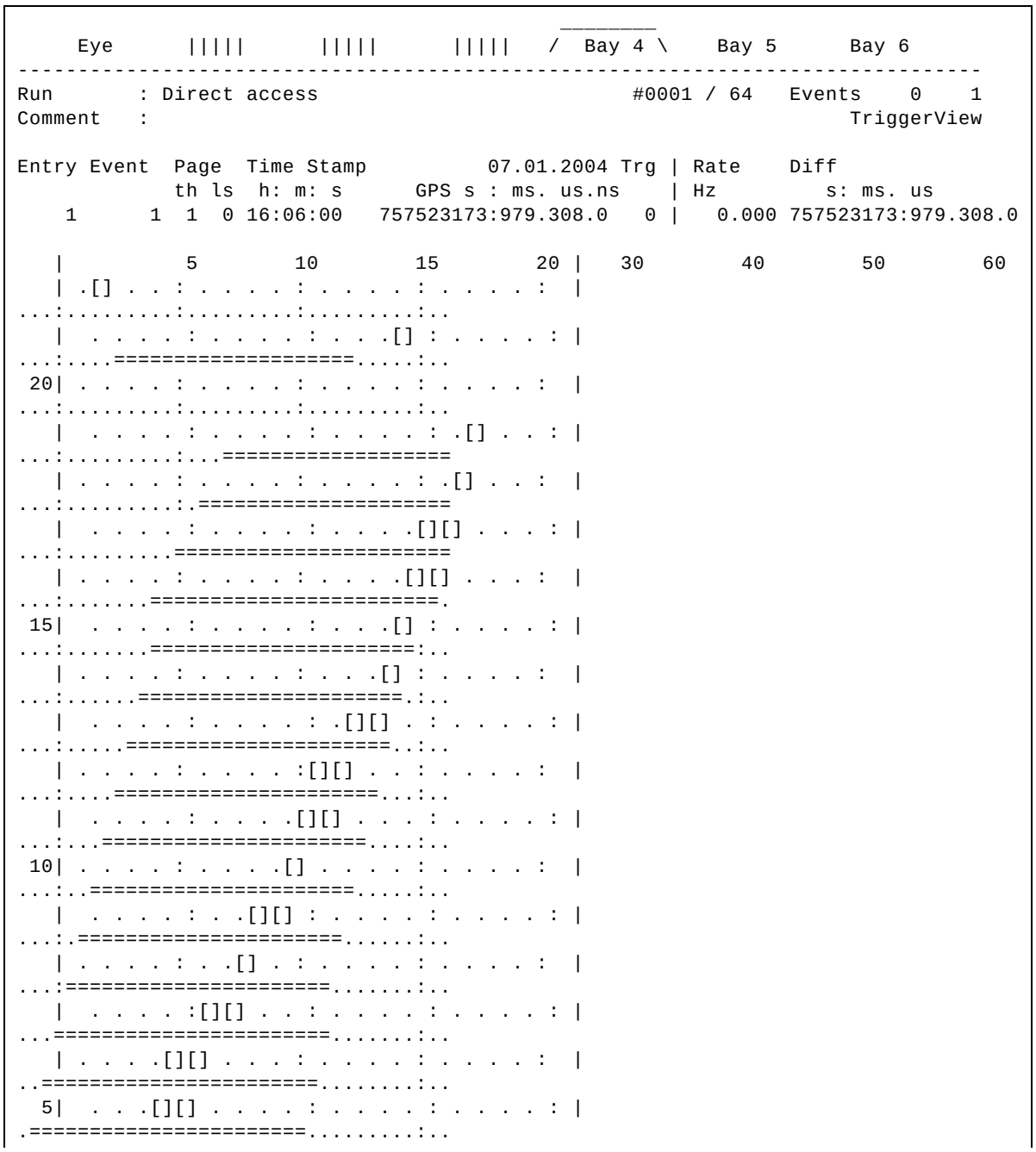

1.2.2.5 Graphical User Interface

In order to ease the operation of the software system a number of graphical user interfaces (GUI) will be provided as stated below:

The run control GUI to setup and steer the DAQ operation. It also displays the system status and the DAQ status.

An event display GUI to inspect event data quasi online or with small delays (figure xx).

The GUI of the performance monitoring task to inspect the recorded histograms as described in section 1.2.2.3.

In addition to providing these programs, procedures must be established for the installation of the GUIs on the graphical desktops of the DAQ consoles.

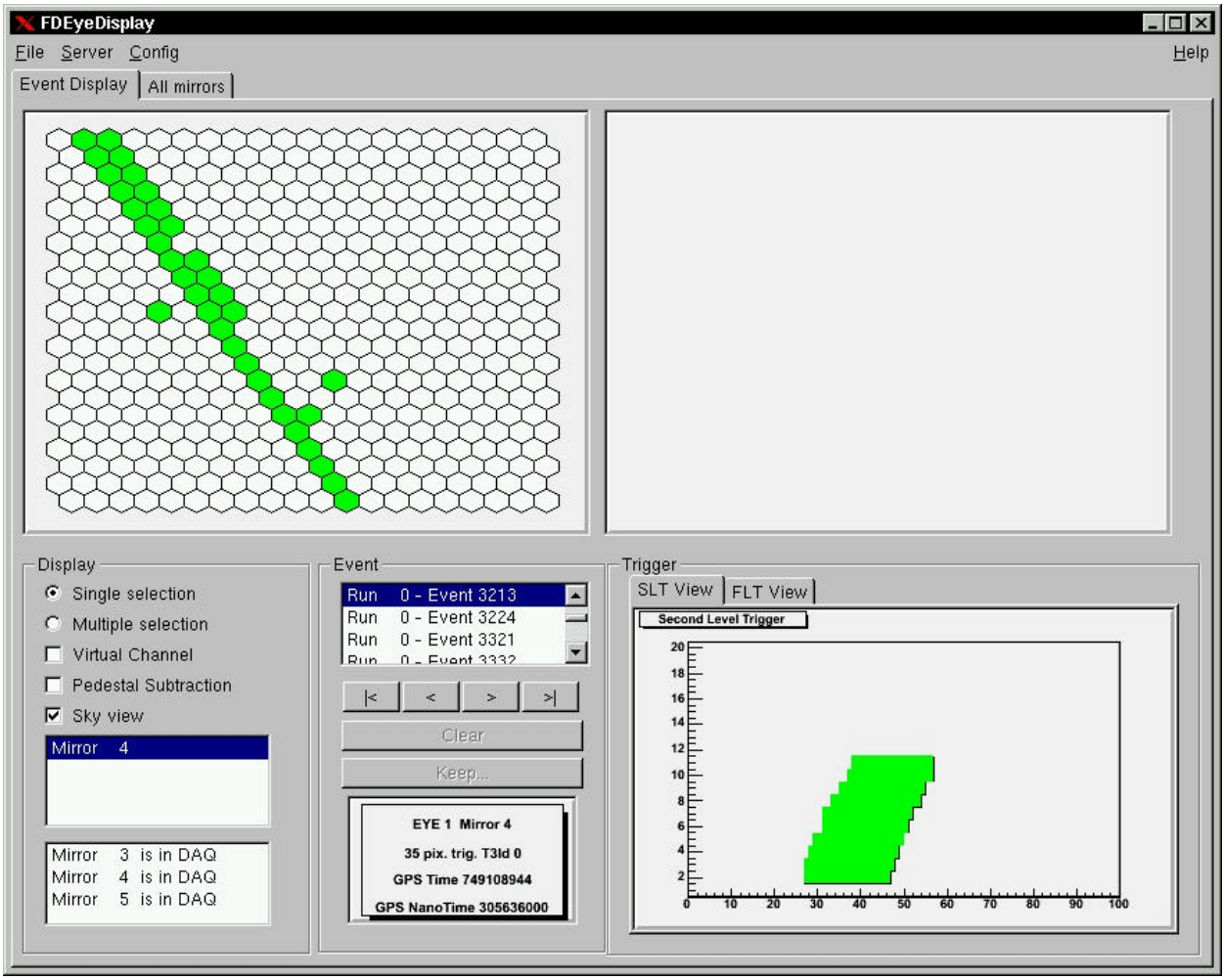

Figure xx: GUI Event display showing event 3213 in telescope #4 at Los Leones: The involved pixels follow a straight line on the camera (up, left) and the projection to the row axis is linear in time (low, right).

1.2.2.6 Event Building

Events classified by the MirrorPC as T2-trigger are sent to the EyePC. They are buffered there for max.10 s and will be finally recorded only, if a correlation with the surface array is confirmed by the central data acquisition system (CDAS).

Events from special calibration runs are readout if the external trigger bit is set. These data will in future be analysed on-line, calibration parameters derived and all information kept in data files per telescope.

Events recorded with ordinary shower setup are merged with the data of other MirrorPCs to form multi-telescope events (also if they originate from laser shots). The merging is done on the basis of the recorded event time by each front-end system. At this point some correction constants are applied to the event times accounting for clock inaccuracies and intrinsic offsets.

If events pass an even more stringent test of the space-time linearity (and other criteria like minimum energy, minimum track length to be defined during prototype phase) they regarded as T3 trigger. In this case the energy of the event is expected to be above 10^{19} eV and the event data will be always transmitted to CDAS and merged with SD data. The event builder has to make a decision within 5 s after the trigger has occurred as otherwise the information concerning the SD detectors data is lost in the CDAS data buffers.

The event building takes also care on special events originating from the various laser and calibration light sources, removes them from the main data stream and stores them optionally in separate files.

1.2.2.7 Hardware Level Software

The FD electronics can be accessed like a large memory block. Control and status registers as well as the data memory for all camera pixels have unique IDs in the address space. The access to the FD electronics is realized via an IEEE 1394 (FireWire) link to SIB board. This board communicates with the SLT and all FLTs via a simplified VME-like protocol - called PBUS+ (for “Peripheral Bus”). Figure xx shows the principal organization of the electronics and the hardware access library (fdhwlib). The library is organized in three layers: the transport layer, the register model and the application programmer interface. The advantage of this layered architecture is, that details of the actual implementation like the register model or the type of connection with the hardware can be modified with no or only little side-effects in the application program. Thus, the transition from the prototype microenable interface to the final FireWire solution was easily possible by adapting the transport layer library only. Application programs were neither affected nor needed to be changed.

The transport layer is defined according to the specification of the PBUS+ protocol. Main functions are read and write operations in single and block mode to registers and memory in the electronic modules. SystemV-style semaphores are used to synchronize the access of different processes. To allow a flexible use this layer can also be accessed from remote using the pbusdaemon. This architecture enables us to use diagnostic tools from remote during normal operation of the DAQ system.

The register model allows executing all functions of the electronics easily. It is used for hardware tests, diagnostic tasks and to implement the application programmer interface. The graphical diagnostic monitor (FDHwDiagnose) is based on this layer, too.

The third layer provides the interface for the DAQ system, monitoring and other processes. This interface is designed according to the physical function of the camera. The user can use this layer without knowing any details of the register model and also the large variety of hardware test features is omitted at this level.

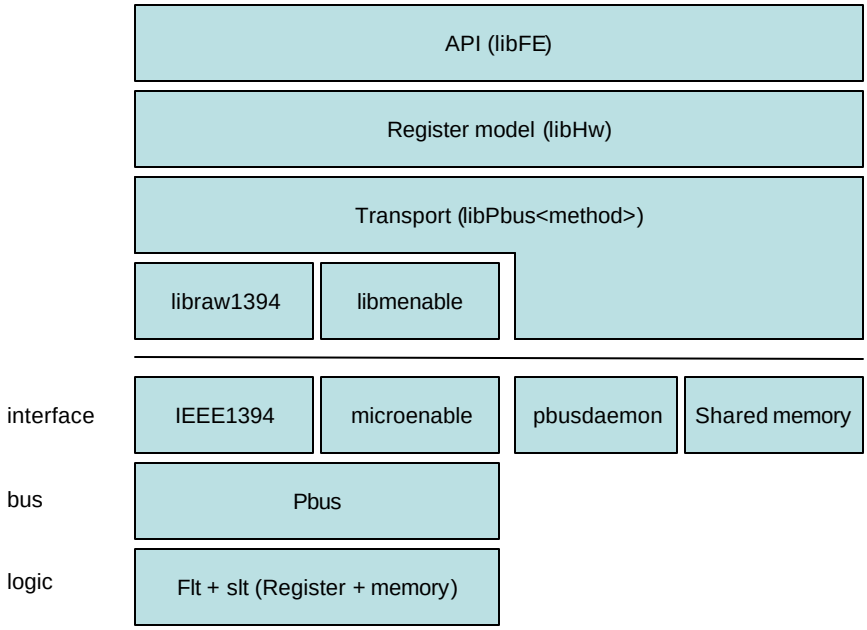

Figure xx: Organization of the hardware access library: There are two available interfaces to the FD electronics – IEEE1394 and the microenable interface. Each comes with a device driver and a basic access library. These libraries have been utilized to implement a transport layer (libPbus<method>) and register model (libHw) and finally the application programmer interface (libFE). The transport layer also allows remote access via the pbusdaemon from a PC connected through the LAN or – in simulation mode – to a shared memory simulating real electronics.

1.2.3 FD Slow Control System

The task of the FD Slow Control System (SCS) is to carefully control and supervise the operation of each FD telescope. The status of devices, sensors and actuators and other selected variables are monitored by the system and recorded, if they belong to safety relevant parts or are of general physical interest.

An application program running on a dedicated PC ensures that the experiment is always operating at safe environmental and valid infrastructure conditions.

All security relevant actions of the SCS are written to log-files. In addition some monitored data (e.g. wind speed, temperatures etc.) are written periodically to files. The use of XML file format allows for simple browsing or offline conversion into a database system.

1.2.3.1 Which parameters are monitored and controlled?

The SCS monitors environmental conditions, the status of devices and installations in the telescope bays and in the overall telescope building and also check its own integrity.

For each telescope bay it monitors or controls:

- an indoor light sensor located close to each camera,
- the shutter motor with its associated end switches,
- a key-switch that inhibits shutter operation (e.g. during manual work or drum calibration),
- a warning light or horn active during shutter movement,
- the fail-safe-curtain with its motor, magnetic brake and end switches,
- the HV enable switch,
- relays in the AC power line for the MirrorPC and for front-end sub-rack, and
- the status of the UPS unit that supplies the shutter motor and the local profibus devices.

In addition it monitors or controls following items specific to overall Fluorescence Station:

- wind speed, rain and outdoor light sensor,
- status sensors for the 3 access doors to the telescope bays and the emergency exit,
- the indoor and outdoor temperature,
- a power enable switch for the CAEN HV/LV main frame,
- a reset signal for the CAEN main frame's internal CPU,
- an overall interlock signal of CAEN main frame that prevents output of any voltages,
- all parameters and settings of the CAEN main frame (via OPC),
- the status of the central UPS that supplies the computers and the LAN system, and
- the shutter of the star monitor.

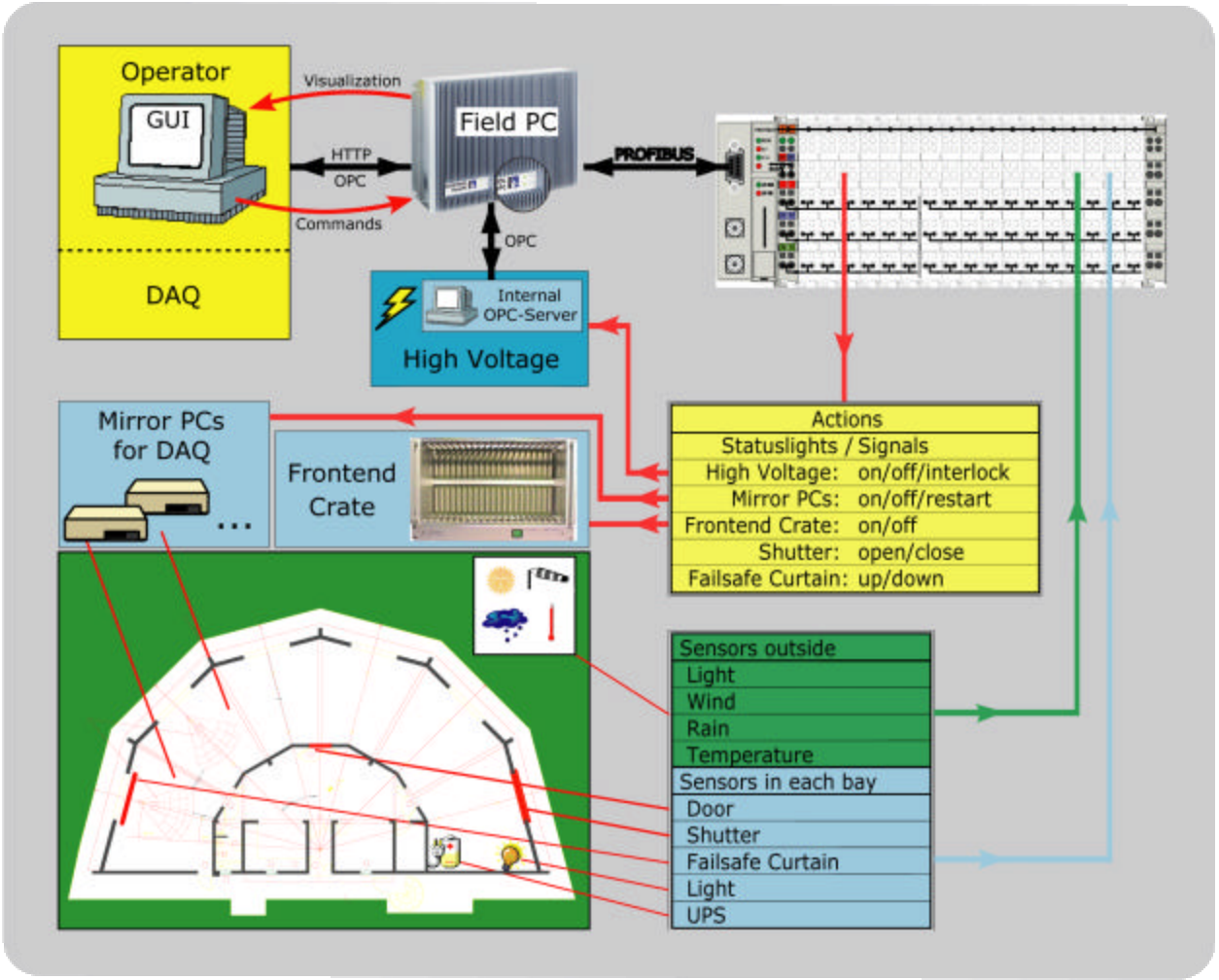

figure xx: Overview of the Slow Control System, its components and interconnections.

1.2.3.2 Technical implementation of the SCS

Sensors and actuators to be controlled are installed widely spread over the whole building. For practical reasons and to minimize the cabling effort we have implemented an electronic network controlled by a dedicated computer, the so called FieldPC. It is the same approach as is widely used in industrial automation, the so called *fieldbus* technology. The fieldbus connects the controlling FieldPC and its *programmable logic controller* (PLC) with peripheral input/output units. These I/O units are connected either directly via the fieldbus or via so-called *intelligent terminals* [29].

The advantages of the fieldbus concept are manifold:

- the use of commercial components avoids long development times,
- industry proven systems and components have a guaranteed reliability during the 20 years of operation,
- standard hardware interfaces can be used for many commercial sensor types and are easy to install, and
- debugging tools and test facilities are available.

The basis for our development is the slow control prototype system installed in Forschungszentrum Karlsruhe. It implements the same components as are installed on site in Argentina (if possible). It utilizes a PROFIBUS [30] master board as standardized in accordance to „Europäischer Feldbus Standard“ (EN 50170) to establish the fieldbus connection and the Profibus/DP protocol (sensor-actuator applications) as protocol profile. The principal setup of this system is shown in figure xx. Special bus terminals connect the sensors and actuators to a *terminal bus* (K-Bus). A fieldbus controller routes the K-Bus to the fieldbus.

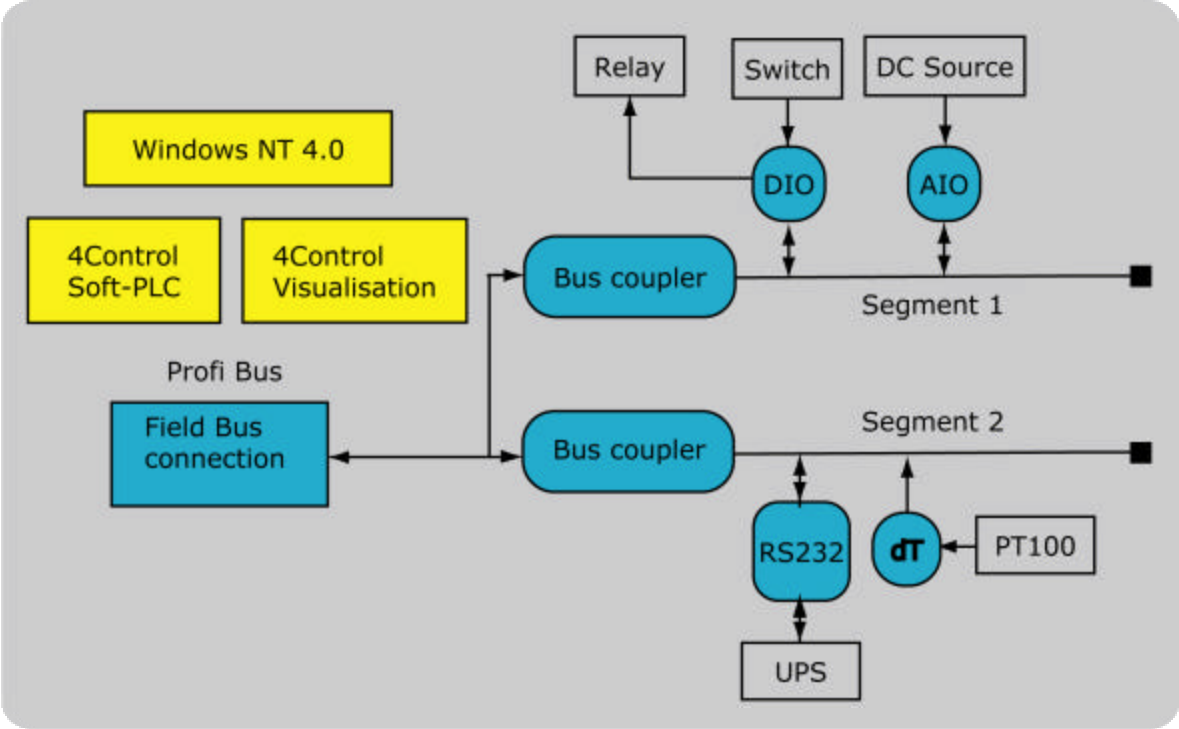

figure xx: Sample configuration of the slow control prototype systems at Forschungszentrum

The positive experience with the prototype system was transferred into the design for the Slow Control System (SCS) on site.

We use the same development software and profibus components from Fa. Beckhoff (see [xx]) as below:

- profibus bus coupler BK 3100,
- digital input terminals (24 V or 5 V; 2- or 4-wire mode),
- digital output terminals (24 V or 5 V, relay outputs (AC 230 V); 2- or 4-wire mode),
- analog input terminals (differential ±10 V or single ended; differential 4… 20 mA; resistive temperature devices (RTD) inputs),
- terminals for serial communication (RS232 interfaces), and
- system terminals (converter 24 V/ 5V; diagnostic and end terminals).

The modular design causes a fine granularity in the I/O system. It allows extending the system with additional components as needed. In every segment the functionality of I/Os can be a different. However, we install identical sets of components in each bay and one or two extra segments for more general functions to simplify software development.

1.2.3.3 Software

As the hardware of the SCS is composed of commercial components, the main effort goes into the development of the application software. We use the development software 4CONTROL [31] provided by Softing GmbH in Haar near Munich. 4CONTROL is a Win-NT based software system for the control, programming, operating and monitoring of common technical processes in production and process automation. The package includes the following features:

- real time capable Programmable Logic Controller (PLC) under Windows NT 4.0,
- IEC 1131-3 compliant programming- and implementation system for structured text, function block diagram, sequential function chart and JAVA (as IEC 1131-3 extension) as programming languages,
- intra- and internet based instrumentation and visualization,
- auto-generation of images for operation and screen information, and
- software interfaces to other applications, especially the OPC Interface [32], the SQL database interface and open file formats (ASCII).

Detailed information can be found at http://www.4control.de/. For IEC 1131-3 standard refer to [33].

Of prime importance for the SCS is that the software allows remote access via LAN to the process status of the FieldPC for remote operation, maintenance, alarm management and visualization. In addition, the OPC data exchange with computers running different operating systems (e.g. Linux) is possible via third party software packages (e.g. communication with the DAQ software, the monitoring system, etc.). For simple applications the UDP protocol can be used.

A graphical user interface (GUI) through an internet explorer allows rapid development of simple interfaces for the operator. The strongest point of this interface is its flexibility: it is most useful for the application developer; ease of use is not the main focus. Therefore a further purely Linux-based GUI just for the operators (in the FD-buildings or the central campus) is under development. It will provide more specific access to the system, but in very user-friendly way.

1.2.3.4 Safety aspects

The main tasks of the SCS which are relevant for the safety are:

- Protect the camera against damage due to high light exposure by following rules:
  - It must be ensured that the HV cannot be switched on while there is too much light in the bays.
  - During measurement the HV must shut down (HV-interlock), if the doors to the telescopes are opened or the light sensor detects a high light level in a bay.

- If the HV is on during daylight, lock the shutters against operation.

- Protect the telescope's entrance window against bad weather:

  1. It must be ensured that the shutters are closed during wind speeds above a level which destroys the aperture system.

  2. When rain is detected the shutters must be closed.

- As direct sun light would damage the camera (even without HV on) the shutters must be closed and locked during daylight and the fail-safe-curtain must fall down if a shutter is manually opened.

- Safe operation of the computer and shutter system, if the main AC power fails. The SCS and the computer system are protected by an uninterruptible power supply (UPS), which must ensure that in case of power failure the MirrorPC, EyePC and CalibrationPCs shut down properly and that all shutters are closed by the SCS. The SCS system will stay as long as possible in operation, but must shut down itself before a total discharge of the UPS batteries. A safe power-on boot procedure must be established. For a safe restart of the computer system a certain minimum UPS capacity level is mandatory.

- To avoid damage to the hardware connected to the LV/HV power supply system additional rules and actions are implemented and carried out via OPC communication:

  1. It must not be possible to switch the HV on before the LV has reached its designated values.

  2. It must not be possible to switch off the LV while the HV is on.

  3. The LV channels are connected in pairs, providing positive and negative voltage to the distribution boards. If a LV channel fails or trips during operation, the corresponding channel of opposite polarity must be switched off also.

  4. If a LV channels fail during operation, the HV channels supplied by that channel must be switched off.

- In case of failures of the SCS system itself the whole system must go automatically to a save mode. The profibus system checks its own integrity constantly. In case of errors all connected outputs go into defined states (typically zero). The wiring of the system is done in a way that in case of a profibus or FieldPC breakdown the HV is switched off, the safety curtains drop and the shutters close.

Only a very reliable SCS system can fulfill these tasks. The components of our system are in operation in industry production and plants since years. They are not approved to military or medical grade and aerospace projects. However, by selecting the hardware carefully we can achieve a very high reliability. The FieldPC from Softing GmbH has for example a meantime between failures (MTBF) of 8 years.

1.2.4 Computing Facilities

The selection of the computing facilities for data acquisition and processing are strongly influenced by the need for reliability during 20 years lifetime and remote controlled maintenance. All these requirements are fulfilled by commercial PCs with a good performance-to-cost ratio. The number of different network devices has been kept as low as possible to reduce the number of required spare parts.

The chosen system consists of an EyePC for each Fluorescence Station connected to 6 MirrorPC via a private mirror subnet. Despite the rather low data rates of less than 1 Mbyte /s during normal experiment conditions, this network is kept separate from the eye network connecting the EyePC with the telecommunication station and the slow control PC (SCPC). Figure xx show the network topology of a single Fluorescence Station.

1.2.4.1 MirrorPC

The MirrorPCs are commercial PCs running with a VIA Ezra C3 650 MHz CPU and are equipped with 256 Mbyte RAM. They operate diskless and with a passive cooling for increased lifetime. The power supply is selected to be very reliable. The MirrorPCs can be switched on and off remote controlled by the slow control.

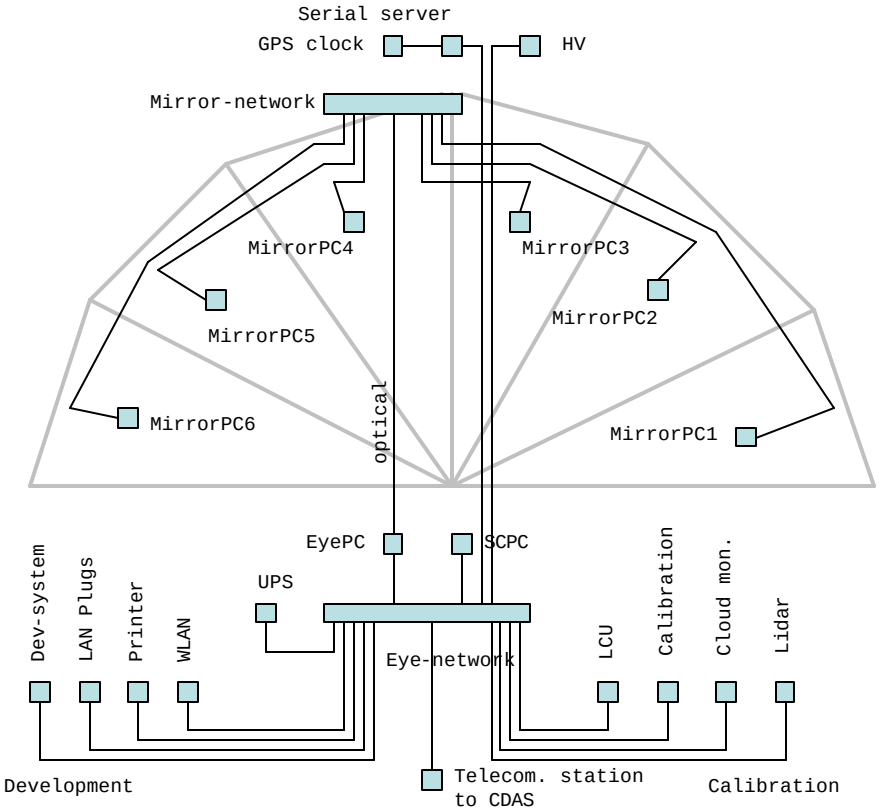

Figure xx: Network topology of a single Fluorescence Station. Each build contains two subnets divided by the EyePC. The mirror network is for exclusive use of the DAQ while the eye network connects all other devices including the radio link to CDAS. The development infrastructure might be not available in all Fluorescence Stations at any time.

1.2.4.2 EyePC

The EyePCs are used for diagnostics and monitoring, the short term data storage and the inter-telescope trigger analysis. As they are the only PCs in the data stream equipped with hard disks they serve as boot and file servers for the MirrorPCs. With respect to the data and system security a 19" Linux server was chosen. It provides RAID support for the data and system disk. Software installation on the EyePC is restricted to DAQ and monitoring processes for security reasons; access from unauthorized persons is strictly forbidden.

1.2.4.3 Slow Control PC

The Slow Control PC is described in chapter 1.2.3 "FD Telescopes Control-System (Slow Control)".

1.2.4.4 HV/LV

The HV/LV system is controlled via a network interface. Refer to chapter 1.2.3 "FD Telescopes Control-System (Slow Control)" and 1.2.1.8 for details.

1.2.4.5 Uninterruptible Power Supply (UPS)

The EyePC, the Slow Control System and the LAN switches of the eye network are UPS powered to ensure a smooth shutdown cycle in case of power failures. However, the UPS system is not designed to allow measurement during longer break down times. Consequently, the MirrorPCs and the remaining FD electronics are left UPS unprotected. The UPS will be monitored by the EyePC to ensure system restart and system operation with sufficiently loaded batteries only.

1.2.4.6 GPS clock

The GPS clock is placed between bay 3 and 4 to keep the cable length to the FE electronics in all bays as short as possible. The serial interface of the GPS clock is connected to the EyePC using a serial server. This solution allows us to place the GPS clock even far away from the position of the EyePC. Details of the clock are described in subsection 1.2.1.7.

1.2.4.7 Development facilities

The development facilities are used to commission the telescopes. They include another PC and a printer as an example. In addition, it is possible to connect notebooks (and other LAN-devices) using LAN plugs or the installed WLAN. To keep the network configuration effort low a DHPC server is running at each EyePC.

1.2.4.8 Calibration facilities

Several calibration facilities also need access to the LAN – mostly through conventional PCs:

LCU – the LED calibration unit implements a LAN interface with FPGA logic.

CalibrationPC – the PC to control of the Xenon flasher in the calibration room.

Cloud Monitor – the PC which periodically digitizes the image of the IR cloud camera.

LIDAR – the LIDAR PC controls the laser and the DAQ of the LIDAR system.

For more details refer to 1.1.9 "Calibration system" and 1.1.10 "Atmospheric monitoring".

1.2.4.9 Telecommunication station

The telecommunication station provides a radio link to the central campus (CDAS) in Malargüe.

References

1 G. Matthiae and P. Privitera , “The Schmidt Telescope with Corrector Plate”, Pierre Auger Project Technical Note GAP-98-039, 1998.

2 R. Sato, J. A. Bellido C. and H. C. Reis, “Ray-tracing of the Schmidt Camera with Corrector Plate” Pierre Auger Project Technical Note GAP-99-012, 1999.

3 J.W. Elbert, “The HiRes filter and its effect on the aperture,” in Proceedings of the Tokyo Workshop on Techniques for the Study of Extremely High Energy Cosmic Rays (ed: M. Nagano) p.232, 1993.

4 R. Cester, D.Maurizio, E. Menichetti and N. Pastrone, “Evaluation of Commercial UV Glass Filters for the Auger Prototype Fluorescence Detector”, Pierre Auger Project Technical Note GAP-99-031, 1999.

5 P. Facal San Luis and P. Privitera, "Measurement of the FD camera light collection efficiency and uniformity", Pierre Auger Project Technical Note GAP-2000-010, 2000.

6 G. Matthiae and P. Privitera, "Study of the Philips Hexagonal PMT XP3062 for the FD Camera", Pierre Auger Project Technical Note GAP-99-001, 1999.

7 M. Born and E. Wolf “Principles of Optics”, Sec. 6.4 (Cambridge University Press).

8 H.C. Reis, C.O. Escobar, R. Sato and J.A. Bellido, “A Study of the corrector plates for the Auger fluorescence detector,” Pierre Auger Project Technical Note GAP-99-013, 1999.

9 R.Sato et al.,”Corrector ‘Plate’ with an Annulus Shape” Pierre Auger Project Technical Note GAP-99-014, 1999.

10 J. Castro-Ramos and A. Cordero-Davila, “Design of a Maksutov-Bouwers Camera for the Fluorescence Detector”, Pierre Auger Project Technical Note GAP-99-011, 1999.

11 E. Fokitis, S. Maltezos and E. Papantonopoulos, “Optical Filter Design by the Simulated Annealing Method for the Fluorescence Detector of the Auger Project”, Pierre Auger Project Technical Note GAP-98-022, 1998.

12 J.A. Dobrowofsky et al., Appl. Optics, 31 3784, 1992.

13 E. Anastassakis and E. Liarokapis, J. Appl. Phys., 62 no.8, 1987.

14 M. Ambrosio et al., "The FD camera PMT test system", Pierre Auger Project Technical Note, in preparation.

15 National Institute of Standards and Technology, Calibration Program, Gaithersburg, MD 20899-2330 USA.

16 H. Gemmeke, A. Grindler, H. Keim, M. Kleifges, N. Kunka, Z. Szadkowski, D. Tcherniakhovski, "Design of the Trigger System for the Auger Fluorescence Detector", 11th IEEE NPSS Real Time Conference, Conf. Records 519-23 and IEEE-TSS Vol.47, No 2 (2000), 371-375.

17 S.Argirò et al., Monitoring DC Anode Current from a Grounded-Cathode PMT, Nucl.Inst. Meth. A435,1999 pp. 484-489

18 D. Camin and V. Re, "Analog processing of signals from the fluorescence detector", GAP 1999-019.

19 S. Argirò et al, "The Analog Signal Processor of the Auger Fluorescence detector prototype", Nucl.Instrum.Meth.A 461:440-448,2001

20 B. Dawson, "Amplitude Dynamic Range in Auger Fluorescence Electronics: Update for the Four Eye System at Nihuil", GAP 99-038.

21 P.W. Cattaneo, "The Anti-aliasing Requirements for Area and Timing Measurements with the Fluorescence Detector Read-out Channel", GAP 2000-062.

22 P.W. Cattaneo, "The anti-aliasing requirements for amplitude measurements with the Fluorescence Detector read-out channel", GAP 2000-049.

23 P.W. Cattaneo, "Comparison of Different Solutions to the Dynamic Range Reduction for the Fluorescence Detector Front End Electronics", GAP 1999-009 and P.F. Manfredi et al., "A bilinear analog compressor to adapt the signal dynamic range in the Auger fluorescence detector", Nucl. Inst. Meth. A461 (2001) 526-529

24 Specification of Interface between Analog and Digital Board is available at the BSCW document system http://fuzzy.fzk.de.

25 H. Gemmeke, M. Kleifges, A. Kopmann, N. Kunka, A. Menshikov, D. Tcherniakhovski, "First Measurements with the AUGER Fluorescence Detector Data Acquisition System", Proceedings of ICRC 2001, Hamburg, Eds: K.-H. Kampert, G. Heinzelmann, C. Spiering, on CD-ROM, page 769

26 The specification of the digital monolithic Auger backplane is available at the BSCW document system http://fuzzy.fzk.de.

27 D. Bormann, FZK internal report, Specification HPE- 285/5/1-4.

28 Auger Collaboration, "Conventions for the Pierre Auger Observatory", ???

29 See for example: http://www.beckhoff.com/english/busterm/default.htm or http://www.beckhoff.com/english/busterm/aufbau.htm

30 Profibus Home Page: http://www.profibus.com .

31 4CONTROL Datasheet, Sept. 99, Version 1.2, Softing GmbH

32 OPC Foundation: OLE for Process Control (OPC) Final Specification V2.0. OPC Foundation, P.O. Box 140524, Austin, Texas, 10/1998 or http://www.opcfoundation.org .

33 Standardization in industrial programming and control: http://www.plcopen.org .